



HAL
open science

Stratégies de commandes assistives pour les exosquelettes des membres inférieurs

Weiguang Huo

► **To cite this version:**

Weiguang Huo. Stratégies de commandes assistives pour les exosquelettes des membres inférieurs. Traitement du signal et de l'image [eess.SP]. Université Paris-Est, 2016. Français. NNT : 2016PESC1041 . tel-01534826

HAL Id: tel-01534826

<https://theses.hal.science/tel-01534826>

Submitted on 8 Jun 2017

HAL is a multi-disciplinary open access archive for the deposit and dissemination of scientific research documents, whether they are published or not. The documents may come from teaching and research institutions in France or abroad, or from public or private research centers.

L'archive ouverte pluridisciplinaire **HAL**, est destinée au dépôt et à la diffusion de documents scientifiques de niveau recherche, publiés ou non, émanant des établissements d'enseignement et de recherche français ou étrangers, des laboratoires publics ou privés.

École Doctorale MSTIC

Laboratoire Images, Signaux et Systèmes Intelligents

THÈSE

Présentée pour l'obtention du grade de DOCTEUR
DE L'UNIVERSITE PARIS-EST

par

Weiguang Huo

**Stratégies de commandes assistives pour les
exosquelettes des membres inférieurs**

**Assistive Control Strategies for Lower-limb
Exoskeletons**

Spécialité : Robotique

Soutenue le 06 décembre 2016 devant un jury composé de :

Président du jury	Prof. Jean-Pierre Merlet	<i>INRIA Sophia Antipolis</i>
Directeur de thèse	Prof. Yacine Amirat	<i>University Paris Est Créteil</i>
Co-encadrant de thèse	Dr. Samer Mohammed	<i>University Paris Est Créteil</i>
Rapporteur	Prof. Gabriel Abba	<i>Ecole Nationale d'Ingénieurs de Metz</i>
	Prof. Ravi Vaidyanathan	<i>Imperial College London</i>
Examineur	Prof. Jean-Michel Gracies	<i>UPEC-CHU Mondor</i>

Acknowledgements

FIRST of all, I would like to thank my advisor, Yacine Amirat, and co-advisor, Samer Mohammed, for their continuous support and precious guidance during this research work. They gave me the liberty to develop my own ideas, at the same time, encouraged me with their enthusiasm and were willing to help me with their knowledge and experience. Without their support, this thesis work would not be finished.

I would also like to express my sincere gratitude to all my collaborators and co-authors: Kyoungchul Kong, Jian Huang, Juan C. Moreno, Hala Rifai and Sehoon Oh for their fruitful discussions and invaluable advices during my research, also to Victor Arnez-Paniagua and Ivan Colorado-Cervantes for their friendship and helpful assistance during experiments. I am also grateful to Hanseung Woo, Byeonghun Na, and other members who are from the RAS lab of Sogang University, for their support in developing the lower limb exoskeleton.

I would like to thank all the members of the jury for reviewing this thesis and giving their valuable and constructive suggestions and comments: Jean-Pierre Merlet, Gabriel Abba, Ravi Vaidyanathan, and Jean-Michel Gracies.

I thank all members of the LISSI lab. They are enthusiastic, smart and willing to share knowledge. It was a wonderful experience to work with them. Also, many thanks to my friends, Zhaoxia Li, Pierre Rigaudière, Jungsoo Cho, Ferhat Atta, for their support in my life and research during my time in France.

Finally, I would like to express my deepest gratitude to my wife, Xiao Wang, and family members, Jiwang Huo, Lingrong Huo, Rongqin, An, for their endless support, encouragement and love.

06 December 2016

Weiguang Huo

Abstract

NEUROLOGICAL problems caused by stroke and spinal cord injury as well as the weakness of skeletal muscles may considerably affect the motor ability of the elderly and infirm. Traditional solutions of assistance and treatment for these dependent people are relatively costly; they generally need significant human efforts and financial resources from caregivers and national healthcare centers. Moreover, a recent survey from the United Nations shows that many regions and countries are experiencing rapid population ageing, for instance, Europe and Japan. In this context, robotics appears as a convenient and promising solution to develop assistive systems for improving the autonomy of dependent people. Lower limb exoskeletons are wearable robots that can be used as assistive devices for augmenting the wearer's motor ability and/or improving the effectiveness of neuromuscular rehabilitation. Recently, they have attracted increasing interest in the robotics community. As lower limb exoskeletons exhibit close cognitive and physical interactions with the wearer, a fundamental function is to provide appropriate power assistance by taking into account the wearer's sensor-motor ability. Consequently, it is of great importance to develop human intention based control strategies. Meanwhile, from the exoskeleton's viewpoint, the physical contacts with the wearer and the environment are both considered disturbances affecting the accomplishment of the wearer's desired movements. These disturbances should also be taken into account during the design of control strategies.

In this thesis, we develop three assistive control strategies for lower limb exoskeletons. In the meantime, two modes of assistance are studied: the passive mode in which the wearer has very limited motor ability as well as the active-assisted mode in which the wearer has certain motor ability but that is insufficient to perform autonomously a desired physical movement. To evaluate the proposed control strategies, two lower limb exoskeleton prototypes are developed: a knee joint lower limb exoskeleton, called EICOSI, and a full lower limb exoskeleton, called E-ROWA.

In the first control strategy, the wearer is assumed to be in passive mode. A robust sliding mode control approach is developed based on the use of a nonlinear disturbance observer, in order to guarantee accurate tracking performance of desired knee joint movements. This control strategy ensures the tracking error converges to zero in finite time. Moreover, the use of the nonlinear disturbance observer guarantees robustness with respect to modeling uncertainties and external disturbances from the wearer and/or environment. The stability

and the convergence of the proposed control approach are theoretically proven by means of a Lyapunov analysis. Experimental results, obtained in the case of knee joint flexion/extension movements, show significant advantages in terms of position tracking and robustness with respect to modeling uncertainties and external disturbances, compared to classical control approaches.

In the second control strategy, we propose a human intention based nonlinear active impedance control structure, in which the wearer is in an active-assisted mode. This assistive strategy is used to assist the wearer in single-task physical activities, for instance, the knee joint flexion/extension movement. The structure of the proposed control strategy consists of three main parts: a nonlinear observer to estimate the human joint torque, a desired impedance model of the human-exoskeleton system and a sliding mode based tracking controller. We investigate the performance of the proposed control structure based on two case studies: knee-joint flexion/extension movements and sit-to-stand movements. Correspondingly, we develop a single-joint active impedance controller and an extended multi-joint one for both cases, respectively. Their stabilities and robustness with respect to modeling uncertainties are theoretically analyzed as well. In the first case study, the inertia, damping and gravity of the human limb are efficiently compensated without affecting the system stability. With the impedance compensation, the amplitude of EMG signals of the wearer's vastus medialis can be reduced by up to 60%. In the second case study, we furthermore develop a time-varying desired impedance model that enables the lower limb exoskeleton to provide adaptable power assistance according to the wearer's lower limb motor ability. The performance of this proposed approach is evaluated by analyzing the EMG signals of the vastus lateralis muscle.

Finally, the third control strategy is developed to assist the wearer during walking activities. Different gait modes such as level walking, stair ascent and stair descent show different lower-limb kinematic and kinetic characteristics. In this case, we propose a new approach that is able to detect the gait mode at the early beginning of a new step using the kinematic features namely velocity and position of the wearer's feet during walking. These features are measured using body-worn inertial measurement units and joint angle sensors of the E-ROWA exoskeleton. In order to accurately estimate the kinematic features, we propose a Kalman filter based feature update algorithm by combining a zero-velocity detection method and a human kinematic model. A fuzzy logic based algorithm is used to estimate the likelihood of each gait mode in real time. The proposed gait mode detection approach makes it possible to select appropriate kinematic and kinetic models for each gait mode. Different assistive strategies are developed: partial gravity compensation, virtual-spring/damper based impedance assistance and zero impedance assistance. These strategies are combined differently according to the estimated wearer's gait mode. Experiments conducted with different healthy subjects show satisfactory results in terms of the latency and success rate of the gait mode detection as well as the effectiveness of assistive strategy.

Keywords: Lower limb exoskeletons, robust control, nonlinear disturbance observer, active impedance control, gait mode detection.

Résumé

LES problèmes neurologiques dus aux AVC et aux lésions de la moelle épinière ainsi que la faiblesse des muscles squelettiques peuvent considérablement affecter les capacités motrices des personnes infirmes ou âgées. Les solutions traditionnellement utilisées pour l'assistance et le traitement de ces personnes dépendantes, sont relativement coûteuses ; en termes de prise charge, elles impliquent, pour les aidants et les services de santé, des efforts humains et des moyens financiers importants. Par ailleurs, une étude récente des nations unies a montré que plusieurs régions et pays dans le monde, comme par exemple le Japon et l'Europe, souffrent du problème du vieillissement rapide de leurs populations. Dans ce cadre, la robotique apparaît comme une solution bien adaptée et prometteuse pour développer des systèmes d'assistance permettant d'améliorer l'autonomie des personnes dépendantes. Les exosquelettes des membres inférieurs sont des robots portables, destinés à être utilisés en tant que dispositifs d'aide à la mobilité pour augmenter les capacités motrices des sujets porteurs, ou comme auxiliaires de rééducation neuromusculaire. Ce domaine de recherche a fait l'objet, ces dernières années, d'un intérêt grandissant au sein de la communauté robotique. Du fait qu'un exosquelette est caractérisé par une interaction physique et cognitive directe avec son porteur, sa fonction principale est de fournir une assistance adaptée aux capacités sensori-motrices du sujet porteur. Il est, par conséquent, nécessaire de développer des stratégies de commande basées sur l'intention de mouvement du porteur. Du point de vue de l'exosquelette, les contacts physiques avec le sujet porteur ou l'environnement sont considérés comme des perturbations affectant la bonne réalisation des mouvements désirés du porteur. Ces perturbations doivent être également être prises en compte lors de la conception des stratégies de commande.

Dans cette thèse, nous proposons trois stratégies de commandes assistives pour les exosquelettes des membres inférieurs. Deux modes d'assistance sont étudiés ici : le mode passif où le sujet dispose de capacités motrices très limitées et ne développe quasiment aucun effort, et le mode actif-aidé où le sujet possède certaines capacités motrices mais qui sont insuffisantes pour réaliser de manière autonome un mouvement désiré. Pour évaluer les performances des stratégies de commande proposées, deux prototypes d'exosquelettes des membres inférieurs ont été développés : l'exosquelette de l'articulation du genou EICOSI, et l'exosquelette des membres inférieurs E-ROWA.

Résumé

Dans la première stratégie de commande, le sujet est supposé être en mode passif. Une commande robuste par modes glissants, basée sur un observateur non-linéaire de perturbations (Nonlinear Disturbance Observer (NDO)), est développée pour garantir un suivi précis des mouvements désirés de l'articulation du genou. Cette stratégie de commande garantit une convergence de l'erreur de suivi vers zéro en temps fini. Par ailleurs, l'utilisation de l'observateur non-linéaire de perturbations permet de garantir la robustesse du système vis-à-vis des incertitudes paramétriques et des perturbations externes dues au porteur ou à l'environnement. Une analyse de stabilité au sens de Lyapunov est développée pour prouver formellement la stabilité et la convergence de l'approche de commande proposée. Les résultats expérimentaux, obtenus dans le cas des mouvements de flexion/extension de l'articulation du genou, montrent que la stratégie de commande proposée présente des avantages significatifs en termes de précision du suivi de position et de robustesse vis-à-vis des incertitudes de modélisation et des perturbations externes, comparativement aux approches classiques de commande.

Dans la deuxième stratégie de commande, nous proposons une structure de commande en impédance active non-linéaire où le sujet est supposé être en mode actif-aidé. Cette stratégie de commande assistive est utilisée pour assister le porteur dans la réalisation d'activités physiques mono-tâche, telles que la flexion/extension du genou ou le transfert assis-debout. La structure de commande proposée comporte trois éléments principaux : un observateur non-linéaire pour estimer le couple développé par le sujet porteur au niveau articulaire, un modèle d'impédance désirée du système porteur-exosquelette, et enfin, un contrôleur par modes glissants pour le suivi de mouvements. L'évaluation des performances de la structure proposée sont étudiées dans le cadre de deux activités : la flexion/extension du genou et le transfert assis-debout. Pour ce faire, nous avons développé un contrôleur en impédance active mono-articulaire, pour le cas de la flexion/extension du genou, et une extension de ce contrôleur pour la commande de plusieurs articulations, pour le cas du transfert assis-debout. La stabilité et la robustesse du système vis-à-vis des incertitudes de modélisation sont analysées théoriquement pour chaque cas. Dans le premier cas d'étude, l'inertie, l'amortissement et la gravité des membres inférieurs du porteur sont compensés sans affecter la stabilité du système. La compensation d'impédance permet de réduire jusqu'à 60% l'amplitude des signaux EMG mesurés au niveau du muscle extenseur Vastus Medialis du porteur. Dans le deuxième cas d'étude, nous développons un modèle d'impédance variable dans le temps qui permet à l'exosquelette de fournir une assistance adaptée aux capacités motrices du porteur. Les performances de la stratégie de commande proposée sont évaluées en analysant les signaux EMG mesurés au niveau du muscle extenseur Vastus Lateralis.

Enfin, la troisième stratégie de commande proposée est une commande contextualisée pour assister le porteur dans ses activités de marche. Les différents modes de marche, tels que la marche sur sol plat, la montée d'escaliers et la descente d'escaliers, induisent pour les membres inférieurs des caractéristiques cinématiques et cinétiques différentes. Dans ce cadre, nous proposons une approche permettant de détecter le mode de marche dès le début d'un nouveau pas, en utilisant les caractéristiques cinématiques du porteur, à savoir la position et

la vitesse des pieds lors de la marche. Ces caractéristiques sont mesurées en utilisant des centrales inertielle miniaturisées portables et les capteurs de positions articulaires embarqués sur l'exosquelette E-ROWA. Pour assurer une bonne estimation des caractéristiques cinématiques du porteur, un algorithme basé sur un filtre de Kalman, est développé en combinant la méthode de détection de vitesse zéro et le modèle cinématique du porteur. Un algorithme flou est également proposé pour estimer la vraisemblance de chaque mode de marche en temps réel. L'approche de détection du mode de marche rend possible la sélection des modèles cinématique et cinétique appropriés pour chaque mode. Différentes stratégies d'assistance sont développées : compensation partielle de la gravité, assistance basée impédance de type ressort virtuel, assistance basée impédance de type amortisseur virtuel et assistance de type impédance nulle. Ces stratégies sont combinées différemment selon le mode de marche estimé. Les expérimentations conduites avec la participation de plusieurs sujets sains montrent des résultats satisfaisants en termes de latence, de taux de succès concernant la détection du mode de marche, et aussi d'efficacité de la stratégie d'assistance.

Mots clefs : Exosquelette des membres inférieurs, Commande robuste, Commande par impédance active, Observateur non-linéaire de perturbations, Détection du mode de la marche.

Symbols

Human-EICOSI System Control

<i>Notation</i>	<i>Description</i>
$J = J_h + J_e$	Inertia of the human shank-foot/EICOSI
$B = B_h + B_e$	Viscous friction of the human shank-foot/EICOSI
A	Solid friction of the EICOSI exoskeleton
K_j	Stiffness of the knee joint
J_d	Desired inertia of the shank-foot-exoskeleton system
B_d	Desired damping of the shank-foot-exoskeleton system
K_d	Desired stiffness of the shank-foot-exoskeleton system
τ_e	Output torque of the EICOSI exoskeleton
$\tau_{h,k}$	Human knee joint torque
$\hat{\tau}_{h,k}$	Estimated human knee joint torque
θ	Measured knee joint angle
θ_{rp}	Rest position of the knee joint in the sitting position
θ_d	Desired joint angle of the exoskeleton
θ_r	Reference joint angle of the human-exoskeleton system
e	Tracking error
$\tau_g = \tau_{g,h} + \tau_{g,e}$	Gravitational torque of the human shank-foot/EICOSI
$\text{sgn}(\cdot)$	the signum function.

Human E-ROWA System Control

<i>Notation</i>	<i>Description</i>
\mathbf{q}	Measured joint angle vector
\mathbf{q}_d	Desired joint angle vector
\mathbf{q}_r	Reference joint angle vector
$\boldsymbol{\tau}_e$	Exoskeleton joint torque vector
$\boldsymbol{\tau}_h$	Human joint torque vector
$\hat{\boldsymbol{\tau}}_h$	Estimated human joint torque vector
$\theta_a, \theta_k, \theta_h$	Relative joint angles of ankle, knee and hip
$\tau_{h,a}, \tau_{h,k}, \tau_{h,h}$	Torques generated by the human ankle, knee and hip joints
$\tau_{e,k}, \tau_{e,h}$	Torques generated by the exoskeleton knee and hip joints
$\mathbf{F}(F_{sx}, F_{sy})$	Interaction forces generated between the human wearing the exoskeleton and the chair.

Parameters of the Human E-ROWA System

<i>Notation</i>	<i>Description</i>
m_{h1}, m_{h2}, m_{h3}	Masses of the human shank, thigh and HAT
m_{e1}, m_{e2}, m_{e3}	Masses of the exoskeleton shank, thigh and HAT
I_{h1}, I_{h2}, I_{h3}	Inertias of the human shank, thigh and HAT
I_{e1}, I_{e2}, I_{e3}	Inertias of exoskeleton shank, thigh and HAT
k_{h1}, k_{h2}, k_{h3}	The coefficients of distribution of gravity for the human shank, thigh and HAT respectively
k_{e1}, k_{e2}, k_{e3}	The coefficients of distribution of gravity for the exoskeleton shank, thigh and HAT respectively
l_1, l_2, l_3	Lengths of the human shank, thigh and HAT

Contents

Acknowledgements	i
Abstract (English/Français)	iii
Symbols	ix
1 General Introduction	1
1.1 Motivations and Challenges	1
1.2 Objectives of the Thesis	2
1.3 Our Lower Limb Exoskeletons	3
1.3.1 EICOSI Knee Joint Exoskeleton	3
1.3.2 E-ROWA Lower Limb Exoskeleton	4
1.4 Outline of the Thesis	6
1.5 Contributions of our Work	8
2 Overview of Lower Limb Exoskeletons	11
2.1 Introduction	11
2.2 Lower-limb Exoskeletons: A Brief Review	13
2.2.1 Exoskeletons with Hydraulic or Pneumatic Actuators	13
2.2.2 Exoskeletons with Electrical Motors	14
2.2.3 Exoskeletons with SEAs	15
2.2.4 Exoskeletons with Pneumatic Muscle Actuators	17
2.2.5 Other Exoskeletons	17
2.3 Control Strategies	20
2.3.1 Direct-intention based Control Algorithms	20
2.3.2 Gait-mode based Control Algorithms	23
2.3.3 Reference Tracking Control Algorithms	26
2.4 Assessment Methods	27
2.4.1 Metabolic Cost	27
2.4.2 Gait Biomechanical Analysis	28
2.4.3 Muscle Activity Analysis	29
2.5 Discussion	30
	xi

3	Joint-level Tracking Control Strategy	33
3.1	Introduction	33
3.2	System Modeling	34
3.2.1	Human-Exoskeleton System	34
3.2.2	Parametric Identification	35
3.3	Control Algorithms	35
3.3.1	Nonlinear Disturbance Observer	36
3.3.2	NDO-based Sliding Mode Control	37
3.3.3	NDO-based Terminal Sliding Model Control (TSMC)	38
3.4	Experimental Evaluation	41
3.4.1	Comparison of Tracking Precision	42
3.4.2	Comparison of the Required Time to Eliminate Disturbance	44
3.4.3	Comparison of the Robustness Regarding Modeling Uncertainties	45
3.5	Conclusion	49
4	Intention Based Single-task Assistive Control Strategy	51
4.1	Introduction	51
4.2	System Modeling	53
4.2.1	The Knee Joint Flexion/Extension Movement	53
4.2.2	The Sit-to-Stand Movement	54
4.3	Control Algorithms: Active Impedance Control Structure	55
4.4	Active Impedance Controller Design for Single-joint Movements	57
4.4.1	Human Joint Torque Observer	57
4.4.2	Sliding Mode Controller (SMC)	59
4.4.3	Desired Impedance Model	61
4.4.4	Robustness with Respect to Modeling Uncertainties	63
4.5	Active Impedance Controller Design for Multi-joint Movements	66
4.5.1	Human Joint Torque Observer	66
4.5.2	Desired Impedance Model	67
4.5.3	Design of the Sliding Mode Controller	68
4.5.4	Analysis of the Tracking Performance	69
4.5.5	Robustness with Respect to Modeling Uncertainties	70
4.6	Experiments of Knee Joint Flexion/Extension Movements	72
4.6.1	Parametric Identification	72
4.6.2	Assessment Method	75
4.6.3	Experimental Protocol	77
4.6.4	Experimental Results	78
4.7	Simulations and Experiments of Sit-to-Stand Movements	83
4.7.1	Parametric Identification	84
4.7.2	Simulation Study	85
4.7.3	Preliminary Experiments	86
4.8	Conclusion	89

5	Gait-mode Based Multi-task Assistive Control Strategy	93
5.1	Introduction	93
5.2	A Wearable Robot for Walking Assistance	94
5.2.1	E-ROWA	94
5.2.2	Inertial Measurement Units (IMUs)	94
5.3	Human Gait Mode Detection	96
5.3.1	Reference Point	96
5.3.2	Gait Modes	97
5.3.3	Gait Mode Detection	97
5.3.4	Sensor Fusion Using Kalman Filter	100
5.3.5	Fuzzy Logic based Approach for Gait Mode Detection	103
5.4	Assistive Torque Control based on Gait Mode Detection	105
5.4.1	Assistive Strategies According to Gait Modes	105
5.4.2	Gait Phases Detection	108
5.4.3	Assistive Torque Generation	110
5.5	Experimental Verifications	112
5.5.1	Detection of the Zero-velocity Instant	112
5.5.2	Gait Modes Detection	113
5.5.3	Assistive Torque Generation	114
5.5.4	Comparison Study	118
5.6	Conclusion	120
6	Conclusions and Outlook	123
A	Modeling of the Sit-to-Stand Movement	127
B	Calibration Procedure of the IMU Alignment	129
	Glossary	132
	Bibliography	144
	List of figures	145
	List of tables	149
	List of Publications	151

1 General Introduction

1.1 Motivations and Challenges

ALONG with the worldwide population ageing, there is increasing interest in the use of robotic devices to assist dependent people (elderly/infirm) in accomplishing their main daily living activities as well as rehabilitation exercise training. A recent survey from the United Nations shows that people aged 60 and over represented almost 11.5 percent of the global population in 2012, and this percentage is projected to nearly double to 22 percent by 2050 [1]. In some regions and countries, the problem of an ageing population is particularly prominent. For example, in Japan, the population aged 60 and over reached more than 30 percent by 2012, while 34 percent of the European population will be aged 60 and over by 2050 [1]. Neurological injuries such as stroke, spinal cord injuries (SCI) and weaknesses of the skeletal muscles seriously limit the mobility of the elderly and infirm to perform daily living activities [2]. Current research challenges include the development of new therapeutic tools and methods that guarantee the improvement of the locomotive performance of the elderly/infirm during their daily living activities as well as the movement restoration of the impaired lower limbs. Recently, assistive robotics has appeared as a promising and efficient solution to physically assist dependent people during rehabilitation training programs and daily living activities [3]. Indeed, robots/exoskeletons can overcome many limits of the traditional therapeutic devices to considerably reduce the required labor intensity from the therapists, improve the training performance such as repeatability, and be easily applied during daily living.

Developing portable, intelligent and highly efficient lower limb wearable robots (i.e., exoskeletons/orthoses) is generally considered as a solution for assisting individuals suffering from neurological and/or lower limb musculoskeletal disorders. During the last decade, various lower limb wearable robots have been developed as academic prototypes and commercial products due to the latest advances in the fields of actuators, sensors, and human-robot interaction paradigms [4]. Although there is still much room for improvement, the potential benefits of wearable robotics have been extensively revealed by improving the wearer's reha-

bilitation performance, daily living mobility, and general improvement of life quality [4–6]. It can be predicted that lower limb wearable robotics will become a widely used technology in the near future [7].

To further promote the development of lower limb wearable robots, researchers still face many challenges in both the hardware and software aspects. In terms of the hardware design, two crucial features, the portability and wearability, need to be further improved. Thus, exoskeletal frames should be more lightweight and fully take into account human biomechanics. High-efficiency compact actuators are needed to ensure sufficient and safe power assistance. Associated enabling techniques such as the power supply and sensors also limit the practical applications of lower limb exoskeletons. In addition to hardware improvements, developing appropriate control algorithms will be of great importance to improve the efficiency of the physical assistance provided by the powered exoskeleton. A basic function for most lower limb exoskeletons is to ensure the performance of a given task that can be characterized by a desired trajectory/torque determined by a therapist or following the intention of the wearer. However, the tracking performance is affected by the wearer's remaining motor ability or interaction with the environment (e.g., foot contacts). Powered exoskeletons are supposed to assist the wearer in performing daily living activities while cooperating with the remaining motor ability of the wearer. This means that the wearer's motion intention should be accurately tracked by the exoskeletons. Furthermore, various terrains such as level ground and stairs are usually faced by the wearer when walking in a living space. In this case, different assistive strategies as well as a fast and transparent gait motion transition algorithm are required. Despite the large amount of work done in this field [4, 7], there still exist many unsolved questions with regard to the aforementioned challenges. In the following section, we will present in detail the objective of this thesis.

1.2 Objectives of the Thesis

The aim of our work is to improve the state-of-the-art control strategies for lower limb exoskeletons during the physical assistance of individuals with limited muscular capabilities during daily living activities. These control strategies include joint-level tracking control as well as human motion intention based single-task and multi-task power assistance controls. In the following, we identify the objectives of this thesis, listed by the steps for designing control strategies.

1. Developing a joint-level reference tracking control algorithm of lower limb exoskeletons. The proposed approach is robust with respect to disturbances from both the wearer and external environment. Additionally, the convergence speed of the proposed algorithm is relatively fast.
2. Proposing a human intention based control strategy that is able to provide appropriate power assistance to assist the wearer in performing a single lower limb motion task. The

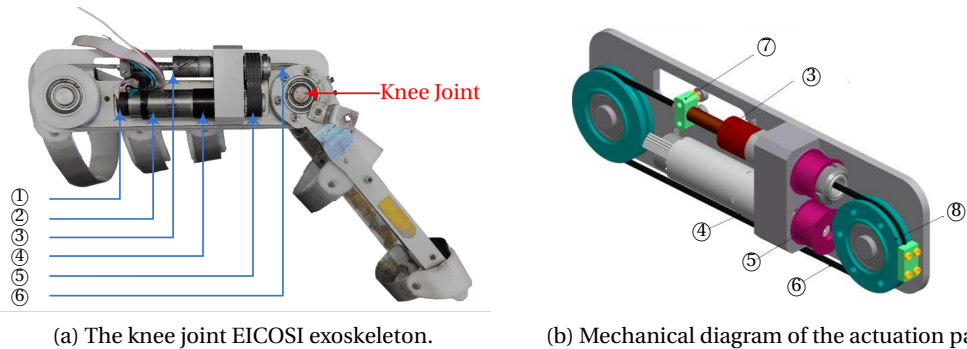


Figure 1.1 – The Exoskeleton Intelligently COMMunicating and Sensitive to Intention (EICOSI). (① - Encoder; ② - Brushless DC motor; ③ - Ball screw; ④ - Gear motor; ⑤ - Belt transmission; ⑥ - Cable drive; ⑦ - Angle keeper; ⑧ - Pulley)

proposed control structure is general and can easily be employed for various motion tasks and implemented using different exoskeletal devices.

3. Designing a fast human gait mode detection algorithm when using lower limb exoskeletons. Combining with the proposed detection algorithm, a control strategy is also needed to guarantee the provision of seamless and natural power assistance for different gait tasks such as level walking and stair ascent/descent.
4. Evaluation of the proposed control methods using two lower limb exoskeletons that were developed during the thesis work. The effectiveness of the proposed approaches can be efficiently verified by experiments using appropriate assessment methods.

1.3 Our Lower Limb Exoskeletons

In this thesis work, two lower limb exoskeletons, EICOSI and E-ROWA, were developed for the evaluation of the proposed control algorithms. In this section, we present the main features of these two exoskeletons.

1.3.1 EICOSI Knee Joint Exoskeleton

A single Degree of Freedom (DoF) prototype exoskeleton (EICOSI, Exoskeleton Intelligently COMMunicating and Sensitive to Intention) was designed to provide power assistance at the wearer's knee joint level (Figure 1.1a). The exoskeleton consists of two segments attached separately to the thigh and shank and fixed to the wearer's leg using appropriate braces (Figure 1.2). The total mass of this exoskeleton is about 3 Kg, and is actuated by a high-power brushless DC motor (Maxon, Switzerland). To ensure a compact and portable structure and a relatively high output torque, a compact transmission system is designed using a gear motor, a ball screw, a belt transmission and a cable drive (Figure 1.1b). The reduction ratio from the



Figure 1.2 – A subject wearing the EICOSI exoskeleton in the sitting position.

motor side to the joint side is 264:1. The whole actuator can deliver up to 18 Nm .

The motor is equipped with an incremental encoder that measures the motor's rotation angle with a resolution of 1000 pulses per revolution. The knee joint angle can be calculated based on the reduction ratio of the whole transmission system. The angular velocity is obtained using a numerical derivation of the joint angle. To solve the oversampling problem, a fourth-order Butterworth filter is used to process the raw measured knee joint angle. The maximal rotation angle and angular velocity are -2.1 rad and ± 2.1 rad/s, respectively. The motor is driven using a motion controller EPOS 70/10 (Maxon, Switzerland), and is controlled using a host PC equipped with a controller board (dSPACE, Germany) running at 1 kHz. The output torque of the EICOSI is calculated based on the motor's output torque and the reduction ratio of the transmission mechanism. The control programs were developed using the MATLAB software (Mathworks, USA).

1.3.2 E-ROWA Lower Limb Exoskeleton

E-ROWA (Exoskeletal-Robotic Orthotics for Walking Assistance) developed by SG Mechatronics Co., is designed to assist dependent people to regain locomotion functions (see Figure 1.3). This exoskeleton consists of four parts: exoskeletal frames, sensor system, hardware control system, and a power unit. The weight of the whole exoskeleton is about 17 Kg.

The exoskeletal frames consists of 10 degrees of freedom (DoFs), and are attached to the wearer's waist and legs by means of straps. For each limb, there are three DoFs at the hip joint level (including flexion/extension, adduction/abduction and rotation), one DoF at the knee joint level (flexion/extension) and one DoF at the ankle joint (dorsiflexion/plantarflexion). The lengths of the exoskeletal frames such as shank and thigh are adjustable for different wearers (height: 165-190 cm). The angular motion range of each DoF is listed in Table 1.1. The exoskeleton hip and knee joints of each limb are actuated in the sagittal plane (flexion/extension movements) using two compact Rotary Series Elastic Actuators (cRSEA) respectively, while the remaining DoFs are passive. The cRSEA has several advantages over traditional actuation modes, in particular, in terms of precision, large torque generation, low output impedance, and hardware compactness, etc. At the same time, it can achieve the joint lock function

1.3. Our Lower Limb Exoskeletons

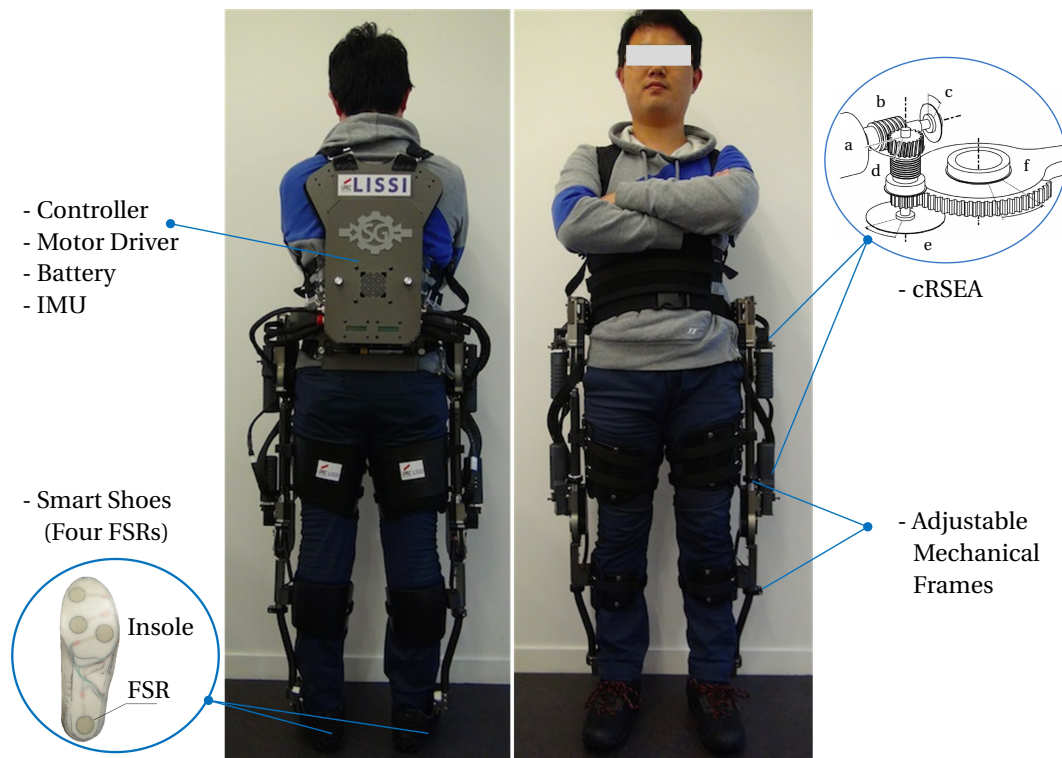


Figure 1.3 – Lower limb exoskeleton E-ROWA (Exoskeletal-Robotic Orthotics for Walking Assistance). a: DC motor, b: worm gear and worm wheel, c and e: angle sensors, d: spring, f: hip/knee joint.

in the case of power failure, due to the use of worm wheel and gear. The designed cRSEA efficiently achieves the important characteristics such as the compact actuation design and mechanical safety (i.e., joint lock function), which have been separately pointed out in existing exoskeletons MINDWALKER [8] and Vanderbilt exoskeleton [9]. The use of cRSEA actuators enables transparent physical assistance with minimal discomfort due to the reduction of the mechanical impedance of the robot. The output torque of each actuator can be measured using a torsional spring included in the cRSEA. The maximum output torque of each cRSEA is about 25 Nm.

The E-ROWA is also equipped with various sensors in order to identify the wearer's states in real-time. An Inertial Measurement Unit (IMU) sensor is mounted in the backpack (see Figure 1.3) to measure the inclination angle of the wearer's torso. Two incremental encoders (Maxion, Switzerland) mounted in the cRSEA are used to measure the motor and joint angles, respectively. Note that the deflexion angle of the torsional spring can also be calculated based on the motor and knee joint angles as well as the corresponding gear ratios. Moreover, the hip and knee joints are equipped with 13 bits absolute encoders (Renishaw Co. UK) that can be used for setting and identifying the initial position of the active joints. The ground reaction force (GRF), which is an important metric for gait phase detection, is measured using four force-sensing resister (FSR, Tekscan, USA) sensors that are attached at four different locations

Joint	DoF	Angular Range (deg)
	rotation	-10 ~ 10
Hip	adduction/abduction	-20 ~ 20
	flexion/extension	-45 ~ 120
Knee	flexion/extension	-120 ~ 0
Ankle	flexion/extension	-180 ~ 180

Table 1.1 – The motion angular range of each DoF of the E-ROWA

(i.e., toes, Meta12, Meta45, heel) on the insole (see Figure 1.3).

A NI™myRIO is used for the data acquisition and the control of the E-ROWA. It can be wirelessly connected with a host PC. The control algorithm is developed using LabView (Nations Instruments, United States). The whole exoskeleton is powered by a Li-Po battery unit that can last about 3 hours between charges.

1.4 Outline of the Thesis

According to the aforementioned objectives, a three-level structure (see Figure 1.4) is proposed to organize this thesis by considering the wearer’s role (i.e., passive mode or active-assisted mode) and applications (i.e., single-task or multi-task activity). Here, the passive and active-assisted modes are defined as follows: in the passive mode, the wearer is considered to have very limited motor ability, and to be passive during the movements with exoskeleton’s assistance; in the the active-assisted mode, the wearer is assumed to have certain motor ability but that is insufficient to perform autonomously a desired physical movement, while the exoskeleton is used to complement the wearer’s strength. Based on this structure, the

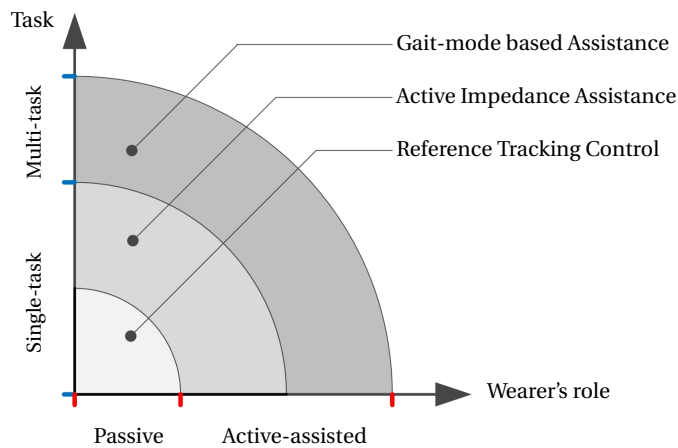


Figure 1.4 – The scope of the thesis

proposed control strategies are categorized into three classes: the first one is a joint-level controller designed for providing robust and accurate tracking of a given task; the second one is a nonlinear active impedance control structure that is able to assist wearers in performing a desired movement by taking into account the human's motor ability; and the last one represents a fast gait mode detection algorithm and a multi-gait-mode torque assistive control strategy. Correspondingly, the rest of the thesis is organized as follows.

Chapter 2 presents an overview of lower limb exoskeletons for assistance and rehabilitation in the literature, in particular, a synthesis of the well-known exoskeleton devices, the adopted control strategies and the associated assessment methods. ¹

Chapter 3 introduces a control method of lower limb exoskeletons using a reference tracking trajectory at the knee joint level (flexion/extension). A model, integrating the human shank and orthosis, is presented. A robust terminal sliding mode control approach combined with a nonlinear observer is proposed to reduce the influence of internal and external disturbances. To illustrate the effectiveness of the proposed control method, a comparison study with two control methods (i.e., basic sliding mode and sliding mode with nonlinear observer) is shown. The asymptotic stability of the proposed approaches and observer convergence are proved by means of a Lyapunov analysis. The advantages of the proposed approach, in terms of improving the tracking precision and reducing the required time for eliminating external disturbances, are theoretically analyzed as well. The effectiveness and robustness of the presented methods are evaluated by experiments using the EICOSI exoskeleton. ²

Chapter 4 presents a general intention-based nonlinear active impedance control (AIC) structure applied on a lower limb exoskeleton. The AIC structure includes three parts: a human joint torque observer, a desired impedance model and a disturbance observer based sliding mode controller. The AIC is able to adapt the mechanical impedance of the human-exoskeleton system towards a desired one using the exoskeleton's power assistance. Based on this structure, two cases are studied: single-joint and multi-joint cases. In the first case, a specific control strategy is proposed for the knee joint exoskeleton EICOSI to perform flexion/extension movements. The effectiveness of the structure with respect to reducing the human effort by active impedance assistance is fully studied. In the second case, the control structure is extended to a multi-joint one, which is used to provide appropriate power assistance for the sit-to-stand movement with the E-ROWA exoskeleton. The proposed approach's performance and robustness with respect to modeling uncertainties are theoretically analyzed and discussed for both case studies. Simulations and experiments are conducted to verify the effectiveness of the human effort reduction. Particularly, EMG signals are used as a metric to show the reduction

¹W. Huo, S. Mohammed, J. C. Moreno, and Y. Amirat, "Lower Limb Wearable Robots for Assistance and Rehabilitation: A State of the Art", IEEE System Journal, vol. 10, no. 3, pp. 1068-1081, 2016.

²S. Mohammed, W. Huo, J. Huang, H. Rifai, and Y. Amirat, "Nonlinear Disturbance Observer Based Sliding Mode Control of a Human-driven Knee Joint Orthosis", Robotics and Autonomous Systems, vol. 75(A), pp. 41-49, 2016.

of the human effort.^{3 4 5}

Chapter 5 proposes a fast gait mode detection method based on a body-worn sensor system to detect different gait modes, such as level walking and stair ascent/descent. A fuzzy logic algorithm is utilized to estimate the likelihoods of gait modes in real time. The proposed fast gait mode detection ensures the possibility of naturally and immediately selecting the appropriate kinematic and kinetic models with respect to each gait mode. The assistive torques that are required for assisting in human motions are calculated in real time. The proposed methods are verified by experiments with the lower-limb exoskeletal assistive robot E-ROWA.⁶

Chapter 6 draws the conclusions of this thesis and recommends future work.

1.5 Contributions of our Work

1. Joint level tracking control strategy:

We develop a terminal sliding model control approach of a knee-joint lower limb exoskeleton based on nonlinear disturbance observer. The proposed tracking control approach is robust with respect to modeling uncertainties and disturbances from the wearer and the environment and is able to guarantee that the tracking error converges to zero in finite time. The use of the nonlinear disturbance observer improves the tracking precision and reduces the chattering effect of the terminal sliding model control. Additionally, we theoretically analyze the stability and convergence of the proposed approach. The experimental results show that the proposed approach significantly improves the tracking performance and quickly eliminates the influence of external disturbances.

2. Intention-based single-task assistive control strategy

To assist individuals with lower limb muscular weakness in accomplishing a desired movement, we develop an active impedance control structure that provides power assistance to the wearer by adapting the impedance of the human exoskeleton system to a desired level that the wearer can easily achieve. We develop a nonlinear observer to estimate the human joint torque, which also indicates the human motion intention. To ensure the accurate tracking of the desired joint trajectory generated by the desired human-exoskeleton impedance model, we further develop a nonlinear disturbance

³W. Huo, S. Mohammed, and Y. Amirat, "Impedance Reduction Control of a Knee Joint Human Exoskeleton System", IEEE Transaction on Robotics, 2016. (Submitted)

⁴W. Huo, S. Mohammed, Y. Amirat, and K. Kong, "Active Impedance Control of a Lower Limb Exoskeleton to Assist Sit-to-Stand Movement", IEEE International Conference on Robotics and Automation (ICRA), 2016, pp. 3530-3526.

⁵W. Huo, S. Mohammed, and Y. Amirat, "Observer-based Active Impedance Control of a Knee-Joint Assistive Orthosis", IEEE International Conference on Rehabilitation Robotics (ICORR), 2015, pp. 313-318.

⁶W. Huo, S. Mohammed, Y. Amirat, and K. Kong, "Fast Gait Mode Detection and Assistive Torque Control of an Exoskeletal Robotic Orthosis for Walking Assistance (EROWA)", IEEE/ASME Transaction on Mechatronics, 2016. (Revised version submitted)

observer-based sliding-mode control for lower limb exoskeletons. Moreover, we apply the proposed control structure to two case studies: assisting in knee joint flexion/extension movements using the EICOSI exoskeleton (i.e., single-joint case) as well as assisting in sit-to-stand (STS) movements using the E-ROWA exoskeleton (i.e., multi-joint case). In the first case, the results show that the original inertia, damping and gravity of the human joint can be efficiently reduced, and the magnitude of the subjects' EMG signals can be reduced by up to 60%. In the second case, we develop a time-varying desired impedance model according to the wearer's STS speed that can be used to indicate the human lower limb motor ability. The results show that the proposed active impedance approach can efficiently estimate the human joint torques and provide appropriate power support to the wearer. To the best of our knowledge, the proposed approach, in which a nonlinear general torque-sensor-less control method is proposed to reduce the human muscular activity using inertia, damping and stiffness compensation, is unique in the field of robot-aided physical assistance.

3. Gait mode based multi-task assistive control strategy

We develop a fast gait mode detection algorithm to identify three common daily living activities such as level walking and stair ascent/descent. Here, the term "fast" means that the transition between gait modes can be detected at the early beginning of a new gait step. To achieve this goal, we use the velocity and position of the wearer's foot as the features. Moreover, we propose a feature update algorithm to ensure accurate feature estimation by combining a zero-velocity detection method and the use of a human kinematic model. Based on the actually estimated dynamic features, we develop a fuzzy logic algorithm to estimate the continuous likelihood of each gait mode. To the best of our knowledge, this is the first attempt to detect the human gait modes using features such as the velocity and position of the wearer's foot during walking. Furthermore, we develop a hybrid power-assistive strategy for a lower limb exoskeleton (E-ROWA) to provide different assistances to the wearer according to the wearer's gait modes. The proposed assistive strategy is an alternative method to the traditional finite-state machine algorithms that switch between different strategies according to the changes in the defined states (e.g., gait modes and phases). The assistive torques of the proposed strategy are directly calculated based on the outputs of all of the assistive approaches and the likelihoods of the associated gait modes and phases. This can provide smooth assistive torques and efficiently avoid sudden changes. The proposed approaches are all evaluated by experiments with the lower limb exoskeleton E-ROWA. The results show that the latency and success rate of the gait mode detection both satisfied the requirements for real-time power assistance, and the exoskeleton could provide efficient assistance for the wearer according to his/her gait modes. The proposed gait mode based assistive approach can be easily achieved, and only low-cost sensors, such as force-sensing resistors, IMUs and angle sensors, are required.

Summary

In this chapter, we briefly introduced the use of lower limb exoskeletons for assistance and rehabilitation purposes by reviewing their prospects, advantages and challenges. The objective of the thesis is to develop control algorithms of lower limb exoskeletons according to the wearer's roles such as passive/active movements as well as locomotive activities. Additionally, the lower limb exoskeletons designed for evaluating our control strategies were presented. The outline of this thesis was illustrated using a three-level structure. Finally, our contributions were summarized as 1) a nonlinear disturbance observer-based terminal sliding model tracking control approach; 2) an intention-based active impedance control structure; and 3) a fast gait mode detection algorithm based power assistance strategy.

2 Overview of Lower Limb Exoskeletons

2.1 Introduction

A wearable robot is usually defined as a mechanical device that is designed around the shape and function of the human body and can be worn by the operator, with segments and joints corresponding to those of the person it is externally coupled with [10]. Exoskeletons and active orthoses are two typical examples of wearable robots. An exoskeleton generally refers to a mechanical device that is used to assist an able-bodied wearer by augmenting his/her strength and endurance [6]. Active orthoses are exactly what their name indicates, orthoses equipped with powered actuations that are usually used to assist patients in totally/partially recovering the motor functions of the neuromuscular and skeletal systems. However, the line between exoskeletons and active orthoses is not clear-cut and is becoming blurrier with the development of wearable robots.

Since the concept of the robotic exoskeleton was proposed and studied in the 1960s, it has attracted increasing interest of the research community. Wearable exoskeletons have been a particular focus of robot research in the last two decades. Initially conceived for military and therapeutic applications [6], the use of wearable exoskeletons is rapidly moving towards assistive purposes where the robot is designed to promote functional activities at home, in the community and in society [11, 12]. They can effectively integrate the cognitive ability of the human being and advantages of robotic devices to assist the wearers in accomplishing their desired activities.

To develop effective, lightweight and safe lower limb robotic exoskeletons that provide transparent physical assistance, three main aspects have been extensively studied by researchers and therapists: mechanical design, control strategies and assessment methods. The above aspects contribute to the crucial elements of the development processes of any sustainable lower limb exoskeleton. The design of the power supplies, electric parts and sensors also play important supporting roles.

In general, the mechanical part of a powered lower limb exoskeleton consists of the actuation,

Chapter 2. Overview of Lower Limb Exoskeletons

the mechanical frame and the human-machine interface. The mechanical design contributes to the basic features of the lower limb exoskeleton such as the wearability, portability, efficiency and safety. During the design, an important consideration for researchers is to ensure the exoskeleton's portability and efficiency of power assistance. To address this question, various exoskeletons have been developed from hydraulic actuator-based ones to artificial pneumatic muscle based ones and from rigid mechanical ones to soft exoskeletal suits. In the meantime, many researchers have raised the importance of taking into account the human body biomechanics during the design of lower limb exoskeletons. For example, if the wearer's gait biomechanics are affected or altered by the exoskeleton, the wearer's efforts may show a significant rise.

The control strategies lie at the core of the lower limb exoskeletons. The main goal of the controller of a lower limb exoskeleton is to *naturally* assist the wearer to achieve his/her desired locomotive activities in coordination with the wearer's lower limb musculoskeletal systems and remaining motor ability. Thus, the principal and fundamental requirement of the controller is to efficiently recognize the wearer's motion intention (e.g., gait mode and joint torque/position/velocity) and adjust the generated torque of the robot actuators in a natural and transparent way. In addition, the controller should ensure the accurate implementation of the wearer's motion intention. This means that the controller must be robust with respect to disturbances from the wearer and the environment. Overall, the control strategy plays an important role in efficiently improving the performance and acceptability of the lower limb exoskeleton.

In terms of the assessment methods, the performance of the mechanical design or control algorithm cannot be evaluated only from an engineering perspective, as the acceptability of the lower limb exoskeleton should be determined by its potential wearers. It has been observed that many devices were abandoned by their wearers because of the enormous physical energy requirement, although many improvements had been done on the design of those lower limb exoskeletons [10, 11]. Hence, it is essential to develop effective and appropriate physiological assessment methods according to the studied applications. The metabolic cost and muscular torque generated by the wearers are among the proposed performance metrics for locomotion-assist lower limb exoskeletons.

In this chapter, we will mainly introduce the control strategies of lower limb exoskeletons presented in the literature, with respect to stand-alone and portable lower-limb exoskeletons/active-orthoses operating in parallel with human lower limbs. Additionally, to provide a comprehensive understanding of the lower limb exoskeletons, a basic overview of the existing exoskeletons is first presented based on a classification of their actuation modes. Finally, some common assessment methods are reviewed.

2.2 Lower-limb Exoskeletons: A Brief Review

Many recent reviews [6, 10, 13] have presented a comprehensive overview of lower limb exoskeletons. Based on the actuation modes of lower limb exoskeletons, a classification method was proposed in our previous study as well [4]. Indeed, the actuation is of crucial significance, since it has a direct impact on the usability of the exoskeletal device in terms of wearability, portability, efficiency and safety. The choice of the actuation mode is mainly associated with the application. For example, hydraulic or pneumatic actuators are usually chosen for the wearer's motor ability augmentation [14], while artificial pneumatic muscle actuators may provide a better solution for power assistance for daily living activities [15]. This section presents a brief review of the lower limb exoskeletons, including those that are mentioned in recent reviews as well as some recently designed novel ones, using actuation mode classification criteria. The characteristics of each class including their advantages and limitations are also discussed.

2.2.1 Exoskeletons with Hydraulic or Pneumatic Actuators

Due to the high power to weight ratios of the hydraulic and pneumatic actuators, they are usually considered suitable choices for exoskeletons designed mainly for human performance augmentation. The Berkeley's lower extremity exoskeleton BLEEX and the Sarcos exoskeleton are two typical examples of this type of exoskeleton, and both were sponsored by the Defense Advanced Research Projects Agency. The goal of these two exoskeletons is to "increase the capabilities of ground soldiers beyond that of a human" [5]. BLEEX also has other potential applications such as helping disaster relief workers, wildfire fighters and emergency personnel carry major loads typically associated with high-demand labor [14, 16, 17]. For the above purposes, the BLEEX and Sarcos exoskeletons are used to support their weight and provide the ability to carry extra loads.

There are seven degrees of freedom (DoFs) in BLEEX (see Figure 2.1(a)), which coincide with the associated DoFs of the human lower limbs. There are four actuated DoFs (flexion/extension at hip, knee, and ankle as well as abduction/adduction at the hip) that require relatively significant torques and are actuated using hydraulic actuators. The required torques to actuate these joints are computed based on the measurement of the human joint torques for ensuring typical human walking gait cycles. Linear hydraulic actuators are used in BLEEX due to their compact size, low weight, and high-force capabilities. The Sarcos second-generation exoskeleton (XOS 2) has been developed into a full-body exoskeleton. A significant difference between the Sarcos exoskeleton and BLEEX exoskeleton is that the Sarcos exoskeleton uses rotary hydraulic actuators that are located directly at the powered joint level of the exoskeleton [5, 18, 19]. In terms of performance, BLEEX has been reported to support up to 75 kg of load (exoskeleton weight plus payload), with a walking velocity of 0.9 m/s and a maximum velocity of up to 1.3 m/s without load [14]. XOS 2 is able to help a person hold a 68-kg payload without feeling the load [14]. These performances clearly show that hydraulic actuators can

supply a high specific power (i.e., high ratio of power to weight) [13, 16]. The rotary ones have a greater internal leakage or considerable friction compared to the linear hydraulic-based actuators [14].

The nurse-assisting exoskeleton (see Figure 2.1(b)) is another exoskeleton prototype that uses pneumatic rotary actuators. This exoskeleton was developed at the Kanagawa Institute of Technology, Japan [20, 21] and was used for assisting a nurse to carry a patient in her arms. It is a full-bodied suit and consists of three power-assisting units (arm unit, wrist unit, and knee unit). Regarding the lower limbs, direct-drive pneumatic rotary actuators are used for the flexion/extension of each knee. The weight of the knee joint actuator is approximately 1.5 kg [20]. Experiments showed that the leg actuator could produce a torque of approximately 15 Nm at the beginning of the stretching, which represents half of the necessary torque (30 Nm) for stretching the knee joint.

2.2.2 Exoskeletons with Electrical Motors

The first known example of an active exoskeleton actuated using electrical motors was designed by M. Vukobratovic *et al.* in 1974 [22]. After that, electrical motors have been widely used in active lower limb exoskeletons, such as the HAL (see Figure 2.1 (c)) [23], Rewalk (see Figure 2.1 (e)) [24], Vanderbilt University exoskeleton (see Figure 2.1 (f)) [25], and H2 exoskeleton [26]. Compared with the hydraulic and pneumatic actuators, the electrical motors are more power-efficient but require a larger size and heavier weight to achieve the same purpose. Hence, if the purpose of the lower limb exoskeleton is not to assist the potential wearers in carrying relatively heavy loads, electric motors are generally more suitable. The advantages of electric actuators include their compact size and relatively admissible weight. Additionally, since the required torques for lower limb exoskeletons and orthoses are relatively high and the speed is relatively low, it is usually hard for direct-drive electric actuators to satisfy the requirements of high torque output, low speed, small size, and light weight simultaneously. Hence, geared-drive and/or cable-drive electric actuators are usually designed to satisfy such requirements.

The Hybrid Assistive Leg (HAL)-5 is a lower limb exoskeleton using electrical motors. It was developed by Sankai *et al.* [23, 27–30] for both performance augmentation and rehabilitative purposes. Each electric actuator consists of a DC servomotor and a harmonic drive gear. These electric actuators can supply the required torques at the hip, knee joints, and upper body joints (elbow and shoulder joints). Due to the use of advanced aeronautical materials and the reduction of the size of the bulky backpack that was present in the previous prototype (i.e., HAL-3), the weight of the current version of HAL-5 has been reduced to 21 kg. Furthermore, since HAL-5 can support itself, the wearer is even not aware of its weight. In terms of performances, HAL-5 can support healthy wearers during standing up, walking, climbing stairs, and a range of other daily living activities. Additionally, it is claimed that HAL-5 can help a healthy adult lift up to 80 kg of load, which represents roughly twice his normal capability (30-40 kg) without

assistance [5]. This means that HAL-5 can support payloads of approximately 40 kg. It should also be noted that the endurance of the wearers cannot be improved significantly using HAL-5, as they quickly become tired when holding a heavy load.

The Rewalk¹, Vanderbilt-designed Indego exoskeleton² and Ekso exoskeleton³ are three commercial lower limb exoskeletons that are mainly designed to assist both spinal cord injury and stroke patients in daily walking. Note that Rewalk and the Indego exoskeleton have received (U.S. Food and Drug Administration) FDA clearance for both clinical and personal use in the United States. These three exoskeletons are all actuated using electric motors. At the hips and knees of these three exoskeletons, electric motors are used to assist in the wearer's joint flexion and extension movements. Each knee motor of the Vanderbilt exoskeleton is additionally equipped with an electrically controllable normally locked brake, which consists of a spring-loaded solenoid, such that the knee joints remain locked in the event of a power failure [9]. The ankle joints of the Rewalk and the Ekso exoskeleton are all passive, while there is no ankle joint part in the Vanderbilt exoskeleton.

Ohta *et al.* [31] presented a 2-DoF motor-powered gait orthosis for spinal cord injury patients. An important feature of this orthosis is related to its use of linear motor actuators at the knee and hip joints as a combination between DC motors and ball screws. The increase of the moment arms results in an enhancement of the output torque, while the size of the actuator remains relatively small. The masses of the knee and hip joints are only 0.8 and 1.4 kg, respectively. Consequently, the required power supply can be reduced.

2.2.3 Exoskeletons with SEAs

Using traditional non-backdrivable actuators (e.g., electric motors) in some wearable robots showed certain inherent limitations, such as a poor torque density of the motors at low speed as well as friction, backlash, torque ripple, and noise of the gears. In recent studies, researchers have tried to develop a novel type of actuator to remedy these problems. Serial Elastic Actuators (SEAs) were developed for this purpose.

Compared with the non-backdrivable actuators, the SEA presents several advantages such as shock tolerance, lower reflected inertia, more accurate stable force control in unconstrained environments, and energy storage [32, 33]. Recently, the SEA has been used in many exoskeletons and orthoses. In this section, only the active SEAs are reviewed; therefore, some passive SEAs are not included, e.g., the MIT exoskeleton [34] and the ankle exoskeleton developed by Sawicki *et al.* [35], as they only control the energy storage and release without providing actuation.

The MIT active ankle-foot orthosis (AAFO) [36] uses SEA-based actuators to compensate for

¹<http://rewalk.com>

²<http://www.indego.com>

³<http://eksobionics.com>

the patient foot drop. Regarding the structure of the AAFO, a SEA is attached to a conventional ankle-foot orthosis. The total weight of the AAFO is 2.6 kg, excluding the weight of an off-board power supply. The SEA consists of a DC motor powered ball screw mechanism in series with helical springs. It can adapt the impedance of the ankle in plantar flexion during stance and assists in dorsiflexion during the swing phase of the walking gait cycle based on the measurement of the ground force and joint kinematics [6]. In terms of performance, the AAFO showed significant effectiveness in assisting drop-foot patients. The experimental results showed that the AAFO has three benefits: reducing the occurrence of slap foot, allowing greater plantar flexion, and proving relatively similar swing phase ankle kinematics to the normal state [36]. Another powered ankle-foot orthosis, actuated by a SEA-based robotic tendon, was developed by researchers at the Arizona State University, Phoenix, USA [37, 38]. The robotic tendon uses a screw/spring/motor arrangement. A comparison study between the effectiveness of the robotic tendon and that of the traditional direct-drive system showed that, in an ideal example, the peak power required at the ankle joint level when using the robotic tendon is 77 W, while it is 250 W when using the direct motor. This result can be explained by the fact that the robotic tendon can store and release energy during cyclic repetitive tasks. Additionally, the weight of the robotic tendon is just 0.95 kg (the latest version is only 0.5 kg), which is seven times less than that of its equivalent motor/gearbox system. Moreover, the ideal energy requirements are reduced from nearly 36 to 21 J. This means that an orthosis using the SEA can be more portable, lightweight, and efficient.

Wang *et al.* [8] designed an SEA-actuated lower limb exoskeleton, MINDWALKER, which is used to support SCI paraplegics to walk (see Figure 2.1 (g)). There are three DoFs at the hip joint level (abduction/adduction, flexion/extension and rotation), one DoF at the knee joint level, and two DoFs at the ankle joint level (dorsiflexion/plantarflexion and inversion/eversion). The abduction/adduction and flexion/extension of the hip joints and the flexion/extension of the knee joints are powered using designed SEA actuators. Each SEA actuator, which consists of a spiral spring, a lever arm and a linear actuation, can deliver 100 Nm torque and 1 kW power. Due to the use of the high torque-to-weight ratio SEA, the total weight of the exoskeleton is 28 kg, while the weight of each SEA is 2.9 kg.

Different types of SEA have been designed with the development of wearable robots. For example, Veneman *et al.* [39] developed a series elastic and Bowden-cable-based actuation system. Although the main purpose of this actuator is to support the power source for a stationary robotic trainer LOPES, it might have wider application in wearable exoskeletons. The highlighted characteristic of this actuator is that it introduces Bowden cables in the design of the SEA to detach the actual motor from the exoskeleton frame. This can lead to a more portable exoskeleton frame. In terms of performance, this actuator shows advantages in three important aspects of wearable robots: bandwidth of force training, reduction of the output impedance, and force fidelity. The bandwidths for the full force range and smaller range are 11 and 20 Hz, respectively, while the corresponding required frequencies, which are obtained by studying the human gait cycle and the motion control range of a human therapist, are 4 and 12 Hz, respectively. The impedance output can be reduced to an almost

imperceptible level. The fidelities for tracking 2- and 20-Hz sinusoidal trajectories are 98.7% and 94.7%, respectively. Novel types of SEA, such as those developed in [40–42], are continually developed to mitigate some of the drawbacks of SEAs such as friction and weight reduction and compliance improvement.

2.2.4 Exoskeletons with Pneumatic Muscle Actuators

The original concept of the pneumatic artificial muscle was presented by McKibben for prosthetic applications in the 1950s [43]. The pneumatic artificial muscles are very simple to manufacture and can be used in an antagonistic form similar to that of the human skeletal muscles. The pneumatic artificial muscle is widely considered as an efficient actuation mode for wearable exoskeletons due to its specific characteristics, such as high power/weight ratio, relatively light weight, and inherent compliance. Moreover, they are very safe and suitable for rehabilitation purposes due to their inherent compliance and limited maximum contraction [44].

Caldwell *et al.* [45] developed a lower body 10-DoF exoskeleton for actively assisting in human walking with the use of artificial pneumatic muscles as actuators (see Figure 2.1(h)). There are 3 DoFs at each hip joint level, 1 DoF at each knee joint level, and 1 DoF at each ankle joint. Artificial pneumatic muscles are used to provide a flexion/extension torque at each active joint. Due to the use of pneumatic muscles, the resulting exoskeleton is very portable, and the total weight (excluding the power source) is less than 12 kg. Sawicki *et al.* [15, 46] developed a powered lower limb orthosis for motor adaptation and rehabilitation purposes using artificial pneumatic muscles to provide flexion and extension torques at the associated joints. Experiments show that this lower limb orthosis can supply a substantial plantar flexor torque: ~ 57 % of the peak ankle plantar flexor torque during stance and ~ 70 % of the plantar flexor torque generated during normal walking [15]. By observing the EMG activities of the soleus muscle from initial use to 30 min of walking with healthy wearers, it was shown that the soleus EMG amplitude was reduced by 50 % and tended to the normal level [15].

However, there are some drawbacks of using artificial pneumatic muscles. For instance, their control bandwidth is relatively low compared to that of hydraulic actuation. This is because the hydraulic fluid is generally incompressible, while the pneumatic muscles use compressible air.

2.2.5 Other Exoskeletons

There are also some actuation designs that integrate the characteristics of two or more types of previously mentioned actuators. For example, Saito *et al.* [47] developed an externally powered lower limb orthosis that is actuated using a bilateral-servo actuator. This actuator consists of two cylinders that can simulate the characteristics of the human muscles. It is also operated by the antagonistic action of sealed oil, which is controlled using a servomotor.

Chapter 2. Overview of Lower Limb Exoskeletons

Hence, this actuator combines the advantages of both the hydraulic and electrical actuators.

In addition, novel types of actuation are constantly being developed. For example, Haines *et al.* [48] proposed a novel low-cost high-strength artificial muscle from fishing lines and sewing thread. The output force changes in response to the temperature, and the performance of the artificial muscle matches or even exceeds that of the skeletal muscle in certain aspects, such as a lack of hysteresis, long life, and high output power [48].

Some new concepts with respect to the exoskeleton's design have also been recently proposed. For instance, researchers in the Harvard Biodesign Lab developed a soft exosuit for assisting in ankle plantarflexion and hip flexion (see Figure 2.1(d)) [49]. It consists of a spandex base layer, a waist belt, a calf wrap on each leg, and two vertical straps per leg. No rigid mechanical frames are used in this suit. An off-board motor-based actuation is designed to further reduce the load applied to the wearer, which makes the exosuit very portable.

2.2. Lower-limb Exoskeletons: A Brief Review



Figure 2.1 – Examples of the existing assistive lower limb exoskeletons with respect to actuation modes. (a) the BLEEX exoskeleton [16] (hydraulic actuation), (b) the nurse-assisting exoskeleton [21] (pneumatic actuation), (c) HAL-5 [50] (electrical-motor-based actuation), (d) the Soft Exosuit [49] (electrical-motor-based actuation), (e) the Rewalk [24] (electrical motor-based actuation), (f) the Vanderbilt University exoskeleton [25], (electrical-motor-based actuation), (g) the MINDWALKER [8], (SEA actuation), (h) the exoskeleton designed by Costa *et al.* [45] (artificial pneumatic muscle based actuation).

2.3 Control Strategies

Recalling that the main goal of lower limb exoskeletons for mobility assistance is to provide power assistance during the wearer's daily living activities by naturally and seamlessly integrating the wearer's sensor-motor capability, it is necessary to develop multilevel control strategies including appropriate detection algorithms of human intention, power assistance strategies and joint-level control approaches (e.g., motor control). For each aspect, much work is presented in the literature. Our previous review [4] provides an overview of the control strategies of lower limb exoskeletons based on the types of human-robot interfaces used. Regarding the joint-level control approaches, a huge number of existing control theories (e.g., PID control, sliding mode control, and adaptive control) can be selected according to the specific control objective. A recent review presented by M. R. Tucker *et al.* ([7], 2015) proposed a general control framework to investigate and classify the state-of-the-art control strategies for active lower limb prosthetics and orthotics. In this framework, a hierarchical control structure is defined, which consists of three layers: a perception layer for the wearer's motion intention estimation such as activity mode and human volitional intention; a translation layer for converting the wearer's intention to the desired device state outputs; and an execution layer for achieving the desired device states (see Figure 2.2). According to this hierarchical structure, the three control strategies presented in Section 1.4 (i.e., Scope of the thesis) are classified as follows: reference tracking control algorithms belong to the execution layer, while the active impedance assistance strategy and gait mode detection based torque assistance control strategy are direct volitional intention based and a gait mode based three-layer control strategies, respectively. In the following section, the control strategies in the literature are grouped into two categories: direct intention-based control algorithms and gait-mode based control algorithms, and their perception and translation layers will subsequently be reviewed. Finally, reference tracking control approaches that are generally used as execution layers for both categories cited above are introduced.

2.3.1 Direct-intention based Control Algorithms

Direct intention-based control is a strategy that provides assistance to the wearer to achieve a desired movement by enhancing his/her delivered motor ability using the lower limb exoskeleton. From the wearer's perspective, it is a human-in-loop control strategy. The states of the lower limb exoskeleton are directly and voluntarily controlled by the wearer. Regarding the design of the control algorithms, a primary issue is to estimate the wearer's volitional outputs (i.e., motion intention). This raises two questions: what type of wearer's volitional output can be used, and how can it be estimated? In the literature, the joint torque and impedance generated by the wearer are widely used as volitional outputs. In terms of the estimation of the joint torques/impedances, an EMG signal is an intuitive means to estimate the wearer's net joint torque and impedance, since it is directly measured from the wearer and appears prior to the human movements. Additionally, the wearer's net joint torques can be estimated using the force/torque sensors as well as model-based methods (e.g., inverse dynamic model).

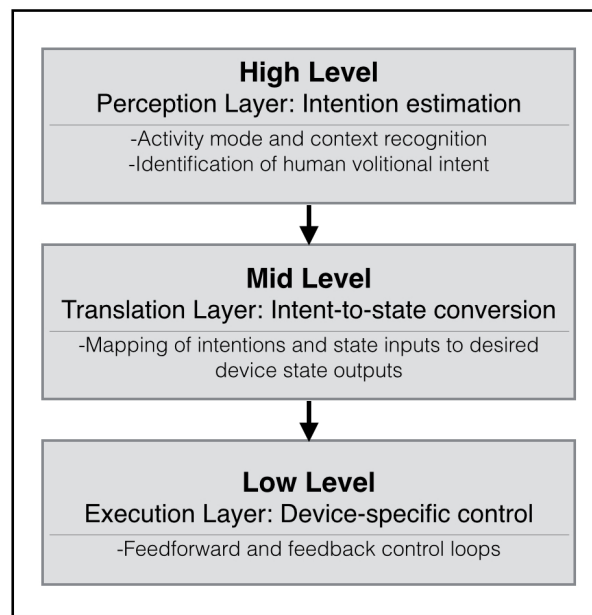


Figure 2.2 – Hierarchical control structure of exoskeletons/orthoses [7]

A. Estimation of the Human Motion Intention

Electromyography (EMG): To estimate the wearer’s net joint torque, one method is to build a proportional or polynomial relationship directly between the wearer’s net joint torque and the EMG signals [46, 51]. For example, D. P. Ferris *et al.* [46] proposed a proportional myoelectric control of a powered ankle-foot orthosis driven by artificial pneumatic muscles. The air pressures in the artificial pneumatic muscles are proportional to the processed muscle activation patterns measured from the soleus and tibialis anterior.

Moreover, the wearer’s net joint torque can be calculated using a musculoskeletal model based on the measurement of EMG signals from the corresponding muscles [52–55]. This method necessitates a prior calibration process, which usually requires an accurate model, parameter identification, important computational efforts and experimental setting processes for measurements. For instance, researchers from the Berlin University of Technology, Germany [53–55]), proposed a method to calculate the human walking intention for an exoskeleton by combining EMG signals and a human musculoskeletal model. The human body model consists of two legs with feet, shanks, thighs, and a torso. The EMG signals measure the muscular activities responsible for the flexion and extension of the knee joint (semimembranosus and vastus medialis). In addition to the EMG sensors, pose sensors are also used to obtain the postures of the wearer. The EMG data are processed using an EMG-to-force function to estimate the intended forces. An online calibration method was also proposed by iteratively optimizing the desired torque towards the torque calculated using the inverse dynamics of the human body model. The experimental results showed that the curve of the torque calculated using EMG data matched well that computed using inverse dynamics during

Chapter 2. Overview of Lower Limb Exoskeletons

free daily living activities, such as walking and climbing stairs.

The wearer's joint impedance can also be estimated using EMG signals measured from the antagonistic muscles. Hence, the wearer's joint impedance can be mapped to the lower limb exoskeletons. Karavas *et al.* [56] proposed a tele-impedance assistance approach of a knee exoskeleton for assisting the wearer in achieving successful sit-to-stand movement. The wearer's net knee joint torque and stiffness are estimated using EMG signals measured from the extensor (rectus femoris, vastus medialis and vastus lateralis) and flexor (biceps femoris, semimembranosus and semitendinosus) muscles.

Although EMG signals have been widely used to estimate the human intention prior to the exoskeleton control, there are still some inherent limitations during practical application that need to be solved in the future. For example, the EMG signals are easily influenced by the electrode placement, neighboring muscle signals and noises that affect the original EMG recordings. Additionally, novel methods need to be proposed to simplify the calibration procedure of the EMG signals, since they may change considerably from wearer to wearer and day to day.

Inverse Dynamics Methods: The wearer's joint torques can be estimated using the inverse dynamic model based on the joint kinematics and external torques acting at the joint levels [57, 58]. The joint kinematics can be measured using inertial measurement units (IMUs) or angular sensors (e.g., encoders) embodied in the lower limb exoskeletons. The external torques mainly include the assistive torques of the exoskeleton and the torques generated by the ground reaction forces. Usually, this method is highly effective for the cases in which the dynamic model is invariant, for example, swinging the lower limb. However, it should be noted that the lower limb dynamic models are variable with the changes of the foot contact conditions during daily living activities such as walking. To estimate the lower limb joint torques during walking activities, different dynamic models are required according to the foot contact states. To address this problem, Kong *et al.* [58] proposed a method to seamlessly integrate the outputs of the different inverse dynamic models built for the respective gait phases using a fuzzy logic algorithm.

Forceltorque Sensors: In addition to the EMG and inverse dynamics, the ground reaction forces (GRFs) can be applied to estimate the wearer's joint torques [58, 59]. The GRFs and the center of pressure can be estimated using force sensors or force-sensitive resistors (FSRs) that are attached to the shoe sole. Based on this information, the ankle joint torque can be calculated. Sequentially, the knee and hip joint torques can be estimated by combining the kinetic and potential energies of the shank and thigh, respectively [59]. The accuracy of the joint torques estimated using this method largely depend on the precision of the GRF measurement. Since the GRFs, especially the shear force, are difficult to accurately measure using the existing commonly used sensors, it is not possible to accurately estimate the human joint torques using GRFs in practice. Furthermore, the interaction force/torque between the wearer's limbs and the exoskeleton also provides an approach to explicitly infer the wearer's

motion intention [60].

B. Intention-based Control Strategies

Once the wearer's joint torque or impedance (i.e., the wearer's intention) is estimated using the aforementioned methods, an appropriate control strategy for the lower limb exoskeleton is needed to provide power assistance in coordination with the wearer's efforts. One method is to directly augment the wearer's torque. For example, Kong *et al.* proposed a concept named fictitious gain that is designed to increase or decrease the sensitivity of the human body. If the fictitious gain is larger than one, the human is assisted using the lower limb exoskeleton and is able to perform the desired motions with lower muscular forces. Correspondingly, a robust frequency-shaped fictitious gain design method was presented. Based on the designed fictitious gain, a linear controller for exoskeletons can be easily obtained to implement the fictitious gain. Another straight-forward method for designing the control approach of the lower limb exoskeleton is to generate a reference joint position, velocity or acceleration based on the estimated human torque. In [61], the authors designed a positive feedback control system for the BLEEX exoskeleton by increasing the closed loop system sensitivity to the wearer's forces and torques. A sensitive function is proposed to generate the exoskeleton velocity. The advantage of this method is that no measurement from the wearer (such as force, position, or electromyogram signal) is required, while the control system is also sensitive to parameter variations and therefore requires a relatively good dynamic model of the system. Fleischer *et al.* [54, 55] developed an intention-based control approach of a knee joint orthosis in which the desired angular accelerations of the knee joints are calculated using the forward dynamics of the human body model based the estimated joint torques. The angular acceleration is then set as the reference of the orthosis.

Impedance control also provides an effective solution for the intention-based control of lower limb exoskeletons. In [56], the authors mapped the estimated human knee joint impedance to a knee joint lower exoskeleton. A reference motion intention is obtained by integrating the estimated knee joint torque over time, and the assistive torque is generated based on the intention tracking error and the estimated human joint stiffness. Ollinger *et al.* [60, 62–64] proposed an active impedance control strategy of a lower limb exoskeleton to increase the agility of the wearer's movements. Considering the fact that the wearer's limb and the exoskeleton are rigidly connected, the mechanical impedance of the lower limb can be modulated using the active impedance of the exoskeleton. The measured interaction torque exerted on the exoskeleton by the wearer is measured using force sensors and used as the input of a desired active impedance model. Hence, a reference angular trajectory is generated by the desired impedance model.

2.3.2 Gait-mode based Control Algorithms

To realize continuous and smooth transitions between different power-assist strategies, the continuous and smooth detection of the different gait modes is critical. In the gait mode

detection, two important criteria should be addressed: the detection latency and the success rate of detection [7]. The transition between gait modes should be detected immediately and accurately; otherwise, the control algorithm of a wearable may result in an incorrect or delayed assistive torque generation, and then, increase the fall risk. In these aspects, various gait mode detection methods have been developed in the literature, from simple manual switching strategies to training-based methods [65, 66]. Although the manual switching methods, such as pushing a button [65] or conducting some finger or arm movements [28], are an effective and practical solutions for the gait mode transition, in particular for patients with complete paraplegia, although the wearer should be thoroughly educated to operate the wearable robot, such manual switching methods are bothersome for people with partial impairments who must use crutches.

For detecting the gait modes without any extra input devices (i.e., the above-mentioned manual means), various recognition methods have been proposed. They are classified according to the used sensor systems (e.g., brain control interface (BCI), EMG, and force/position sensors) and the types of implemented detection algorithms (i.e., rule-based ones and machine learning based ones) as follows.

A. Sensor Systems for Gait Mode Detection

Brain Control Interface (BCI): The BCI can be subdivided into two main categories: the invasive brain-machine interface and the noninvasive one. The surface and noninvasive brain-machine interface based on the field potentials is more commonly used in practical control for robot-based rehabilitation purposes. The electroencephalogram (EEG)-based interface is considered as a primary form of noninvasive brain-machine interface. In the last decade, great progress has been made in the use of the EEG to control exoskeletons [67–72]. Many studies have been conducted on utilizing the EEG-based interface in exoskeletons and active orthoses. For instance, the BETTER project aimed to improve the physical rehabilitation of patients with gait disorders caused by spinal cord injury, stroke, or amyotrophic lateral sclerosis using exoskeletons/orthoses and brain signal measurements [73, 74]. In this project, EEG signals are used to generate discrete commands, such as the intended action [75, 76], while EMG signals are also used for controlling the lower limb exoskeleton.

Although much convincing evidence shows that it is feasible to use EEG-based interfaces to control wearable robots, there are still some limitations facing the use of EEG-based interfaces while estimating the human motion intention. These limitations mainly relate to the relatively high sensitivity, the shortcomings of the wearable EEG measurement equipment, the overlapping of the different electrical activities generated by different cortical areas, and the balance between the training time and accuracy [71, 77].

Electromyography (EMG): The EMG signal is one of the most useful means to detect the gait mode [4, 7]. The EMG appears prior to the mechanical motion due to the response time of the musculoskeletal system, so the gait mode detection using EMG signals has a short latency. In the above-mentioned direct intention-based control, the EMG signals are used to estimate the

wearer's net joint torques or joint impedance. However, here, the patterns of the EMG signals are directly used to estimate the wearer's intended gait modes based on classification methods such as neural networks [78] and linear discriminant analysis [7].

Force and Movement Sensors: Ground reaction forces have been used to estimate gait modes such as standing, sitting and walking in many studies. For instance, a control strategy of the exoskeleton HAL-3 was proposed to estimate the wearer's locomotive activities (i.e., standing, sitting and walking) using the ground reaction forces and hip and knee joint angles [79, 80]. In [9], the shift of the user's center of pressure was used to estimate twelve defined states among three gait modes, walking, sitting and standing, with the use of the Vanderbilt University Exoskeleton. The transitions between these states are inferred based on the distance of the user's forward foot and the horizontal projection of user's center of pressure, which can be affected by the user's upper body. It should be noted that there are no foot pressure/force sensors in the Vanderbilt University Exoskeleton. Hence, the user's center of pressure is calculated using a human full body model with all lower limb and torso inclination angles.

Apart from the ground reaction forces, the wearer's limb positions and joint angles are also used to estimate the gait modes. Li *et al.* [81] proposed a gait mode detection method for an ankle-foot orthosis by tracking the 3D position of the wearer's foot using an IMU. Yuan *et al.* [82] introduced a fuzzy logic-based method to detect the ground condition during the stance phase of a prosthesis using features such as the rising time of the GRF at heel level, sequence of foot strikes on the ground, foot inclination angle during stance, shank inclination angle at toe-off and maximal shank inclination angle during swing.

Environmental Sensing: The human gait modes can be estimated according to walking terrains that are directly detected using environment sensors such as laser and sonar. Zhang *et al.* [83] developed a wearable terrain recognition system using a laser distance sensor and IMUs. The laser distance sensor is placed on the wearer's waist to calculate the slope of the terrain in front of the wearer and the rate of terrain height changes, while the IMUs measure the position and orientation of the laser distance sensor and the wearer. Based on these measured features, the types of terrains (i.e., level terrains, up/down ramp, up/down stairs and obstacle) are recognized using threshold-based algorithms. Kleiner *et al.* [84] used a two-dimensional laser scanner and an inertial navigation unit on a prosthesis to measure the distance to the structure in a two-dimensional plan and to estimate the current three-dimensional position and orientation of the prosthesis.

However, in practice, the relationship between the terrain and the human walking intention should be considered within the control strategy framework of the powered exoskeleton [7]. Additionally, the relatively high cost and the sensor's vulnerability to features constitute the main limitations for using such technology [82].

B. Gait Mode Detection Methods

Heuristic Rule-based Methods: The principle of the heuristic rule-based methods is that given

the set of all possible gait modes, the designer identifies a fixed set of rules that indicate the transition among the gait modes [7]. These rules can be built using simple threshold-based methods or advanced algorithms (e.g., fuzzy logic methods). Due to its ease of implementation, the rule-based gait mode detection methods have been widely used in existing exoskeletons [7]. Li *et al.* proposed a threshold-based automatic gait mode recognition method for an ankle-foot orthosis by tracking the 3D position of the wearer's foot using an IMU [81]. Yuan *et al.* introduced a fuzzy logic-based method to detect the ground condition during the stance phase of a prosthesis [82]. However, the latency is yet a critical challenge for the threshold-based or rule-based methods [7]. Most of the currently developed methods detect the gait mode based on the human state (e.g., GRFs or joint angles) when the human feet contact the ground, which causes up to a step or stride delay.

Machine Learning Based Methods: In general, there is a problem of efficiency when rule-based methods have a large number of rules or features, since all their parameters should be tuned manually and designed for each wearer. To address this problem, various machine learning methods, such as linear discriminant analysis [66] and vector analysis [85], have been proposed to accurately detect the gait modes. The significant advantages of such methods are that a relatively large number of features can be used and the optimal feature values can be quickly obtained. On the other hand, these methods require a set of training data for the different gait modes, which usually hinders their application in practice [7].

C. Finite State Machine Based Control Strategies

Since the lower-limb kinematic and kinetic characteristics significantly vary with the gait motions, the control algorithms for the exoskeletons should take the different gait motions into account. A recent review shows that finite-state control has also been a very popular control strategy for lower limb exoskeletons [7]. In this approach, different assistive strategies are selected according to the states (e.g., gait phases and gait modes) detected by a dedicated motion detection algorithm. For example, in [86, 87], the authors presented a control method for assisting paraplegic patients using joint reference trajectories. Control gains (PD control) are selected for twelve states of sitting, standing and walking. In [50], different assistive strategies were employed to assist complete paraplegic patients during sit-to-stand and stand-to-sit activities using the robot suit HAL. Other finite-state control strategies of lower limb exoskeletons have also been proposed based on the wearer's gait phases [6, 8, 9, 78, 86, 88, 89].

2.3.3 Reference Tracking Control Algorithms

To achieve the satisfactory tracking of the desired states that are generated by the aforementioned intention-based strategies or imposed by the therapists, low-level control algorithms are required. The desired states could be reference angular trajectories, joint torques or joint impedances. An important metric to assess the low-level control algorithms is the tracking performance (i.e., tracking precision). Given that the exoskeletons are in contact with the wearer and environment, the stability and robustness with respect to external disturbances

should be taken into account during the design of the low-level control methods.

The low-level control can be considered as a specific application of classical control techniques. For example, feedforward control [89], proportional derivative (PD) control [27], adaptive control [90], impedance control [56], and sliding mode control [91] have been widely used in existing lower limb exoskeletons. The performance characteristics and stability of the aforementioned control strategies can also be analyzed using traditional analysis methods such as the transfer function, Nyquist stability criterion, and Lyapunov stability analysis.

To improve the robustness with respect to disturbances that come from the wearer, the exoskeleton (e.g., friction) and the environment, one common solution is the use of high-gain controllers (e.g., sliding mode control); recently, another solution has been proposed by researchers: disturbance-observer (DOB)-based control strategies. The disturbance is estimated using a model-based observer and is directly compensated in the controller. Kong *et al.* [41] proposed a linear DOB-based PID controller of a SEA actuator to achieve the fast and accurate tracking of the reference torque. Chen [92] proposed a nonlinear DOB design method for a nonlinear control system that can be used to control a multi-joint lower limb exoskeleton.

2.4 Assessment Methods

To date, various methods to assess the performance of lower limb exoskeletons have been presented. Most of these methods fall into three main categories: metabolic cost, gait biomechanics and muscular activity analysis. In this section, we review some major physiological assessment methods that have been used in exoskeleton studies. Additionally, we will discuss the effectiveness of the robotic devices as determined by these assessment methods.

2.4.1 Metabolic Cost

For augmented-performance exoskeletons, an efficient performance assessment method is to compare the metabolic energy expenditure of the user while walking with and without the use of the exoskeleton. The oxygen consumption, carbon dioxide production and urinary nitrogen excretion are the basic measurement means, as presented in some studies [93–95].

The MIT exoskeleton project [96] is considered to be the first reported study that compared the metabolic cost while the user was walking with and without the assistance of the exoskeleton. It was reported that the metabolic expenditure was higher by 10% when the exoskeleton was worn. Similar results were obtained from other research studies. K. N. Gregorczyk *et al.* [97, 98] studied the effects on the metabolic cost when carrying loads using a lower-limb exoskeleton prototype. Nine US Army participants were asked to walk at 1.34 m/s on a 0% grade for 8 minutes while carrying loads of 20 kg, 40 kg and 55 kg with and without the exoskeleton. The mean oxygen consumption significantly increased by 60% (body mass) and 40% (body mass

Chapter 2. Overview of Lower Limb Exoskeletons

and exoskeleton mass) when the participants wore the exoskeleton compared to the normal condition without wearing the exoskeleton. This study also analyzed the reasons for this increase in the energy expenditure: the changes in the wearer's gait and walking pattern were thought to be primarily responsible.

There are also some lower limb orthoses that have been reported to reduce the metabolic cost to the user while walking. For instance, G. S. Sawicki *et al.* [99] used an ankle exoskeleton to study the metabolic cost of plantar flexor mechanical efforts exerted during walking with different step lengths at a constant frequency. The exoskeleton is powered by artificial pneumatic muscles and controlled through EMG signals. In this study, nine healthy subjects participated in experiments, and the results show that the exoskeleton slightly altered the user's ankle joint kinematics during walking for all speed/step-length conditions. In this case, the net metabolic power ($6.19 \pm 0.29 \text{ W kg}^{-1}$) with the assistance of the exoskeleton is significantly lower than that for walking without the exoskeleton ($7.18 \pm 0.50 \text{ W kg}^{-1}$) at a 1.75 m/s walking speed. However, as the speed became slower (at the same stride frequency, only reducing the stride length), the effectiveness of reducing the wearer's metabolic cost decreased. Although some single-joint powered orthoses have been demonstrated to reduce the metabolic cost in certain conditions, most studies have shown that the metabolic cost is still higher when the wearer is walking with the assistance of the lower limb exoskeleton and/or a load. This is a common problem in lower limb exoskeleton studies, and further explorations need to be conducted in the future, in particular on the design issues and the actuation.

2.4.2 Gait Biomechanical Analysis

Gait biomechanical analysis is another important assessment method, especially for rehabilitation purposes. The main features that are used as assessment criteria are the gait kinematics and temporal-spatial gait variables. The gait kinematics is direct and meaningful for the joint control and performance evaluation. Temporal-spatial variables such as the speed, walking distance, step length, and cadence are frequently used as well. This assessment method is the one most commonly used to evaluate the effects of lower limb exoskeletons and orthoses on gait functions.

Y. Ohta *et al.* [31] developed a two-DoF motor-powered gait orthosis for spinal cord injury patients. The gait biomechanics (e.g., stability, gait speed and step length) were used to assess the performance. Five male patients with complete spinal cord injury took part in this study. After a period of training with the gait orthosis, their gait speed and length showed certain increases (from 3%-23% and 0%-7%, respectively). At the same time, the stability and dynamics of the walking were also improved, while the lateral and vertical compensatory motions showed small decreases.

Clinical experiments were conducted to evaluate the performance of the active ankle-foot orthosis (AAFO) developed by Herr *et al.* [36]. Three drop-foot participants and three normal subjects took part in this study. Kinematic and kinetic data were collected to analyze and

compare the six subjects' occurrences of slap foot, swing dorsiflexion angular range/power plantar flexion angle and gait symmetry. Three different control conditions were evaluated: zero, constant and variable impedance. The zero impedance was meant to approximate the unassisted drop-foot gait and constant impedance to imitate the conventional ankle-foot orthosis. The results showed, when compared to the zero and constant-impedance control schemes, that the occurrence of slap foot in the drop-foot participants was reduced and the swing dorsiflexion angular range and maximum plantar flexion angle were increased upon actively adjusting the joint impedance. The swing phase ankle kinematics was close to the physiological pattern. It was also found that the variable-impedance controller improved the spatial and temporal gait symmetry by comparison to the zero-impedance controller, while there was no significant difference between the effectiveness of the variable-impedance and constant controllers.

Gait biomechanical analyses were also considered using exoskeletons/powering orthoses, such as the HAL exoskeletons [23], the powered gait orthosis developed by S. Kang *et al.* [100] and the Lokomat gait orthosis [101]. Most of these studies have shown that the exoskeleton/active-orthosis has the advantages of improving the patients' gait abnormality and stability. It should be noted that many studies have shown that while the gait biomechanics can be improved by using rehabilitation exoskeletons for the elderly or infirm, the same result is not obtained when using exoskeletons for performance augmentation. There have also been some studies on lower limb exoskeletons, which demonstrated that the wearer's gait biomechanics could be negatively altered when walking with some exoskeletal devices. For example, K. N. Gregorczyk *et al.* [98] found that the kinematics and the kinetics of the wearer's walking patterns (healthy subjects) were all negatively altered.

2.4.3 Muscle Activity Analysis

The averages levels of the muscle activation can be used to assess the performance of the lower limb exoskeleton, as it expresses the contribution of the wearer to the task execution and consequently the assistance performance. This assessment method was used for the evaluation of the HAL-3 exoskeleton for assisting healthy wearers during tasks such as walking, standing up and ascending stairs [23]. The results show that the activation levels of the wearer's muscle decreased for each type of activity when the user was assisted by the HAL-3. This means that the user employed a lower force/torque to perform the same activities. Similarly, the EMG signals have been widely used to evaluate the change of human effort when the human are assisted using lower limb exoskeletons [64, 102, 103].

H. Akahira *et al.* [101] used the muscle EMG activities to assess the effectiveness of a motor-assisted knee motion device for the orthotic gait. Six paraplegic persons with traumatic SCI participated in this study. For comparison, two reciprocal gait orthoses (an advanced reciprocating passive gait orthosis (ARGO, Steeper, Inc., UK) and an improved powered orthosis) were evaluated. It was found that the amplitudes of the EMG activity in the gastrocnemius

and rectus femoris muscles were enhanced and prolonged significantly by the dynamic knee motion accomplished with the assistance of the powered orthosis. This clearly means that the active orthosis has the potential to activate the neuromuscular function of paralyzed lower limbs.

2.5 Discussion

Based on the aforementioned review of the existing lower limb exoskeletons, it is noted that motor-actuated exoskeletons, especially the SEA-actuated ones, have been widely used for rehabilitation and power assistance purposes. This is mainly due to their promising features such as compact mechanical design, high efficiency, and low impedance. In this thesis, the motor-actuated knee joint exoskeleton EICOSI and the SEA-actuated lower limb exoskeleton E-ROWA were developed to assist individuals suffering from muscular weakness.

To efficiently assist the wearer in achieving daily living activities, researchers have developed various control strategies with respect to the following three layers: a perception layer to estimate the wearer's motion intention such as activity mode and human volitional intention; a translation layer to convert the wearer's intention into the desired exoskeleton state outputs; and an execution layer to achieve the desired states. As discussed in Section 2.3, direct volitional intention based control is more suitable for single-task assistance, while gait mode detection algorithms provide a suitable solution to select different assistive strategies according to the wearer's locomotive activities. To implement these two strategies, a joint-level reference control strategy is essential. In this thesis, we will address these three aspects by considering the following goals:

1. To develop a low-level control approach of a lower limb exoskeleton that is sufficiently robust with respect to disturbances.
2. To propose a direct volitional intention based control strategy to assist the wearer in performing single-task daily living activities with minimum sensing measurement from the wearer. Additionally, the control strategy should be generalized to be easily used for different daily living activities.
3. To design a gait mode detection algorithm that is able to seamlessly estimate the wearer's daily living activities such as level walking and stairs ascent/descent. Based on the gait mode detection, a transition-layer control approach is also needed to generate smooth and appropriate assistive torques for the wearer.

The design of effective assessment methods is also crucial for evaluating the practical performance of the lower limb exoskeletons. Hence, appropriate assessment methods need to be designed for the proposed control strategies. Correspondingly, the effectiveness of the proposed approaches should be verified by experiments based on the associated assessment methods.

Summary

In this chapter, a general overview of lower limb exoskeletons was presented considering three main aspects: design, control strategies, and assessment methods. Existing lower limb exoskeletons were classified according to their actuation modes. The characteristics of each type of exoskeleton were summarized. Regarding the control strategies, a hierarchical structure was used to review the state of the art within the scope of the thesis. Moreover, three main classes of physiological assessment methods (i.e., metabolic cost, gait biomechanics and muscle activities) were discussed, and the corresponding effectivenesses of some existing lower limb exoskeletons were presented as well. Finally, our research interest and scope were reiterated in light of the review of the literature.

3 Joint-level Tracking Control Strategy

3.1 Introduction

REFERENCE tracking control contributes a fundamental function of lower limb exoskeletons. For rehabilitation purposes, patients are usually assisted by exoskeletons in performing movements following the prescriptions of physical therapists (e.g., joint flexion/extension movements) to recover their motor abilities. From the perspective of power assistance, reference tracking control strategies also enable the wearer to achieve predesigned or intention-based daily living activities with the assistance of lower limb exoskeletons. Accurate tracking performance is crucial to guarantee the efficiency of the rehabilitation/training program as well as the accomplishment of the wearer's desired activities. Because lower limb exoskeletons operate in close physical interaction with the wearer and the environment, the development of control methods faces two types of problem: modeling uncertainties and external disturbances. The modeling of human-exoskeleton systems is subject to errors in the estimation of human kinetic/kinematic parameters, which may lead to inaccurate models. Additionally, the tracking performance may be affected by external disturbances such as the contact forces from the environment and the interaction torques delivered by the wearer. Note that the human joint torque can play the role of an assistive torque, or could be a resistive torque. From the viewpoint of the reference tracking controller, the human joint torque is considered as a bounded and time varying disturbance. Therefore, an important research trend of the reference tracking control of lower limb exoskeletons is to develop advanced controllers that are more robust with respect to system uncertainties and external disturbances [90,91].

This chapter presents a joint-level reference tracking control approach to assist in the wearer's knee-joint flexion/extension movements using the EICOSI exoskeleton. The proposed control approach is able to efficiently reduce the influence of the system modeling uncertainties and disturbances. Leading up to the controller design, a model integrating the human shank-foot and the EICOSI exoskeleton is presented, and a nonlinear disturbance observer (NDO) is introduced for disturbance estimation. Subsequently, we propose an NDO-based sliding mode

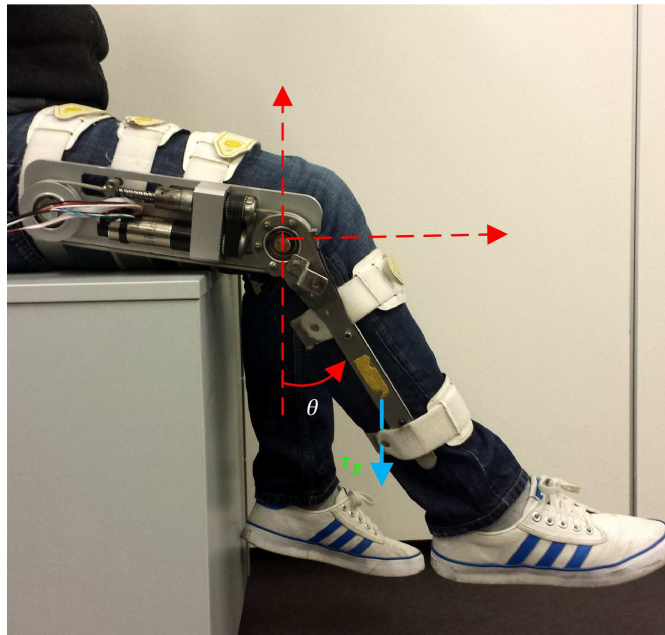


Figure 3.1 – A subject wearing the 1-DOF active EICOSI in the sitting position.

control (SMC). On this basis, we furthermore propose an NDO-based terminal sliding mode control (TSMC) strategy. By comparison with the basic SMC, the NDO-based SMC/TSMC can enhance the tracking performance, extend the control bandwidth and be more robust with respect to modeling uncertainties and external disturbances. Moreover, the proposed NDO-based TSMC can guarantee that the tracking error converges to zero in finite time and thereby improve the overall robustness. The stabilities of the NDO-based SMC and NDO-based TSMC are theoretically proven, and the advantage of the NDO-based TSMC with respect to reducing the convergence time is analyzed. Finally, experiments were conducted on different subjects using three control methods (basic SMC, NDO-based SMC and NDO-based TSMC) to show the advantages of the NDO-based TSMC in terms of tracking precision, required time for eliminating disturbances and robustness with respect to external disturbances.

3.2 System Modeling

3.2.1 Human-Exoskeleton System

A subject wearing the EICOSI exoskeleton with the shank freely moving around the knee joint is illustrated in Figure 3.1. This system is designed to carry out the flexion-extension movement of human knee joint in sitting position. The movements of the exoskeleton and the wearer's shank are considered to be synchronous and simultaneous (i.e., the human limb and the exoskeleton are rigidly coupled). According to the Lagrange formulation, the dynamic

model of the human shank-foot-exoskeleton can be written as follows:

$$J\ddot{\theta} + \tau_g \sin \theta + \text{Asgn}(\dot{\theta}) + B\dot{\theta} + K_j(\theta - \theta_{rp}) = \tau_e + \tau_{h,k}. \quad (3.1)$$

In the dynamic model, the knee joint angle, θ , is set to zero when the shank of the exoskeleton stays in the vertical direction. Consider the fact that a high ratio transmission is used in the EICOSI exoskeleton, the solid friction, $\text{Asgn}(\dot{\theta})$, is taken into account in the dynamic model. The dynamic system is actuated by both the exoskeleton and the wearer during flexion/extension movements.

3.2.2 Parametric Identification

The parameters of the dynamic model (3.1) that are needed be identified include A , B , J , K_j and τ_g . J is composed of the inertias of the human shank-foot and exoskeleton shank, while τ_g represents the resultant gravitational torque of the human shank-foot and the exoskeleton shank. The human shank-foot's inertia, J_h , and gravitational torque, $\tau_{g,h}$, can be estimated based on the weight and height of wearers using the method presented in [104], while the inertia J_e and gravitational torque $\tau_{g,e}$ of the exoskeleton shank have been identified in our previous study based on a model-based identification method as well as the least square optimization [105].

As it regards the remaining parameters, they were identified by using the passive pendulum test [106]. During the identification process, the wearer was asked to not deliver any muscular effort, i.e., $\tau_{h,k} = 0$. This is monitored by a null electromyographical activity of the thigh muscles spanning the knee joint. Then, the equation (3.1) can be rewritten as follows:

$$\tau_g \sin \theta + J\ddot{\theta} = -\text{Asgn}(\dot{\theta}) - B\dot{\theta} - K_j(\theta - \theta_{rp}). \quad (3.2)$$

The knee joint angle is measured by means of an incremental encoder; the angular velocity and acceleration are derived numerically. Therefore, only the parameters A , B and K_j need to be identified in equation (3.2). These parameters are identified using a nonlinear least square optimization applied to equation 3.2 [107].

3.3 Control Algorithms

In a human-in-the-loop robotic control system, the human-robot interaction force/torque constitutes an additional input to the actuator control one. This human interaction should be carefully taken into account as it makes the control of the overall system much more difficult. If the human effect could be considered as an external disturbance, while the sliding mode control might be an effective solution due to its robustness with respect to uncertainties and disturbances. Note that a conventional sliding mode control often has to face the trade-off between the control bandwidth and tracking precision due to the well-known

chattering effect. Some recent studies indicate that disturbance observer based sliding mode control strategies have better control performances than the conventional ones [108, 109]. The disturbance observer based sliding mode control can improve the control bandwidth and tracking precision effectively, and reduce, at the same time, the chattering effect. Therefore, we first develop a nonlinear disturbance observer.

3.3.1 Nonlinear Disturbance Observer

Define the state variable $\mathbf{x} = [x_1, x_2]^T$ with $x_1 = \theta$ and $x_2 = \dot{\theta}$. Therefore, the dynamic model (3.1) can be rewritten in the following vector form:

$$\dot{\mathbf{x}} = f_1(\mathbf{x}) + f_2(\mathbf{x})(\tau_e + d), \quad (3.3)$$

with

$$f_1(\mathbf{x}) = \begin{bmatrix} x_2 \\ \frac{1}{j}(-\tau_g \sin x_1 - A \operatorname{sgn}(x_2) - Bx_2 - K_j(x_1 - \theta_{rp})) \end{bmatrix},$$

$$f_2(\mathbf{x}) = \begin{bmatrix} 0 \\ \frac{1}{j} \end{bmatrix},$$

$$d = \tau_{h,k} + \tau_{d,ex},$$

where d denotes the lumped disturbance which includes the human input torque $\tau_{h,k}$ and the external disturbance $\tau_{d,ex}$. Note that modeling uncertainties and the external torques that act on the exoskeleton (except for the human torque) can be both considered as the external disturbances.

Let \hat{d} be the estimation of the disturbance d . A nonlinear disturbance observer is designed as follows:

$$\begin{cases} \dot{\hat{d}} = z + p(\mathbf{x}) \\ \dot{z} = L[-f_1(\mathbf{x}) - f_2(\mathbf{x})\tau_e - f_2(\mathbf{x})(z + p(\mathbf{x}))], \end{cases} \quad (3.4)$$

where $p(\mathbf{x})$ is chosen as $p(\mathbf{x}) = k_1 x_1 + k_2 x_2$, while k_1 and k_2 are two positive constants [92]. z is an auxiliary variable that is used to avoid the measurement of joint angular acceleration ($\ddot{\theta}$). L satisfies:

$$L = \frac{\partial p(\mathbf{x})}{\partial \mathbf{x}} = [k_1 \ k_2]. \quad (3.5)$$

From (3.3)-(3.5), it follows that:

$$\dot{\hat{d}} = Lf_2(\mathbf{x})(d - \hat{d}). \quad (3.6)$$

Let's define $\tilde{d} = d - \hat{d}$. Normally, there is no prior information about the derivative of distur-

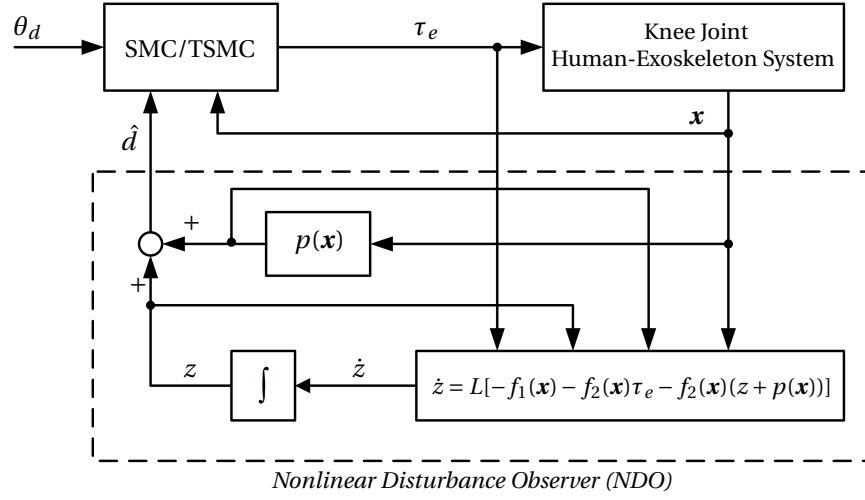


Figure 3.2 – Nonlinear disturbance observer based SMC/TSMC control diagram for the knee-joint human exoskeleton system.

bance d . When the disturbance varies slowly relative to the observer dynamics, it is reasonable to suppose that $\dot{d} = 0$. Then, from (3.6), it follows that:

$$\dot{\hat{d}} = -L f_2(\mathbf{x}) \tilde{d} = -\frac{k_2}{J} \tilde{d}. \quad (3.7)$$

Then, the residual of disturbance estimation approaches zero since k_2 is a positive constant.

3.3.2 NDO-based Sliding Mode Control

To design the NDO-based SMC, first we consider the following sliding surface:

$$s = c_1 e + \dot{e} \quad \text{with} \quad e = x_1 - \theta_d \quad (3.8)$$

where θ_d is the desired trajectory.

The NDO-based SMC controller is then given by:

$$\tau_e = -J c_1 \dot{e} + \tau_g \sin x_1 + A \text{sgn}(x_2) + B x_2 + K_j (x_1 - \theta_{rp}) - \hat{d} + J \ddot{\theta}_d - \lambda s - \sigma \text{sgn}(s), \quad (3.9)$$

where $c_1, \lambda > 0, \sigma > |\tilde{d}_{max}|$. $|\tilde{d}_{max}|$ is used to denote the upper bound of the disturbance estimation error. The whole closed-loop NDO-based SMC control system is depicted on Figure 3.2.

The stability of the knee-joint shank-foot-exoskeleton system with NDO-based SMC is addressed in the following proposition.

Proposition 3.1. Consider the knee-joint shank-foot-exoskeleton system (3.1) with a NDO-

based SMC controller (3.9). Assume that the disturbance d varies slowly relative to the observer dynamics. Then, the trajectory of the system (3.1) can be driven towards the sliding surface (3.8).

Proof. Choose the Lyapunov function V as:

$$V = \frac{1}{2}s^2 + \frac{1}{2}\tilde{d}^2. \quad (3.10)$$

By differentiating (3.10), we obtain:

$$\begin{aligned} \dot{V} &= s\dot{s} + \tilde{d}\dot{\tilde{d}} \\ &= s\frac{1}{J}(-\tau_g \sin x_1 - A\text{sgn}(x_2) - Bx_2 - K_j e + \tau_e + d) + c_1 \dot{e} - s\ddot{\theta}_d - \tilde{d}Lf_2\dot{\tilde{d}}. \end{aligned} \quad (3.11)$$

By substituting (3.9) into the derivative of the Lyapunov function, we obtain:

$$\begin{aligned} \dot{V} &= s\left(\frac{\tilde{d} - \lambda s - \sigma \text{sgn}(s)}{J}\right) - Lf_2\tilde{d}^2 \\ &= \frac{1}{J}s(\tilde{d} - \sigma \text{sgn}(s)) - \frac{1}{J}\lambda s^2 - Lf_2\tilde{d}^2 \leq 0. \end{aligned} \quad (3.12)$$

Therefore, the Lyapunov function is decreasing and the system is stable. This completes the proof. \square

3.3.3 NDO-based Terminal Sliding Model Control (TSMC)

An NDO-based terminal sliding mode control method is further proposed to enhance performance of the control system. Indeed, by comparison with the basic SMC, the TSMC algorithm guarantees the tracking error convergence to zero in finite time [110]. This means that the tracking error converges to zero in finite time, even if there is an initial drift between the reference trajectory and the real position of the shank-foot-exoskeleton system. Additionally, a robust TSMC method is proposed to reduce the required time for eliminating the influence of relatively large external disturbance once the system reaches the sliding surface. Finally, the modeling uncertainties are taken into account in the proposed NDO-based TSMC method as well. The sliding surface, in the case of the NDO-based TSMC, is defined as follows:

$$s = c_1 e + \dot{e} - w \quad \text{with} \quad w = c_1 v + \dot{v}, \quad (3.13)$$

where v is defined as a continuously differentiable function, and $v \in C[0, \infty]$, $v, \dot{v} \in L^\infty$, and $\forall t > T, v = \dot{v} = 0$, $T > 0$; the initial values of v and \dot{v} are chosen as follows: $v(0) = e(0)$, $\dot{v}(0) = \dot{e}(0)$. In this study, a cubic spline function is used to express the function v [110]:

$$v = \begin{cases} a_0 + a_1 t + a_2 t^2 + a_3 t^3 & 0 \leq t \leq T \\ 0 & t > T \end{cases}, \quad (3.14)$$

where the coefficients of the cubic spline are defined as: $a_0 = e(t = 0)$, $a_1 = \dot{e}(t = 0)$, $a_2 = 3(e(t = T) - e(t = 0))/T^2 - 2\dot{e}(t = 0)/T - \dot{e}(t = T)/T$, $a_3 = -2(e(t = T) - e(t = 0))/T^3 + (\dot{e}(t = 0)/T + \dot{e}(t = T))/T^2$.

For convenience, f_m and f_g are used to denote the nonlinear dynamics and control gain of the shank-foot-exoskeleton system separately. According to equation(3.3), f_m and f_g are given as follows:

$$\begin{cases} f_m = f_1(2, 1) \\ f_g = f_2(2, 1). \end{cases} \quad (3.15)$$

Therefore, the dynamic equation (3.1) can be rewritten as follows:

$$\dot{x}_2 = f_m + f_g \cdot (\tau_e + d). \quad (3.16)$$

Here, NDO-based TSMC is designed as follows:

$$\tau_e = \hat{f}_g^{-1} [\ddot{\theta}_d - \hat{f}_m - c_1 \dot{e} + c_1 \dot{v} + \ddot{v} - \kappa \text{sgn}(s) - \lambda s] - \hat{d}, \quad (3.17)$$

where, \hat{f}_g and \hat{f}_m represent the estimation of f_g and f_m respectively. λs ($\lambda > 0$) represents the factor used to reduce the required time for eliminating the external disturbance. By considering the parameter uncertainty of the identified system, κ is defined as follows:

$$\kappa = (1 - D_{max})^{-1} (F_{max} + D_{max} |\ddot{\theta}_d - \hat{f}_m - c_1 \dot{e} + c_1 \dot{v} + \ddot{v}| + T + (1 + D_m) \hat{f}_g \sigma), \quad (3.18)$$

where D_{max} and F_{max} are two positive constants that satisfy the conditions: $1 > D_{max} > |1 - f_g / \hat{f}_g|$ and $F_{max} > |f_m - \hat{f}_m|$, $T > 0$. The whole closed-loop NDO-based TSMC control diagram of the shank-foot-exoskeleton system is shown in Figure 3.2 as well. The following proposition addresses the analysis of stability of shank-foot-exoskeleton system with the NDO-based TSMC.

Proposition 3.2. Consider the knee-joint shank-foot-exoskeleton system (3.1) with a NDO-based TSMC controller (3.17). Assume that the disturbance d varies slowly relative to the observer dynamics. Then, the trajectory of the system (3.1) can be driven towards the sliding surface (3.13).

Proof. Choose the Lyapunov function V as:

$$V = \frac{1}{2} s^2 + \frac{1}{2} \tilde{d}^2. \quad (3.19)$$

By differentiating (3.19) along the equation (3.7) and (3.13), we obtain:

$$\begin{aligned} \dot{V} &= s \dot{s} + \tilde{d} \dot{\tilde{d}} \\ &= s [c_1 \dot{e} + \ddot{e} - c_1 \dot{v} - \ddot{v}] - L f_2 \tilde{d}^2, \end{aligned} \quad (3.20)$$

where $\ddot{e} = \dot{x}_2 - \ddot{\theta}_d$. From (3.16) and (3.17), (3.20) can be expressed as:

$$\begin{aligned}\dot{V} &= s[f_m + f_g \cdot (\tau_e + d) - \ddot{\theta}_d + c_1 \dot{e} - \ddot{v} - c_1 \dot{v}] + (-Lf_2 \tilde{d}^2) \\ &= s[f_m + f_g [(\hat{f}_g^{-1} [\ddot{\theta}_d - \hat{f}_m - c_1 \dot{e} + c_1 \dot{v} + \ddot{v} - \kappa \text{sgn}(s) - \lambda s] - \hat{d}) + d] \\ &\quad - \ddot{\theta}_d + c_1 \dot{e} - \ddot{v} - c_1 \dot{v}] - Lf_2 \tilde{d}^2.\end{aligned}\quad (3.21)$$

Define $\Delta = (f_g / \hat{f}_g - 1)$, then, (3.21) can be rewritten as follows:

$$\begin{aligned}\dot{V} &= s[f_m + (1 + \Delta) \hat{f}_g [\hat{f}_g^{-1} [\ddot{\theta}_d - \hat{f}_m - c_1 \dot{e} + c_1 \dot{v} + \ddot{v} - \kappa \text{sgn}(s) - \lambda s] - \hat{d} + d] \\ &\quad - \ddot{\theta}_d + c_1 \dot{e} - \ddot{v} - c_1 \dot{v}] - Lf_2 \tilde{d}^2 \\ &= s[f_m - \hat{f}_m + \Delta (\ddot{\theta}_d - \hat{f}_m - c_1 \dot{e} + c_1 \dot{v} + \ddot{v}) - (1 + \Delta) \kappa \text{sgn}(s) + (1 + \Delta) \hat{f}_g \tilde{d}] \\ &\quad - (1 + \Delta) \lambda s^2 - Lf_2 \tilde{d}^2.\end{aligned}\quad (3.22)$$

Due to $1 > D_{max} > |1 - f_g / \hat{f}_g|$ and $F_{max} > |f_m - \hat{f}_m|$, $T > 0$, (3.22) satisfies

$$\begin{aligned}\dot{V} &\leq s[(F_{max} + D_{max} |\ddot{\theta}_d - \hat{f}_m - c_1 \dot{e} + c_1 \dot{v} + \ddot{v}| + (1 + D_{max}) \hat{f}_g \tilde{d}) \text{sgn}(s) \\ &\quad - (1 - D_{max}) \kappa \text{sgn}(s)] - (1 - D_{max}) \lambda s^2 - Lf_2 \tilde{d}^2.\end{aligned}\quad (3.23)$$

From (3.18), the derivative of Lyapunov function can be further rewritten as follows:

$$\dot{V} \leq -T|s| - (1 - D_{max}) \lambda s^2 - Lf_2 \tilde{d}^2 \leq 0. \quad (3.24)$$

The Lyapunov function of the NDO-based TSMC control system is decreasing. Therefore, the stability of the closed-loop system is proved, and the tracking error e converges to zero in finite time T . \square

Based on stability proof mentioned above, we furthermore analyze the convergence time of the proposed NDO-based TSMC. According to (3.7), (3.20) and (3.24), it can be observed that:

$$s\dot{s} \leq -T|s| - (1 - D_{max}) \lambda s^2 \leq -T|s|.$$

Due to $s(t) \equiv 0$ and $e(t) \equiv v(t)$, $e(t)$ can converge to zero in finite time T , i.e., $e(t) = 0, \forall t \geq T$. Furthermore, it can be known:

$$s\dot{s} = \frac{1}{2} \frac{d}{dt} s^2 \leq -T|s| - (1 - D_{max}) \lambda s^2. \quad (3.25)$$

Assume for instance that $s(t = T_s) > 0$, (T_s is the starting time of a given point, which does not belongs to the sliding surface). T_r is defined as the time when the system reaches onto the sliding surface. Integrating the equation (3.25) between $t = T_s$ and $t = T_r$ leads to

$$0 - s(t = T_s) = s(t = T_r) - s(t = T_s) \leq -T(T_r - T_s) - (1 - D_{max}) \lambda \int_{T_s}^{T_r} s dt. \quad (3.26)$$

which implies that:

$$T_r - T_s \leq \frac{s(t = T_s) - (1 - D_{max})\lambda \int_{T_s}^{T_r} s dt}{T}. \quad (3.27)$$

If $s(t = T_s) < 0$, a similar result can be obtained, Hence, the equation (3.27) can be rewritten as follows:

$$T_r - T_s \leq \frac{|s(t = T_s)| - (1 - D_{max})\lambda \int_{T_s}^{T_r} |s| dt}{T}. \quad (3.28)$$

Therefore, if $T_s = 0$, we observe that $|s(t = 0)|$ will be equal to zero in the NDO-based TSMC system. This means that the control system lies always on the sliding surface. Hence, the tracking error can converge to zero in finite time (T) [110]. On the other hand, if the external disturbance occurs after the time T (i.e., $T_s > T$), we observe that $w = 0, \forall t > T$. In this case, the w has no effect on reducing the disturbance. However, the convergence time ($T_r - T_s$) can also be reduced by the factor, $(1 - D_{max})\lambda \int_{T_s}^{T_r} |s| dt$, which is introduced through λs . Overall, it is clear that NDO-based TSMC can efficiently reduce the required time for eliminating external disturbances.

3.4 Experimental Evaluation

The experiments were conducted with the participation of three healthy subjects and a plastic mannequin (see Figure 3.3). The three subjects's basic information such as sex, age, weight and height are listed in Table 3.1. Subject 1 is one of the researchers involved in this study, while the other subjects are totally naive to the experimentation. During the experiments, the three aforementioned control methods are used (i.e., Basic SMC, NDO-based SMC and NDO-based TSMC). The parameters of the system (3.1) are identified using the method presented in section 3.2.2. Table 3.2 shows the identified parameters of Subject 1 and the EICOSI exoskeleton. The parameters of the three controllers used in the experiments are also chosen based on the experimental performance conducted by Subject 1. The parameters of three controllers are tuned by trial and error, and are given as follows:

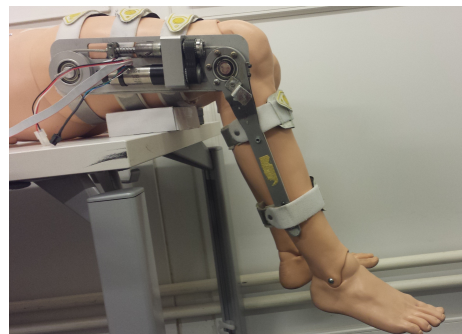


Figure 3.3 – A mannequin wearing the EICOSI exoskeleton in the sitting position.

Subject	Sex	Age(yr)	Weight(kg)	Height(cm)
S_1	M	27	66	170
S_2	F	24	60	172
S_3	M	23	72	173

Table 3.1 – Subjects' information

Parameters	Values
$J(J_e + J_h)$	0.2639(0.0117 + 0.2522) $Kg \cdot m^2$
$\tau_g(\tau_{g,e} + \tau_{g,h})$	8.5724(0.2424 + 8.33) Nm
A	4.4289 Nm
B	0.5950 $Nm \cdot s \cdot rad^{-1}$
K_j	0.3382 $Nm \cdot rad^{-1}$

Table 3.2 – Identified system parameters

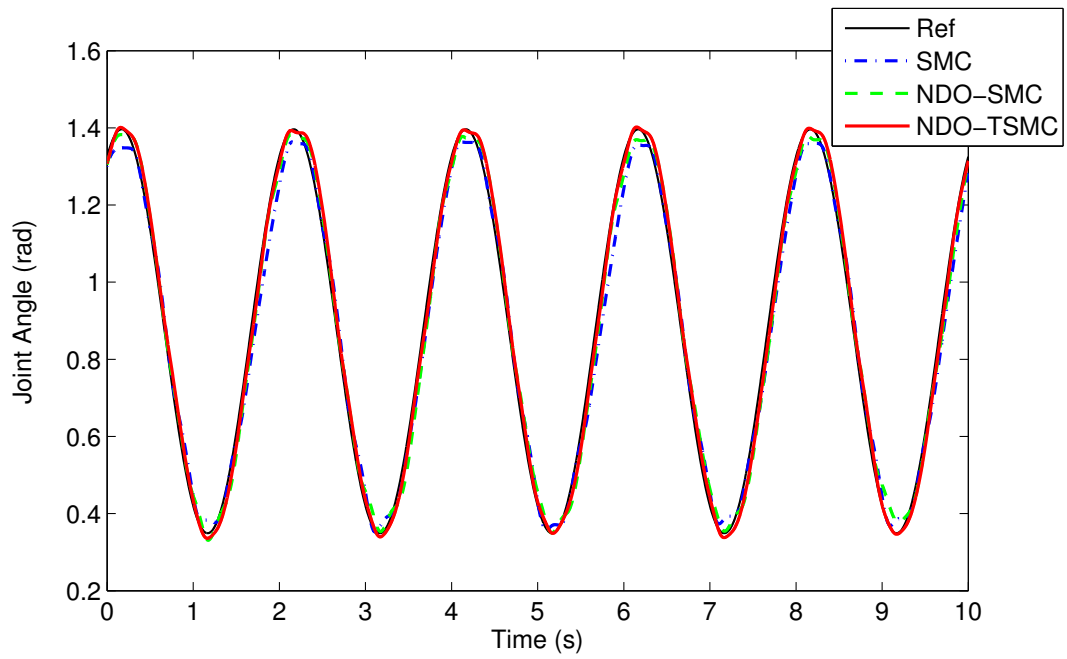
- Basic SMC: $c_1 = 5$, $k_1 = 0$, $k_2 = 0$, $\lambda = 0$, and $\sigma = 15$;
- NDO-based SMC: $c_1 = 5$, $k_1 = 1.5$, $k_2 = 0.5$, $\lambda = 0$, and $\sigma = 15$;
- NDO-based TSMC: $c_1 = 5$, $k_1 = 1.5$, $k_2 = 0.5$, $\lambda = 5$, $\sigma = 7.5$, $D_m = 0.1$, $F_m = 1$, and $T = 0.5$.

Note that the basic SMC is obtained based on the controller (3.9) by setting the parameters k_1 , k_2 and λ to zero. To compare the three controllers' robustness with respect to modeling uncertainties, the same controller parameters are also used in the experiments conducted by Subject 2, Subject 3 and the mannequin.

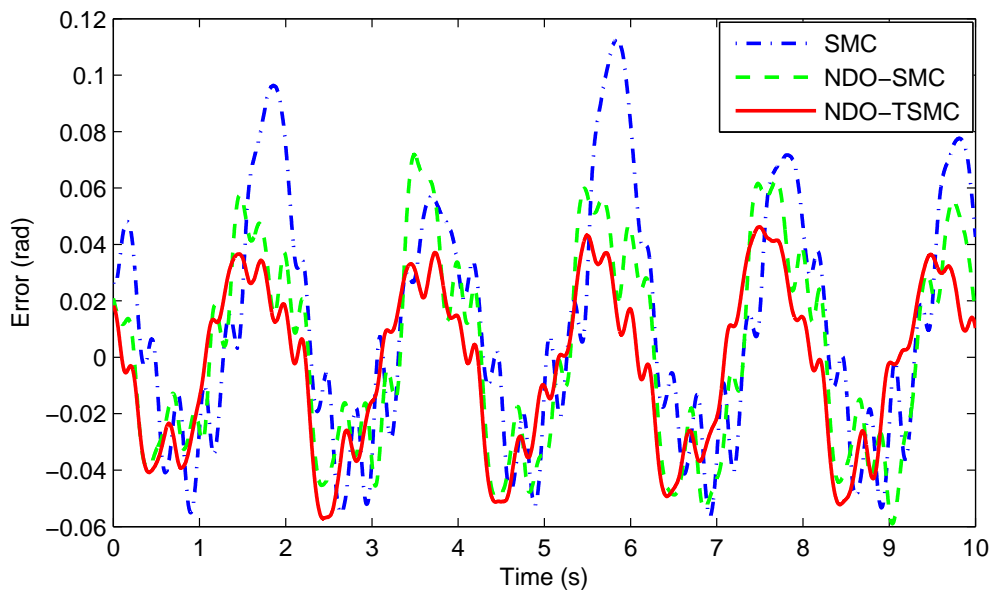
To evaluate the performance of the control methods proposed in this study, three groups of experiments were carried out to compare the tracking precision, the required time for eliminating the disturbance and robustness with respect to modeling uncertainties.

3.4.1 Comparison of Tracking Precision

In this experiment, three different control algorithms, i.e., Basic SMC, NDO-based SMC and NDO-based TSMC, were used to control the shank-foot-exoskeleton system to track a given sinusoidal trajectory with a frequency of 0.5 Hz. Subject 1 participated in this experiment. He sat on a table while wearing the EICOSI exoskeleton (see Figure 3.1), and was asked not to deliver any knee joint torque during the experiment.



(a)



(b)

Figure 3.4 – Comparison experiments of tracking precision using the three control methods. (a) the reference knee joint angles and the tracking results of three control algorithms. (b) the tracking errors of the three control algorithms: MAE = {SMC, 0.03576 ± 0.0259 rad}, {NDO-based SMC, 0.03197 ± 0.01635 rad}, {NDO-based TSMC, 0.02486 ± 0.01492 rad}.

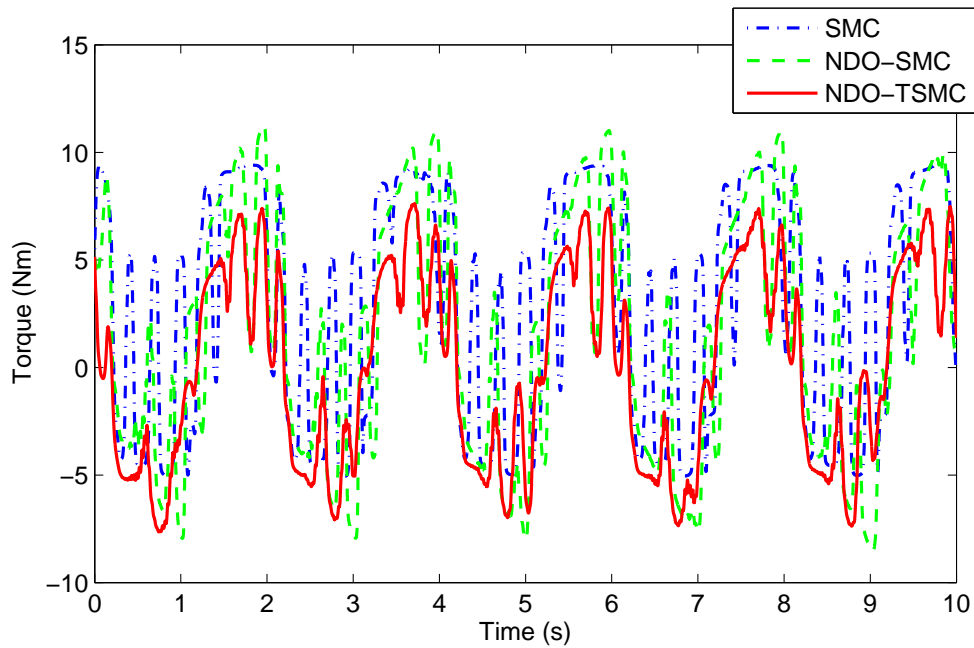


Figure 3.5 – Control torques generated with the three control methods.

Figure 3.4a shows the real and reference knee joint angles with the three control algorithms, and Figure 3.4b shows the tracking errors. The tracking performance of the three control algorithms are compared using the Mean Absolute Error (MAE). It can be observed that compared to the basic SMC, the NDO-based TSMC is able to effectively reduce the tracking error (for the NDO-based TSMC, $MAE = 0.02486 \pm 0.01492$ rad; for the basic SMC, $MAE = 0.03576 \pm 0.0259$ rad). At the same time, the chattering of the control torque of NDO-based TSMC is the lowest among these three approaches (see Figure 3.5). Note that the comfort of the user is often associated with the chattering effect that is noticed at the control torques; the lower the frequency and amplitude of the chattering, the higher the comfort of the wearer. The tracking error and chattering of the control torque slightly decrease when using NDO-based SMC, compared to the use of basic SMC. However, the peak error values when using the NDO-based SMC control can be maintained into a relatively small range (see Figure 3.4b), due to the use of the NDO.

3.4.2 Comparison of the Required Time to Eliminate Disturbance

As mentioned above, two important advantages of the proposed NDO-based TSMC approach is to guarantee that the tracking error converge to zero in finite time, and to quickly eliminate the external disturbance. To verify these properties, two experiments were designed correspondingly. In the first one, an initial tracking error was introduced at the beginning of the experiment, while in the other one, an external disturbance was added to the shank-foot-exoskeleton system for a limited time after the system trajectory has reached the surface.

Similarly, three control algorithms (basic SMC, NDO-based SMC and NDO-based TSMC) were used to track a reference sinusoidal trajectory with a frequency of 0.5 Hz during both experiments. The convergence time to the sliding surface was calculated and compared. To keep the same experimental conditions and avoid the influence caused by the human, a plastic mannequin was used to guarantee the accuracy of comparison.

Figure 3.6a and Figure 3.6b respectively show the knee joint angles and tracking errors corresponding to the first experiment. Since the ideal zero-error tracking performance is difficult to be obtained in practice, here, a small error range (i.e., $\pm 0.15 rad$) is set to indicate the satisfied tracking performance (see Figure 3.6b). One can observe that the convergence time of the NDO-based TSMC method is smaller than the basic SMC. The NDO-based SMC does not show an advantage on the convergence time, compared to the basic SMC, as shown in Figure 3.6a. This is due to the fact that the NDO increases the control torque quickly (see Figure 3.8a) to track the desired trajectory at the beginning, and this sudden increase in the torque impacts negatively the follow-up convergence. However, this problem is avoided when using the NDO-based TSMC methods. The NDO-based TSMC controller is able to deal with sudden changes of the position at the beginning due to the presence of the factor ν . In the second experiment, a given external disturbance is added to the system (between $t=4s$ and $t=5.2s$), as shown in Figure 3.7a and Figure 3.7b. The comparative results show that the NDO-based TSMC approach can significantly reduce the required time for eliminating the external disturbance effects. Moreover, one can observe that the basic SMC cannot effectively compensate the external disturbances (see Figure 3.7a and Figure 3.7b). Moreover, the control torques corresponding to both experiments are also shown in Figure 3.8a and Figure 3.8b.

3.4.3 Comparison of the Robustness Regarding Modeling Uncertainties

To verify the robustness with respect to modeling uncertainties of the proposed control methods, two other subjects (i.e., Subject 2 and Subject 3) and a plastic mannequin with 1 kg load on its foot were chosen to conduct the same experiment as mentioned in Section 3.4.1. The identified parameters of the shank-foot model for Subject 1 and the parameters of three control algorithms listed at the beginning of Section 3.4 were still used in this experiment, although the related parameters of Subject 2, Subject 3 and the mannequin are obviously different from those of the Subject 1. Three groups of experiments were conducted by each subject or mannequin, and each group lasted 15 seconds. The experimental results (tracking errors) are shown in Table 3.3. According to the tracking errors, one can notice that the MAEs when using the NDO-based SMC/TSMC are always smaller than those when using the basic SMC. Additionally, the robustness of the NDO-based TSMC is the best among those three control approaches. The tracking errors of the NDO-based TSMC did not increase significantly with changes of the system parameters, while there are relatively significant changes in errors when using the other two approaches, particularly the basic SMC.

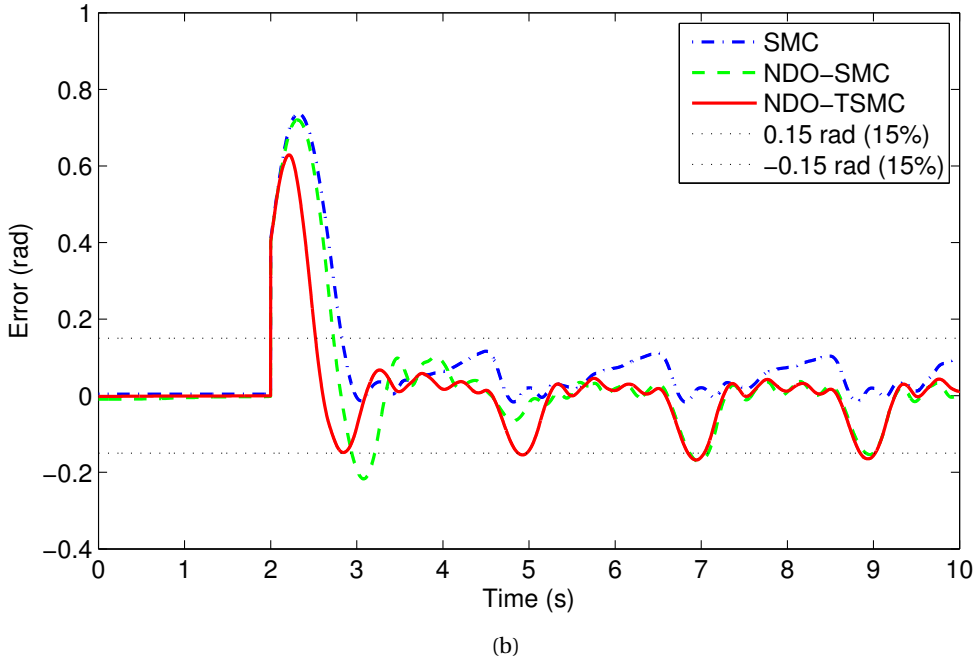
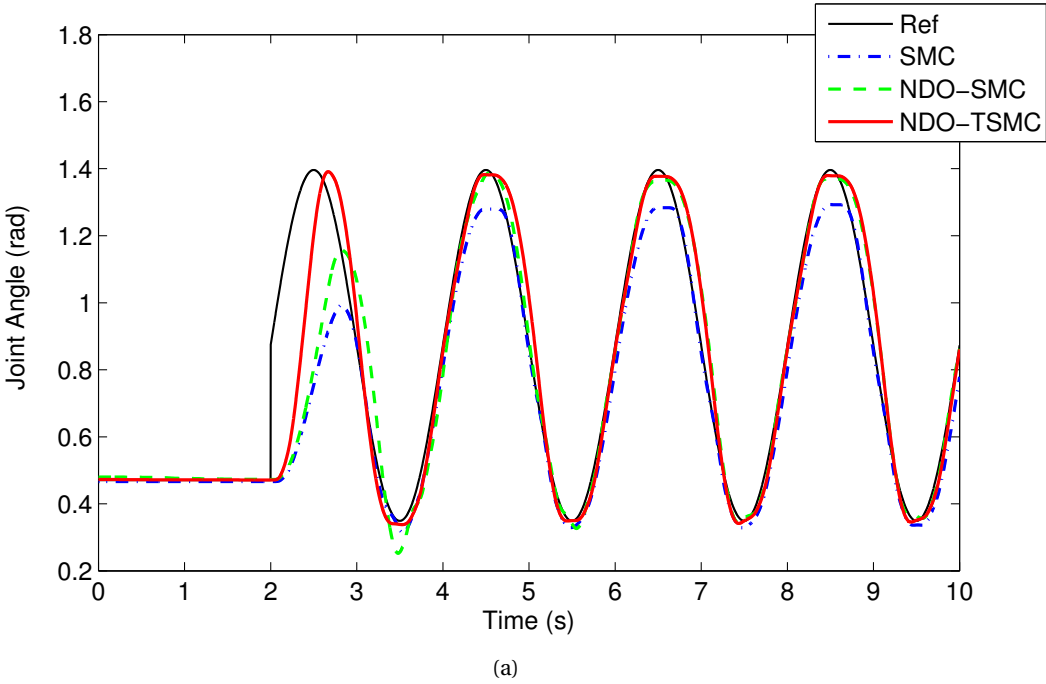
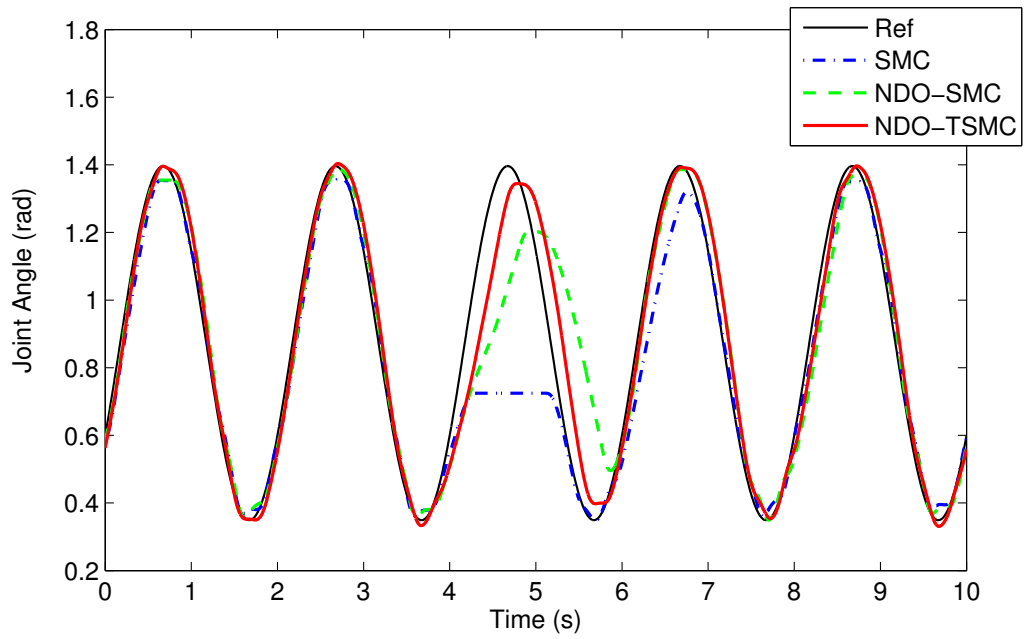
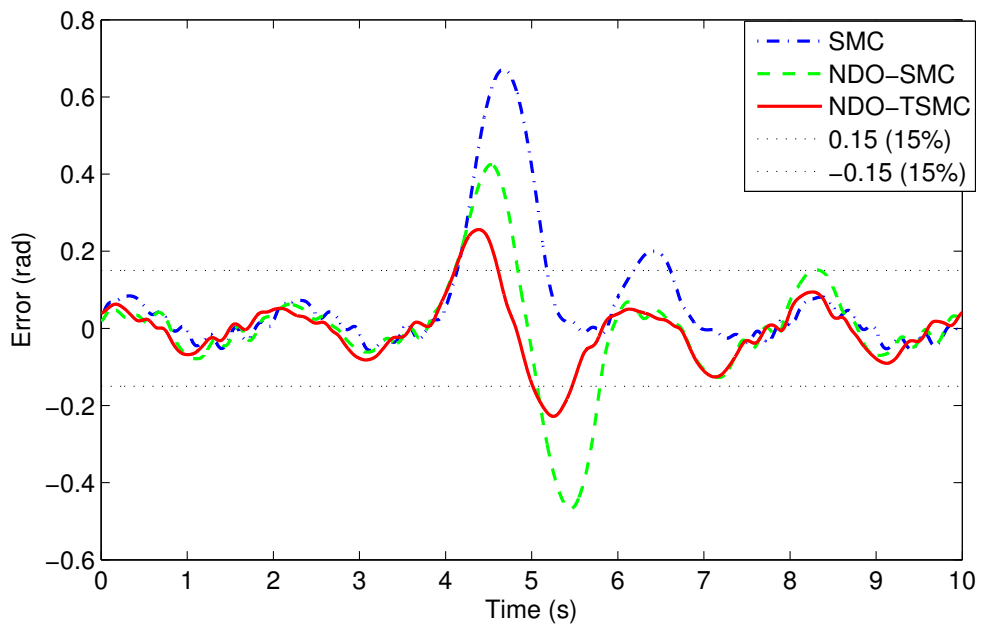


Figure 3.6 – Comparison of the required times for eliminating initial errors (conducted by the mannequin) when using basic SMC, NDO-based SMC and NDO-based TSMC respectively. (a) the desired trajectory and the tracking trajectories. (b) the tracking errors.

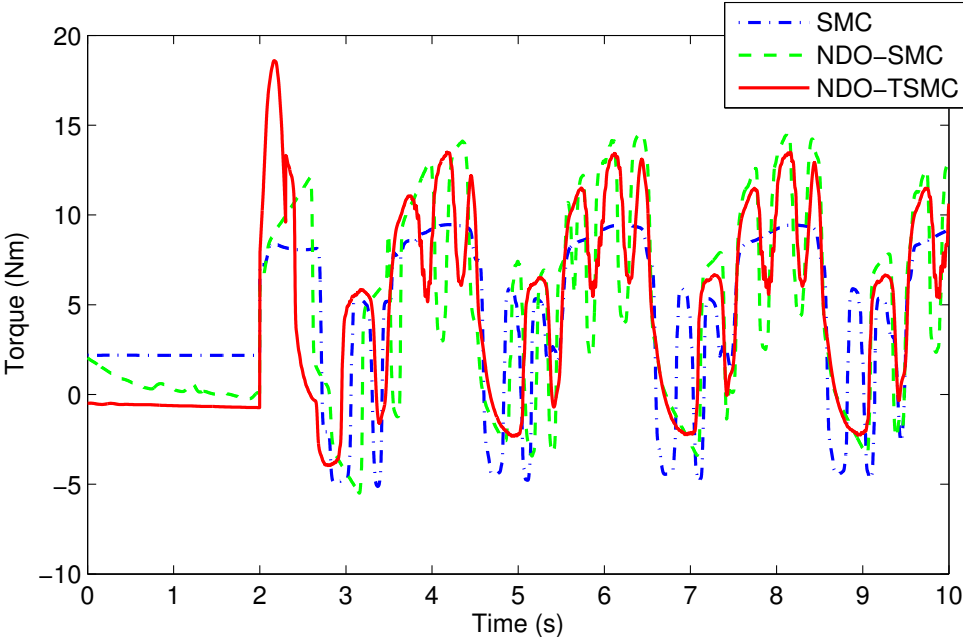


(a)

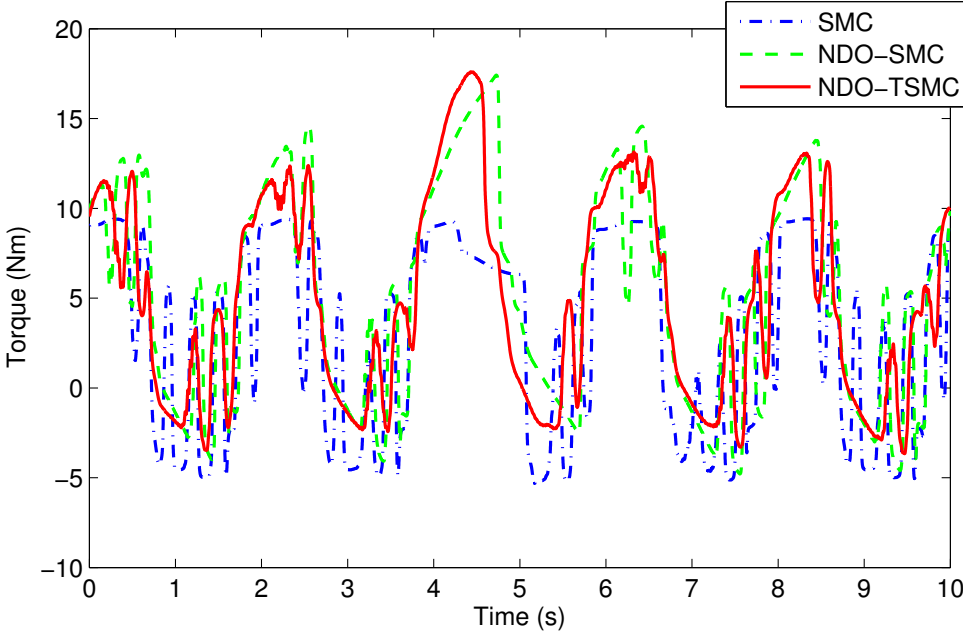


(b)

Figure 3.7 – Comparison of the required times for eliminating external disturbance (conducted by the mannequin) when using basic SMC, NDO-based SMC and NDO-based TSMC respectively. (a) the desired trajectory and the tracking trajectories. (b) the tracking errors.



(a) Comparison of the required times for eliminating initial errors



(b) Comparison of the required times for eliminating external disturbances

Figure 3.8 – The control torques of the basic SMC, NDO-based SMC and NDO-based TSMC.

Subjects	SMC	NDO-based SMC	NDO-based TSMC
Subject 1	0.0358 ± 0.0259	0.0320 ± 0.0164	0.0249 ± 0.0149
Subject 2	0.2450 ± 0.2028	0.0653 ± 0.0479	0.0532 ± 0.0392
Subject 3	0.3647 ± 0.1221	0.0525 ± 0.0299	0.0450 ± 0.0268
Mannequin	0.0584 ± 0.0421	0.0401 ± 0.0451	0.0328 ± 0.0328

Table 3.3 – The mean absolute tracking errors (unit: rad)

3.5 Conclusion

The present chapter addressed the development of low-level control strategies for a lower limb exoskeleton for assisting the wearer in performing knee joint flexion/extension movements. A model of the human shank-foot combined with the EICOSI exoskeleton was developed and its parameters were identified using least squares optimization. Two control methods were proposed to control the shank-foot-exoskeleton along the desired trajectories: a basic sliding mode controller coupled to a disturbance observer as well as a robust terminal sliding mode control approach combined with a nonlinear disturbance observer. The human muscular torque was considered as an external disturbance of the system, so the NDO-based SMC and NDO-based TSMC were designed to estimate the human torque and enhance the performance of the shank-foot-exoskeleton system. The stability of the system is proven by means of a Lyapunov analysis. The experimental results confirmed the advantages of the NDO-based TSMC: improving the tracking precision and reducing the required time for eliminating the external disturbances. The robustness and stability of the NDO-based TSMC method were verified by experiments as well.

The current chapter does not address the misalignment problem between the exoskeleton and the wearer's leg that was considered in the literature, chiefly in exoskeletons with multiple degrees of freedom [28]. In this study, this problem has been considerably reduced by manually adjusting the exoskeleton to each wearer's morphology using adaptable straps. Special care has been taken during experiments to avoid reaching full knee joint flexion, which considerably reduces the joint misalignment.

Although the system model is built based on the sitting position, the control strategy proposed in this chapter is considered to be suitable for other daily living activities, for instance, walking. In these activities, the muscular effort can also be considered as an external disturbance similar to that of the sitting position. In this case, a rational reference trajectory provided by therapists can also be tracked by the wearer's lower limb with the assistance of the EICOSI, if the associated models are built based on these activities. Hence, the proposed control approach can be extended for different human exoskeleton models during various daily living activities, such as normal gait walk, sit-to-stand and stairs climbing.

Summary

In this chapter, a nonlinear disturbance observer based terminal sliding mode control approach of a knee-joint lower limb exoskeleton was presented. Compared to conventional control methods, the advantages of the proposed control approach are accurate tracking performance, fast convergence and strong robustness with respect to modeling uncertainties and disturbances. The corresponding performances of the proposed control methods were both theoretically analyzed and evaluated by experiments. Experimental results of two other methods (i.e., basic SMC and NDO-based SMC) were also presented and compared to the proposed control approach in terms of the tracking precision, convergence time and robustness.

4 Intention Based Single-task Assistive Control Strategy

4.1 Introduction

As stated in the General Introduction section, the goal of this part is to develop an intention based control strategy to assist the wearer in performing single-task daily living activities. Considering that the human joint kinematics and kinetics are significantly different with the changes in daily living activities, different assistive control approaches of lower limb exoskeletons are usually designed for specific activities. In this case, developing a general algorithm that can be easily used to assist in different activities is of great importance. This requires that minimum sensing measurements be used to estimate the human motion intention and the control strategy be available for assisting in various daily living activities. Although EMG signals can be used to estimate the human intention during lower limb activities, they suffer from some inherent drawbacks (e.g., complexity and sensitivity) in practice. Hence, we focus on designing a dynamic model based intention estimation method. Regarding the assistive control strategies of the human-in-the-loop systems, impedance control has been efficiently used during different daily living activities [56, 64, 111]. Moreover, recent studies have shown that the human motion control can also be considered to be an impedance control [56, 112].

In this chapter, we propose a generalized active impedance control (AIC) structure for lower limb exoskeletons, which is able to compensate the mechanical impedance of the human-exoskeleton system. The structure consists of three parts: a human joint torque observer, a sliding mode controller and the desired impedance model. The human joint torque (i.e., the human motion intention) is estimated using joint angle information instead of EMG signals or force/torque sensors. The proposed approach can be conveniently used for different lower limb exoskeletons and to assist in different human activities. To evaluate the performance of the proposed structure, two cases are studied. In the first case, a single-joint nonlinear active impedance control approach of the EICOSI exoskeleton is developed based on the proposed structure to assist in the knee joint flexion/extension movements. The performances of the proposed structure are theoretically analyzed in detail and experimentally evaluated. In

the second case, an extended multi-joint active impedance control is proposed to assist in sit-to-stand movements using the E-ROWA exoskeleton. Correspondingly, the stability and robustness to modeling uncertainties of the proposed multi-joint control approach are analyzed. Experiments were carried out to evaluate the effectiveness of the proposed approach.

In the following, the problems facing the joint flexion/extension and sit-to-stand movements are discussed. Subsequently, the control objective of each case is presented.

Case Study I: Knee Joint Flexion/Extension Movements

The mechanical rigidity of lower limb exoskeletons often imposes additional constraints and loads on the wearer that may alter natural human movements. For example, during walking, the swing phase adopts a pendular motion that reduces the metabolic cost [113]. Locomotion activities, supported by exoskeletons, are generally subject to mechanical artifacts of the robotic device, and these tend to considerably impact the natural pendulum oscillation movement of the lower limbs. Additionally, significant muscular strength is required if the robot interacting with the human limbs has a relatively high impedance. Indeed, reducing the impedance of the exoskeleton through an appropriate control strategy is beneficial in providing power assistance for the wearer [114, 115]. The human efforts can be further reduced if the original impedance of the human limbs is adjusted to a lower value. For instance, Ollinger *et al.* [64, 113, 116] proposed a torque-sensor-based method to compensate for human limb impedance such as damping and inertia, which leads to a significant increase in the agility of the wearer's knee joint movements.

The knee joint flexion/extension movement is considered a pendulum-based experimental scenario to demonstrate the ability of the control approach to promote self-oscillation. Therefore, the control strategy should guarantee the energy needed for the operation of a human-robot exoskeleton system to not only maintain the natural, intrinsic human limb oscillation dynamics but also to facilitate cyclic movements through compensation for inertia, friction and gravity. Whereas compensation for the solid and viscous friction of the exoskeleton is feasible, compensation for the system's inertia is quite challenging due to stability issues [117, 118]. Without appropriate compensation for the inertia, the walking speed will be highly impacted, and the required human effort will increase. Hence, the proposed controller should be sufficiently robust to compensate not only for friction and gravity (i.e., stiffness) but also for system inertia without affecting the stability of the system.

Case Study II: Sit-to-Stand Movements

Sit-to-stand (STS) movement constitutes a key movement of our daily living activities and is a prerequisite of the main daily movements, such as walking. Indeed, from a clinical point of view, standing up from a sitting position is a difficult task facing elderly and dependent people suffering from musculoskeletal system disorders. In [119], several main factors that impact the STS movement, or result in failed STS, were noted, such as balance control, coordination

impairment, and particularly, lower limb muscle weakness.

Recently, assistive exoskeletons have been designed and developed to provide functional motion assistance to elderly and disabled people when achieving daily activities, such as walking and STS movements [6]. The STS assistive strategies using a powered exoskeleton can be roughly divided into two main categories based on the wearer's conditions: exoskeletons that provide all required torques for the STS movement as well as those that complement the wearer's strength (i.e., where the wearer's effort is also taken into account). For the first class, the wearers are usually unable to deliver any lower limb efforts such as complete spinal cord injuries or can generate very limited lower limb muscular strength. In this case, reference-based tracking control strategies are generally adopted while the wearer's residual efforts are considered as external disturbances to the exoskeleton [50, 120]. Regarding the second class, the wearer is able to provide partial muscular efforts, while the exoskeleton complements the wearer's strength to complete a successful STS movement. Note that most elderly people who face the STS fall risk problem are under the situation of the second class [119]. In this section, we focus on the STS motion support using a powered exoskeleton for wearers with a partial loss of their lower limb muscular efforts.

To complement the wearer's muscular strength, the ability to estimate the human motion intention is a fundamental and essential point for active exoskeletons. The muscular strength varies with the individual, so it is also important to provide power assistance to the wearer according to their lower limb muscular strength. This is efficient to encourage the wearer to train and improve his/her own motor ability.

4.2 System Modeling

4.2.1 The Knee Joint Flexion/Extension Movement

To analyze the impedance characteristics of the human exoskeleton system, knee-joint flexion/extension movements of a wearer in a sitting position assisted by the EICOSI are studied. Note that the knee joint movements of the swinging leg during a given gait cycle have a pendulum oscillatory flexion/extension behavior that is close to the natural frequency [121]. Hence, the same experimental scenario as shown in Section 3 (see Figure 3.1) is used here. In this section, however, the wearer wearing the EICOSI is asked to actively swing the shank. We assume that the human limb and the exoskeleton are rigidly coupled. As aforementioned in Section 3.2.1, the dynamic model of the shank exoskeleton system is designed as follows:

$$J\ddot{\theta} + B\dot{\theta} + A\text{sgn}(\dot{\theta}) + \tau_g \sin \theta = \tau_e + \tau_{h,k}. \quad (4.1)$$

Since the joint stiffness part in previous model (3.1) is relatively small and negligible, it is no longer used here.

4.2.2 The Sit-to-Stand Movement

A schematic view of a subject wearing a lower-limb exoskeleton and performing STS transfer task is shown in Figure 4.1. During the STS movement, the human body in the sagittal plane can be modeled using a triple inverted pendulum. The whole body includes three segments: shank-foot, thigh and HAT (Head-Arm-Torso). The exoskeleton, attached to the human body, is represented by the gray rounded rectangles. The physical parameters of each segment are listed in the Symbols part. Assumed that the movements of the two legs during the STS movement are synchronous and simultaneous. The seat force is modeled as an external force ($\mathbf{F} = (F_{sx}, F_{sy})$) that acts on the inverted pendulum, as shown in Figure 4.1.

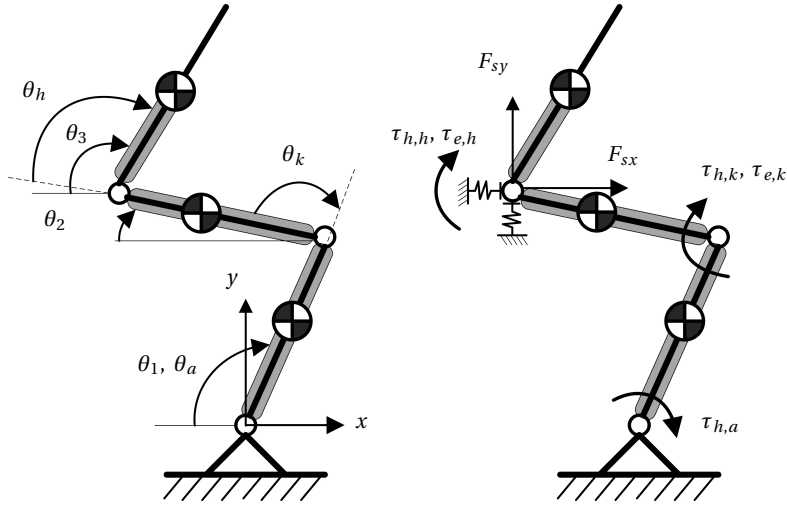


Figure 4.1 – Schematic view of a subject wearing an exoskeleton and achieving the STS motion in the sagittal plane.

Using to the Euler-Lagrange formalism [122], the dynamic model of the whole system is described by:

$$\mathbf{M}(\mathbf{q})\ddot{\mathbf{q}} + \mathbf{C}(\mathbf{q}, \dot{\mathbf{q}})\dot{\mathbf{q}} + \mathbf{G}(\mathbf{q}) = \mathbf{R}\boldsymbol{\tau} + \mathbf{J}_F^T \mathbf{F}, \quad (4.2)$$

where $\mathbf{q} = [q_1, q_2, q_3]^T = [\theta_1, \theta_2, \theta_3]^T$ represents the state vector. \mathbf{J}_F is the Jacobian matrix. Note that the solid and viscous friction forces of the human and exoskeleton joints are ignored, due to their negligible effect during the STS movement [123]. The control input vector $\boldsymbol{\tau}$ and the external seat force \mathbf{F} satisfy:

$$\boldsymbol{\tau} = \boldsymbol{\tau}_h + \boldsymbol{\tau}_e = \begin{bmatrix} \tau_{h,a} \\ \tau_{h,k} \\ \tau_{h,h} \end{bmatrix} + \begin{bmatrix} 0 \\ \tau_{e,k} \\ \tau_{e,h} \end{bmatrix}, \quad \mathbf{F} = \begin{bmatrix} F_{sx} \\ F_{sy} \end{bmatrix}. \quad (4.3)$$

Here $\boldsymbol{\tau}_h$ is used to denote the human efforts generated by the three human joints. $\boldsymbol{\tau}_e$ represents the output torques of the exoskeleton at the knee and hip joint level. Both ankle joints of the

4.3. Control Algorithms: Active Impedance Control Structure

E-ROWA exoskeleton are passive. The transformation matrix \mathbf{R} is given as follows:

$$\mathbf{R} = \mathbf{J}_{\Theta}^{-T}, \quad (4.4)$$

where \mathbf{J}_{Θ} represents the transformation matrix from the joint space $(\theta_a, \theta_k, \theta_h)$ to the defined angle space $(\theta_1, \theta_2, \theta_3)$ as shown in Figure 4.1. Definitions of the matrices $\mathbf{M}(\mathbf{q})$, $\mathbf{C}(\mathbf{q}, \dot{\mathbf{q}})$, $\mathbf{G}(\mathbf{q})$, \mathbf{J}_{Θ} , and \mathbf{J}_F are given in Appendix A.

Note that the seat force takes the major role for compensating the human gravity when the wearer is in the sitting position. Here, the seat force is assumed to be equivalent to two forces, F_{sx} and F_{sy} , acting at the hip joint. These two forces are supposed to compensate the torques acting at the knee and ankle joint level by the human gravity during the sitting position (i.e., the wearer's knee and ankle joint are free at the sitting position). At the same time, they should fade to zero, when the position of the hip joint is higher than a certain height (i.e., "Seat-Off" point). In practice, however, joint angle information are not sufficient to detect the seat-off point as the chairs' height may change. On the other hand, it is shown that the maximum vertical GRF time well approximates the "Seat-Off" time [119]. Hence, the model of the seat forces can be designed as follows:

$$\mathbf{F} = \beta_F [c_x \ c_y]^T, \quad (4.5)$$

with

$$\beta_F = 1 - F_{GRF}/F_{GRF,max},$$

where the required seat forces, c_x and c_y , are calculated based on the aforementioned conditions and the dynamic model (4.2). These parameters are also given in Appendix A. β_F indicates a positive ratio ($\beta_F \in [0 \ 1]$). F_{GRF} denotes the measured vertical ground reaction force, while $F_{GRF,max}$ represents the maximum vertical GRF.

4.3 Control Algorithms: Active Impedance Control Structure

The mechanical impedance is defined as the measure of the human torque (\mathcal{T}_h) induced by the joint movements (Θ) (see Figure 4.2). When the user wears the exoskeleton, the impedance of the human limb is affected by the exoskeleton. If the exoskeleton is passive, the total impedance of the exoskeleton is added to that of the human limb. Because the resultant impedance of the human exoskeleton system is higher than that of the human limb (i.e., $Z_h + Z_e > Z_h$), the movements of the limb naturally require additional human effort. In particular, the joint impedances of some motor-driven exoskeletons, Z_e , are relatively large due to the large masses and high frictions. To reduce the human effort needed to move the limb, the exoskeleton should be able to provide a lower passive or an active impedance (Z_e^d). In other words, if the impedance of the human exoskeleton system can be reduced to a level lower than that of the original impedance of the human limb (i.e., $Z_e^d + Z_h < Z_h$), the human

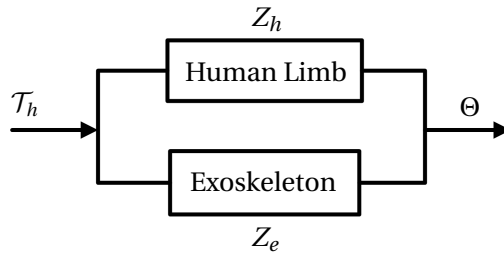


Figure 4.2 – The original impedance of the human exoskeleton system. Z_h and Z_e denote the impedance of the human limb and the exoskeleton respectively. \mathcal{T}_h represents the human joint torque, while Θ is the joint angle (in case study I, $\mathcal{T}_h = \tau_{h,k}$, $\Theta = \theta$; in case study II, $\mathcal{T}_h = \tau_h$, $\Theta = q$).

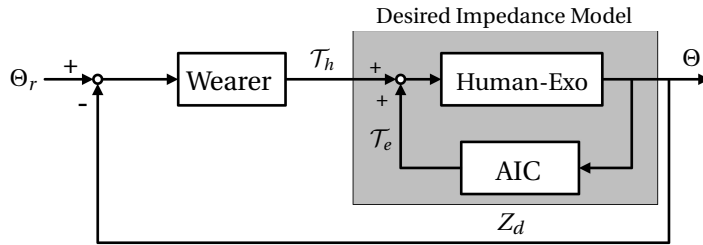


Figure 4.3 – Whole human-in-loop control structure with the exoskeleton's power assistance. AIC denotes the active impedance control, and Human-Exo the human exoskeleton system. Z_d denotes the desired impedance of the human exoskeleton system, and \mathcal{T}_e the assistive torque provided by the exoskeleton (in case study I, $\mathcal{T}_e = \tau_e$; in case study II, $\mathcal{T}_e = \tau_e$).

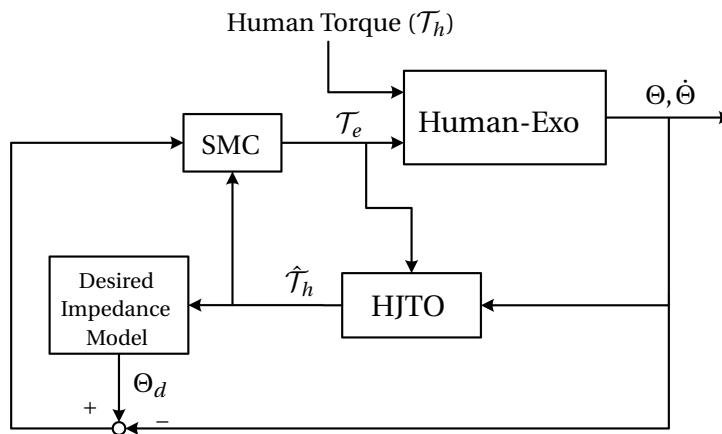


Figure 4.4 – Structure of the nonlinear active impedance control (AIC) ($\hat{\mathcal{T}}_h$: estimated human torque; Θ_d : desired joint angle).

effort needed to ensure the same lower limb movement can also be reduced.

Considering the requirements for reducing the wearer's efforts: the goal is to control the exoskeleton in such a way as to reduce the impedance of the human exoskeleton system to a desired level (see Figure 4.3). Note that the desired impedance, Z_d , is only valid when the system is stable. If the whole human-in-loop system is unstable, the desired joint movement may not be achieved by the wearer (Figure 4.3) or the wearer needs to provide additional muscular effort to stabilize the system. Hence, the stability and robustness of the AIC with respect to the modeling uncertainties should be taken into account in order to show the limitation of the desired impedance design.

Figure 4.4 shows the proposed nonlinear active impedance control structure, which consists of three parts: a nonlinear human joint torque observer (HJTO), a desired impedance model and a sliding mode controller (SMC). The principle of this structure is as follows: the nonlinear observer is used to estimate the human joint torque (\mathcal{T}_h) and the sliding mode controller is used to track the reference motion trajectory (Θ_d) generated by the desired impedance model. The original human exoskeleton model can be adapted to the desired impedance model with respect to the estimated human torque ($\hat{\mathcal{T}}_h$) if the following conditions are satisfied: 1) the nonlinear observer can accurately estimate the human joint torque (i.e., $\hat{\mathcal{T}}_h = \mathcal{T}_h$); 2) the SMC controller shows a high tracking accuracy (i.e., $\Theta = \Theta_d$).

In general, the observer has characteristics similar to those of a low-pass filter. High estimation accuracy of the nonlinear observer can only be obtained at a given constant frequency or within a given velocity range of the observed signals. Hence, the HJTO is designed based on the main frequency range of human motion. Regarding the design of the SMC, an NDO-based SMC is used to ensure a high control gain. From the exoskeleton's point of view, the human effort is considered an external disturbance in the control scheme. Hence, the human joint torque observer is also used as a disturbance observer in the exoskeleton controller (SMC). In the following subsections, we present the design of the active impedance control structure (see Figure 4.4) as well as its characteristics, performance and robustness in both case studies.

4.4 Active Impedance Controller Design for Single-joint Movements

4.4.1 Human Joint Torque Observer

From the human exoskeleton system's viewpoint, the human joint torque, $\tau_{h,k}$, can be considered an external disturbance. According to the disturbance observer (3.4) developed for the lower level control strategy (Section 3.3.1), the human joint torque observer can be designed as follows:

$$\begin{cases} \hat{\tau}_{h,k} &= z + p(\mathbf{x}) \\ \dot{z} &= L[-f_1(\mathbf{x}) - f_2(\mathbf{x})\tau_e - f_2(\mathbf{x})(z + p(\mathbf{x}))], \end{cases} \quad (4.6)$$

with

$$f_1(\mathbf{x}) = \begin{bmatrix} x_2 \\ \frac{1}{J}(-\tau_g \sin x_1 - A \operatorname{sgn}(x_2) - Bx_2) \end{bmatrix},$$

$$f_2(\mathbf{x}) = \begin{bmatrix} 0 \\ \frac{1}{J} \end{bmatrix},$$

where $\mathbf{x} = [x_1 \ x_2]^T = [\theta \ \dot{\theta}]^T$ is a defined state vector of the human exoskeleton system (4.1). $\hat{\tau}_{h,k}$ is the estimation of the human input torque $\tau_{h,k}$. $p(\mathbf{x})$ is also chosen as $p(\mathbf{x}) = k_1\theta + k_2\dot{\theta}$, and k_1 and k_2 are two positive constants. z is an auxiliary variable that is used to avoid the acceleration measurement. L satisfies:

$$L = \frac{\partial p(\mathbf{x})}{\partial \mathbf{x}} = [k_1 \ k_2]. \quad (4.7)$$

From (4.1) and (4.6), the dynamics of the estimated human joint torque are calculated as follows:

$$\dot{\hat{\tau}}_{h,k} = Lf_2 \cdot (\tau_{h,k} - \hat{\tau}_{h,k}). \quad (4.8)$$

Define the estimation error of the human torque as:

$$\tilde{\tau}_{h,k} = \tau_{h,k} - \hat{\tau}_{h,k}. \quad (4.9)$$

In the design of a conventional nonlinear disturbance observer, disturbances (e.g., frictions) are usually considered to be constant or to be changing with a small velocity [92]. However, the human torque associated with performing activities of daily living generally shows high variability, $\dot{\tau}_h$, that cannot be neglected. Assume that the velocity of the human torque is bounded, $\exists \kappa > 0$, $\|\dot{\tau}_{h,k}\|_\infty < \kappa$. The following proposition addresses the stability and tracking precision of the nonlinear observer.

Proposition 4.1. Assume that the Human Exo system is subject to human torque, $\tau_{h,k}$, described by (4.1) and the rate of change of the disturbance is bounded i.e., $\exists \kappa > 0$, $\|\dot{\tau}_{h,k}\|_\infty < \kappa$. The nonlinear observer is given in (4.6). The estimation error, $\tilde{\tau}_{h,k}$, is globally uniformly ultimately bounded.

Proof. Choose the Lyapunov function W as:

$$W = \frac{1}{2} \tilde{\tau}_{h,k}^2. \quad (4.10)$$

By the derivation of the Lyapunov function W and using (4.8), we obtain:

$$\begin{aligned}
 \dot{W} &= \tilde{\tau}_{h,k} \dot{\tilde{\tau}}_{h,k} \\
 &= \tilde{\tau}_{h,k} (\dot{\tilde{\tau}}_{h,k} - \dot{\hat{\tau}}_{h,k}) \\
 &= \tilde{\tau}_{h,k} (\dot{\tilde{\tau}}_{h,k} - L f_2 \tilde{\tau}_{h,k}) \\
 &\leq \|\tilde{\tau}_{h,k}\| \kappa - L f_2 \tilde{\tau}_{h,k}^2 \\
 &= \|\tilde{\tau}_{h,k}\| \kappa - L f_2 \|\tilde{\tau}_{h,k}\|^2 \\
 &= \|\tilde{\tau}_{h,k}\| \left(\kappa - \frac{k_2}{J} \|\tilde{\tau}_{h,k}\| \right).
 \end{aligned}$$

Hence, $\dot{W} \leq 0$, $\forall \|\tilde{\tau}_{h,k}\| \geq \frac{\kappa}{k_2}$. It can be observed that the tracking error ($\tilde{\tau}_{h,k}$) is globally uniformly ultimately bounded. \square

Note that the estimation error is determined from the human torque velocity and the parameter k_2 . Although the estimation error can be restricted to a relatively small range by choosing an appropriately high value of the parameter k_2 , in this way, more measurement noise of the angular velocity $\dot{\theta}$ is included in the estimated torque, $\hat{\tau}_{h,k}$. Hence, a trade-off between torque estimation accuracy and noise suppression should be made for the purpose of practical experimentation. In this study, the value of the parameter k_2 is obtained based on the main frequency range (0.5 - 5 Hz, [124]) of human lower limb motion.

4.4.2 Sliding Mode Controller (SMC)

For the design of the sliding mode controller, a first-order sliding surface is used as follows:

$$s = c_1 e + \dot{e} \quad \text{with} \quad e = \theta - \theta_d, \quad (4.11)$$

where θ_d denotes the desired trajectory and c_1 is a positive constant.

To improve the control gain, the estimated human torque, $\hat{\tau}_{h,k}$, is considered a disturbance of the exoskeleton system. A nonlinear disturbance observer (NDO) based SMC is then designed as follows:

$$\tau_e = -Jc_1 \dot{e} + \tau_g \sin \theta + A \text{sgn}(\dot{\theta}) + B\dot{\theta} - \hat{\tau}_{h,k} + J\ddot{\theta}_d - \lambda s - \sigma \text{sgn}(s), \quad (4.12)$$

with

$$\lambda = \lambda_0 \frac{1 + \beta_1 |e|}{1 + \beta_2 |\hat{\tau}_{h,k}|}, \quad \sigma = \begin{cases} \sigma_0, & |e| \geq E_0 \\ 0, & |e| < E_0 \end{cases} \quad (4.13)$$

where λ_0 , β_1 , β_2 and E_0 are positive constants. $\sigma_0 > |\hat{\tau}_{h,max}|$. $|\hat{\tau}_{h,max}|$ represents the upper bound of the estimation error of the torque observer.

The variable λ increases with the tracking error, e , and decreases with the derivation of the estimated human torque, $\dot{\hat{\tau}}_{h,k}$. Additionally, the nonlinear control term $\sigma \text{sgn}(s)$ is used only when the tracking error, e , exceeds a given range, E_0 . Use of the designed λ and σ , as shown in (4.13), can significantly reduce the effects of SMC chattering on the estimated human torque and limit the tracking error to a relatively small range. The stability of the exoskeleton system using the NDO-based SMC is addressed in the following proposition.

Proposition 4.2. Consider the exoskeleton system (4.1) with an NDO-based SMC (4.12). Assume that the estimation error of the human torque, $\tilde{\tau}_h$, is bounded; then, the trajectory of the system (4.1) can be driven onto the sliding surface (4.11).

Proof. Choose the Lyapunov function V as:

$$V = \frac{1}{2}s^2. \quad (4.14)$$

By differentiating (4.14), we get:

$$\dot{V} = s\dot{s} = s\frac{1}{J}(-\tau_g \cos\theta - A\text{sgn}(\dot{\theta}) - B\dot{\theta} + \tau_e + \tau_{h,k}) + c_1\dot{e} - s\ddot{d}. \quad (4.15)$$

By substituting (4.12) into the derivative of the Lyapunov function, we obtain:

$$\dot{V} = \frac{1}{J}s(\tilde{\tau}_{h,k} - \sigma \text{sgn}(s)) - \frac{1}{J}\lambda s^2. \quad (4.16)$$

If $|e| \geq E_0$, then, $\dot{V} \leq -\frac{1}{J}\lambda s^2 \leq 0$.

If $|e| < E_0$, then,

$$\begin{aligned} \dot{V} &= \frac{1}{J}s\tilde{\tau}_{h,k} - \frac{1}{J}\lambda s^2 \\ &\leq \frac{1}{J}|s||\tilde{\tau}_{h,max}| - \frac{1}{J}\lambda s^2 \\ &= \frac{1}{J}|s|(|\tilde{\tau}_{h,max}| - \lambda|s|). \end{aligned}$$

Therefore, $\forall |s| > \frac{|\tilde{\tau}_{h,max}|}{\lambda}$, the Lyapunov function is decreasing. It can be seen that the tracking error is globally uniformly ultimately bounded. According to Proposition 4.2, the $|\tilde{\tau}_{h,max}|$ can be restricted to a relatively small range. In particular, when the human torque $\tau_{h,k} = 0$, the parameter $\tilde{\tau}_h$ converges to zero, and the corresponding tracking error converges to zero as well ($\dot{V} \leq 0$). \square

4.4.3 Desired Impedance Model

According to the impedance control structure (Figure 4.4), the desired impedance model determines the real joint impedance that the wearer can effectively feel. The human effort needed to perform knee joint movements can be reduced by choosing a relatively small desired impedance, Z_d . To respectively test the effectiveness of the inertia, damping and stiffness reduction, a linear impedance model is chosen, as follows:

$$Z_d = \frac{\theta(s)}{\tau_{h,k}(s)} = \frac{1}{J_d s^2 + B_d s + K_d}, \quad (4.17)$$

where J_d , B_d and K_d represent the desired inertia, damping and stiffness factors, respectively.

Here, the stiffness is used to denote the gravitational torque acting at the knee joint. The design of the parameter K_d determines the level of gravity compensation and can be expressed as follows:

$$K_d = \alpha \tau_g, \quad (4.18)$$

where α is the compensation ratio.

As mentioned in Section 4.3, if the desired impedance is smaller than that of the human joint ($Z_d < Z_h$), the human effort can be reduced compared to the case in which no exoskeleton assistance is provided. To examine the effectiveness of the impedance reduction, two sample simulations are carried out. The parameters of the human shank and the exoskeleton system are set as follows: $J_h = 0.2587 \text{ Kg} \cdot \text{m}^2$, $J_e = 0.08 \text{ Kg} \cdot \text{m}^2$, $B_h = 1.5569 \text{ Nm} \cdot \text{s} \cdot \text{rad}^{-1}$, $B_e = 0.408 \text{ Nm} \cdot \text{s} \cdot \text{rad}^{-1}$, $\tau_{g,h} = 9.2305 \text{ Nm}$, $\tau_{g,e} = 0.4150 \text{ Nm}$, $A = 0.187 \text{ Nm}$. The processes used to identify these parameters will be detailed in Section 4.6. A PID controller is used to replace the wearer's role, as illustrated in Figure 4.3.

To assess the performance of the AIC structure, a comparative simulation study is first conducted. The human limb impedance is chosen as the desired impedance model (i.e., $J_d = J_h$, $B_d = B_h$ and $K_d = \alpha_1 \tau_{g,h} = \frac{\sin(\theta)}{\theta} \tau_{g,h}$). Based on the proposed AIC structure, the human exoskeleton system is controlled using a PID controller (i.e., the wearer, see Figure 4.3) to track a given reference angular position trajectory, θ_r , (Figure 4.5(a)). At the same time, the human torque generated by the PID controller, $\tau_{h,k}$, is also given as the input of the desired impedance model to generate a knee joint movement, θ_m . Figure 4.5(a) shows the real joint angular position trajectory, θ , and the angular position trajectory θ_m that is directly generated by the desired impedance model. It can be observed that these two trajectories match very well. This means that the impedance model of the human exoskeleton system can be accurately adapted to the desired impedance. At the same time, the nonlinear joint torque observer gives a precise estimation of the human joint torque (see Figure 4.5(b)).

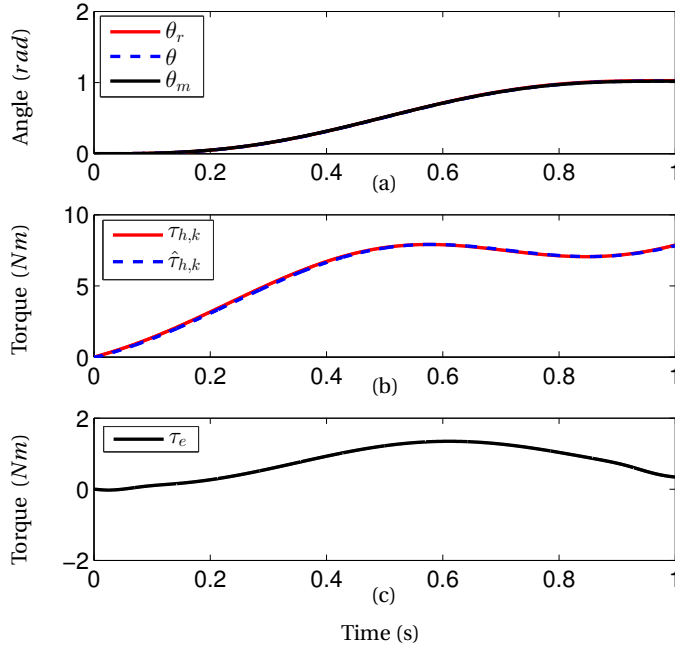


Figure 4.5 – Effectiveness of the active impedance control structure. (a) the reference joint angle, θ_r , the real joint angle, θ , and the joint angle, θ_m , generated by the human limb impedance model with the same human joint torque. (b) the human joint torque, $\tau_{h,k}$, and the estimated human joint torque using the nonlinear observer, $\hat{\tau}_{h,k}$. (c) the exoskeleton assistive torque, τ_e .

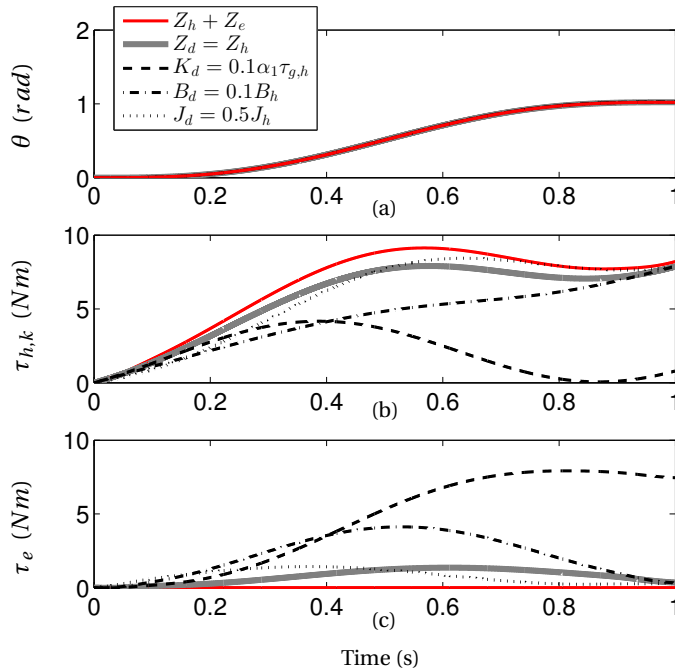


Figure 4.6 – Human torques with different desired impedance models.

Figure 4.6 shows the human joint torques required to perform the same sinusoidal knee joint flexion/extension movement within the constraints of different desired impedance models. It should be noted that the human effort required to ensure the same knee joint movement clearly increases when the exoskeleton is worn ($Z_h + Z_e$, see Figure 4.6(b)). If the desired impedance model is equal to the human joint model (i.e., $Z_d = Z_h$ ($J_d = J_h$, $B_d = B_h$ and $K_d = \alpha_1 \tau_{g,h}$)), the corresponding human joint torques are almost the same (see Figure 4.5(b) and Figure 4.6(b)). Furthermore, reducing the stiffness of the human exoskeleton system, $K_d = 0.1\alpha_1 \tau_{g,h}$, leads to a significant decrease in the human torque, $\tau_{h,k}$. The increase in human torque caused by damping can also be removed by setting a relatively small desired damping factor, $B_d = 0.1B_h$. During the beginning period ($< 0.5s$), a slight reduction of the human torque can be achieved by setting a small desired inertia factor, $J_d = 0.5J_h$. This means that the human effort can be efficiently reduced by setting a small desired impedance.

Note that the desired impedance, Z_d , for a practical human exoskeleton system cannot be infinitely small because a desired impedance that is too small may result in instability of the human exoskeleton system due to the modeling uncertainties. This will be illustrated in the following subsection.

4.4.4 Robustness with Respect to Modeling Uncertainties

A prerequisite for reducing the impedance of the human exoskeleton system using the proposed control structure (see Figure 4.4) is that the closed-loop human exoskeleton control system must be stable. Otherwise, it may cause instability of the whole wearer-in-loop system (see Figure 4.3) or unnecessary human torques for stabilizing the whole system. Generally, the torque sensorless control structure is sensitive to modeling uncertainties. Consider the fact that human limb parameters are difficult to estimate accurately (i.e., certain unknown uncertainties are implicitly included in the human exoskeleton model); therefore, the robustness of the proposed impedance control method with respect to the modeling uncertainties should be guaranteed.

Figure 4.7 represents the impedance control system with modeling uncertainties. Assume that the real Human-Exo system, H^* , consists of the identified human model, H , and a bounded modeling uncertainty, $\|\Delta\|_\infty < 1$, as follows:

$$H^* = H(1 + \Delta). \quad (4.19)$$

Here, HJTO* represents a modified nonlinear torque observer, i.e., the estimated joint torque including the torque generated by the human and that generated by the exoskeleton ($\hat{\tau} = \hat{\tau}_{h,k}^* + \tau_e$). According to the design of the nonlinear torque observer (4.6), the estimation error can be confined within a given small range by choosing appropriate parameter values. For simplicity, we assume that the modified nonlinear torque observer gives ideal estimation

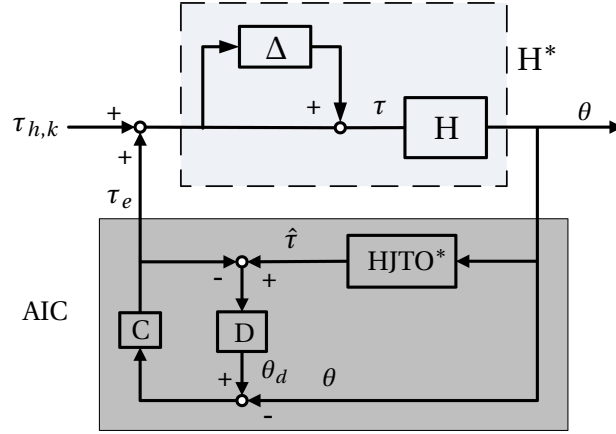


Figure 4.7 – Robustness analysis of the AIC: the nominal system, H , is the identified Human-Exo system; D and C represent the desired impedance model and the proposed controller, respectively.

performance. Then, we have:

$$HJTO^* = H^{-1}, \quad \tau = \hat{\tau} = \hat{\tau}_{h,k}^* + \tau_e, \quad (4.20)$$

where H^{-1} denotes the inverse dynamic model of the nominal system. Note that the estimated human torque, $\hat{\tau}_{h,k}^*$, is not equal to the human torque, $\tau_{h,k}$, due to modeling uncertainties.

From (4.1), (4.12) and (4.20), we obtain:

$$0 = J\ddot{e} + Jc_1\dot{e} + \lambda s + \sigma \text{sgn}(s). \quad (4.21)$$

By assuming that the initial desired angle is equal to the corresponding joint angle (i.e., $e(0) = 0$, $\dot{e}(0) = 0$), we have:

$$e = \theta - \theta_d = 0. \quad (4.22)$$

This means that the SMC has an ideal tracking performance. According to the desired impedance model (4.17), we obtain:

$$\hat{\tau}_{h,k}^* = J_d\ddot{\theta} + B_d\dot{\theta} + K_d\theta. \quad (4.23)$$

Then, (4.23) can be rewritten as follows:

$$\hat{\tau}_{h,k}^* = \Gamma(\theta, \dot{\theta}, \ddot{\theta})(J\ddot{\theta} + B\dot{\theta} + \tau_g \sin(\theta)), \quad (4.24)$$

where $\Gamma(\theta, \dot{\theta}, \ddot{\theta})$ denotes a positive impedance ratio.

From (4.1), (4.12), (4.20) and (4.24), the relationship between the τ_e and τ can be expressed as

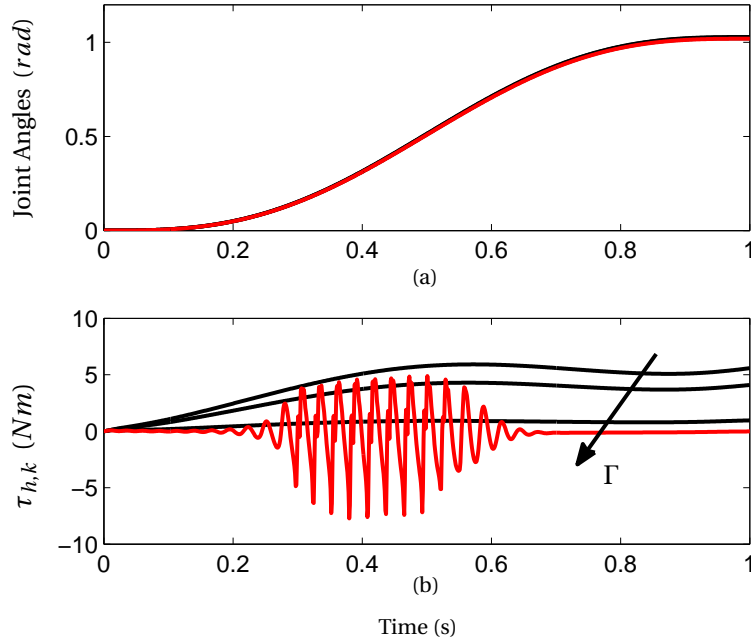


Figure 4.8 – Evaluation of the robust limitations.

follows:

$$\tau_e = (1 - \Gamma(\theta, \dot{\theta}, \ddot{\theta}))\tau + \Gamma(\theta, \dot{\theta}, \ddot{\theta})\text{Asgn}(\dot{\theta}). \quad (4.25)$$

According to the small gain theorem [125], the system is stable if:

$$\|(1 - \Gamma(\theta, \dot{\theta}, \ddot{\theta}))(1 + \Delta)\|_{\infty} < 1. \quad (4.26)$$

It can be noted that the minimum value of the impedance ratio, $\Gamma(\theta, \dot{\theta}, \ddot{\theta})$, is bounded by the uncertainty, Δ . Figure 4.20, which shows the result of a sample simulation, illustrates the robustness of the system with respect to the modeling uncertainties. A given modeling error, $\Delta = 0.4$, is added to the nominal system model. According to the whole control structure illustrated in Figure 4.3, a PID controller simulating the wearer's role is used to control the system to achieve a given joint extension movement (see Figure 4.20(a)) with four different impedance ratios ($\Gamma = 1, 0.8, 0.4, 0.28$). It can be observed that when Γ approaches the stability condition (4.26), an oscillating unnecessary human effort occurs (see Figure 4.20(b)). To guarantee stability, the design of the desired impedance model should take into account the system modeling uncertainties.

4.5 Active Impedance Controller Design for Multi-joint Movements

4.5.1 Human Joint Torque Observer

Following the design method of the single-joint HJTO as shown in Section 4.4.1, the multi-joint HJTO can be further developed using the disturbance observer technique [92], [126]. Correspondingly, the dynamic model (4.2), is transformed into a nominal model with an additional disturbance term represented by $\boldsymbol{\tau}_d = \mathbf{R}\boldsymbol{\tau}_h$:

$$\mathbf{M}(\mathbf{q})\ddot{\mathbf{q}} + \mathbf{C}(\mathbf{q}, \dot{\mathbf{q}})\dot{\mathbf{q}} + \mathbf{G}(\mathbf{q}) = \mathbf{R}\boldsymbol{\tau}_e + \mathbf{J}_F^T \mathbf{F} + \boldsymbol{\tau}_d. \quad (4.27)$$

The HJTO can be designed as follows:

$$\begin{cases} \dot{\mathbf{z}} = -\mathbf{L}(\mathbf{q}, \dot{\mathbf{q}})\mathbf{z} + \mathbf{L}(\mathbf{q}, \dot{\mathbf{q}})(\mathbf{C}(\mathbf{q}, \dot{\mathbf{q}})\dot{\mathbf{q}} + \mathbf{G}(\mathbf{q}) - \mathbf{R}\boldsymbol{\tau}_e - \mathbf{J}_F^T \mathbf{F} - \mathbf{p}(\mathbf{q}, \dot{\mathbf{q}})), \\ \hat{\boldsymbol{\tau}}_d = \mathbf{z} + \mathbf{p}(\mathbf{q}, \dot{\mathbf{q}}), \end{cases} \quad (4.28)$$

where $\hat{\boldsymbol{\tau}}_d$ indicates the estimated disturbance (i.e. the joint torques generated by the human, $\mathbf{R}\hat{\boldsymbol{\tau}}_h$), \mathbf{z} is an auxiliary variable used to avoid the acceleration measurement.

Regarding the design of the observer gain matrix $\mathbf{L}(\mathbf{q}, \dot{\mathbf{q}})$ and the vector $\mathbf{p}(\mathbf{q}, \dot{\mathbf{q}})$, a generalized approach is used as follows [126]:

$$\begin{cases} \mathbf{L}(\mathbf{q}, \dot{\mathbf{q}}) = \mathbf{X}^{-1} \mathbf{M}^{-1}(\mathbf{q}) \\ \mathbf{p}(\mathbf{q}, \dot{\mathbf{q}}) = \mathbf{X}^{-1} \dot{\mathbf{q}} \end{cases} \quad (4.29)$$

with

$$\mathbf{X}^{-1} = \frac{1}{2}(\zeta + 2\beta\sigma_2)\mathbf{I}, \quad (4.30)$$

where β is the minimum convergence rate of the joint torque observer (4.28). \mathbf{I} represents the identity matrix. ζ and σ_2 are two constants that satisfy the following conditions:

$$\|\mathbf{M}(\mathbf{q})\| \leq \sigma_2, \quad \|\dot{\mathbf{M}}(\mathbf{q})\| \leq \zeta \quad (4.31)$$

The design and limits of the convergence rate of the torque observer are analyzed in the following.

Let us define the disturbance tracking error as $\tilde{\boldsymbol{\tau}}_d = \boldsymbol{\tau}_d - \hat{\boldsymbol{\tau}}_d$. From (4.27) - (4.29), the error dynamics of the tracking disturbance can be obtained as follows:

$$\dot{\tilde{\boldsymbol{\tau}}}_d = \dot{\boldsymbol{\tau}}_d - \mathbf{L}(\mathbf{q}, \dot{\mathbf{q}})\tilde{\boldsymbol{\tau}}_d. \quad (4.32)$$

During the STS movement, the velocities of the human joint torques are bounded (i.e. $\|\dot{\boldsymbol{\tau}}_d\| <$

4.5. Active Impedance Controller Design for Multi-joint Movements

ε). As pointed out in [126], both the slow-varying and fast varying disturbance can be well tracked by the proposed NDO. The following lemma addresses the tracking performance of NDO (4.28) for system (4.27).

Lemma 4.1. [126] Consider the human-exoskeleton system subjects to the disturbance, $\boldsymbol{\tau}_d$ (i.e., the human joint torque). The human joint torque observer is given in (4.28) with the observer gain matrix $L(\boldsymbol{q}, \dot{\boldsymbol{q}})$ and auxiliary vector $\boldsymbol{p}(\boldsymbol{q}, \dot{\boldsymbol{q}})$ defined in (4.29). The matrix \boldsymbol{X} is invertible and there exists a positive definite and symmetric matrix $\boldsymbol{\Gamma}_x$, such that:

$$\boldsymbol{X} + \boldsymbol{X}^T - \boldsymbol{X}^T \dot{\boldsymbol{M}}(\boldsymbol{q}) \boldsymbol{X} \geq \boldsymbol{\Gamma}_x, \quad (4.33)$$

- 1) If the rate of change of the human torque is negligible (i.e., $\dot{\boldsymbol{\tau}}_d \approx 0$), the tracking error of the human joint torque, $\tilde{\boldsymbol{\tau}}_d$, converges exponentially to zero for any $\tilde{\boldsymbol{\tau}}_d \in R^n$.
- 2) If the rate of change of the human torque is bounded (i.e., $\|\dot{\boldsymbol{\tau}}_d\| < \varepsilon$), the tracking error of the human joint torque, $\tilde{\boldsymbol{\tau}}_d$, is globally uniformly ultimately bounded.

Here, the matrix \boldsymbol{X} given in (4.30) satisfies the above requirements. It should be noted that there is a trade-off between the convergence rate and the noise amplification. Regarding the control system, the reduction of the noise amplification usually makes the system more stable. Concerning the estimation of the human motion intention, however, a relatively high convergence rate is required.

4.5.2 Desired Impedance Model

According to the control scheme shown in Figure 4.3, one can notice that the desired impedance model determines the assistance level that should be provided by the exoskeleton. In other words, this is the real impedance that the wearer feels. Hence, the desired impedance model can be designed based on the wearer's motor ability to perform the STS movement (i.e., "assist-as-needed" strategy). To assess the lower limb strengths and balance dysfunctions, the well-know five-times-sit-to-stand test is usually used [127]. Researches in the literature show that an elderly with relatively longer standing-up time is usually associated with an increasing factor of disability, morbidity and fall risk [127]. According to the human-exoskeleton model (4.2), a time-varying desired impedance model is proposed as follows:

$$\lambda_1 (\boldsymbol{M}(\boldsymbol{q}) \ddot{\boldsymbol{q}}_r + \boldsymbol{C}(\boldsymbol{q}, \dot{\boldsymbol{q}}) \dot{\boldsymbol{q}}_r) + \lambda_2 \boldsymbol{G}(\boldsymbol{q}) = \boldsymbol{R} \hat{\boldsymbol{\tau}}_h + \boldsymbol{J}_F^T \boldsymbol{F}, \quad (4.34)$$

with

$$\lambda_1 = \lambda_2 = \text{diag}(1, \lambda_k, \lambda_h), \quad \lambda_k, \lambda_h \in (0, 1), \quad (4.35)$$

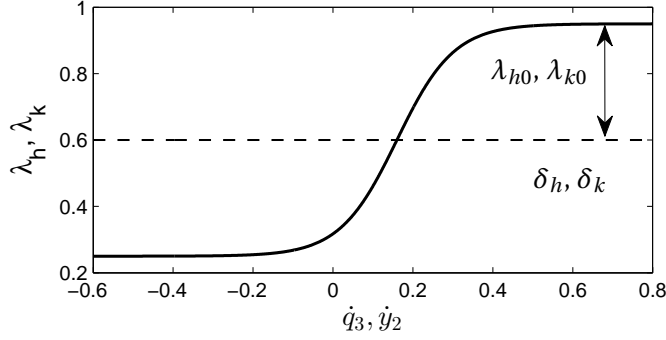


Figure 4.9 – One example of the function of λ_h and λ_k .

where λ_h and λ_k represent the assistive ratios. They are designed as follows:

$$\begin{cases} \lambda_h = \lambda_{h0} \tanh(s_h(\dot{q}_3 - \dot{q}_{3,0})) + \delta_h \\ \lambda_k = \lambda_{k0} \tanh(s_k(\dot{y}_2 - \dot{y}_{2,0})) + \delta_k \end{cases}, \quad (4.36)$$

\dot{q}_3 and \dot{y}_2 denote respectively the angular velocity and the vertical linear velocity of the hip joint, while $\dot{q}_{3,0}$ and $\dot{y}_{2,0}$ represent respectively the threshold values. s_k and s_h are respectively the sensitivity coefficients related to the function slope. Note that ankle joints are only controlled by the wearer so the intended trajectory of the ankle joint is considered to be equal to the current ankle joint angle (i.e., $\mathbf{q}_{r1} = \mathbf{q}_1$).

One example of the function (4.36) is shown in Figure 4.9. It can be observed that the λ_h and λ_k increase with the velocity \dot{q}_3 and \dot{y}_2 (i.e., the desired impedance increases with the standing up velocity). By contrast, the desired impedance decreases when the wearer stands up with a relatively low speed (i.e., lack of motor ability).

4.5.3 Design of the Sliding Mode Controller

In order to accurately achieve the reference motion intention, \mathbf{q}_r , computed using the desired impedance model (4.34), the tracking performance of the controller is a key factor. Hence, a disturbance observer based sliding mode controller is proposed, which has a high control gain. The human torque, $\boldsymbol{\tau}_h$, is considered as an external disturbance for the exoskeleton controller.

Let us define:

$$\mathbf{s} = c_1 \mathbf{e} + \dot{\mathbf{e}}, \quad \mathbf{e} = \mathbf{q} - \mathbf{q}_r \quad (4.37)$$

where \mathbf{s} represents a virtual error vector. \mathbf{q}_r is the trajectory computed using the desired impedance model (4.34). c_1 is a positive constant.

The multi-joint NDO based SMC controller is designed as follows:

$$\mathbf{U}_e = -c_1(\mathbf{M}(\mathbf{q})\dot{\mathbf{e}} + \mathbf{C}(\mathbf{q}, \dot{\mathbf{q}})\mathbf{e}) + \mathbf{M}(\mathbf{q})\ddot{\mathbf{q}}_r + \mathbf{C}(\mathbf{q}, \dot{\mathbf{q}})\dot{\mathbf{q}}_r + \mathbf{G}(\mathbf{q}) - \mathbf{J}_F^T \mathbf{F} - \sigma_1 \text{sat}(\mathbf{s}) - \hat{\mathbf{U}}_h, \quad (4.38)$$

with

$$\mathbf{U}_e = \mathbf{R}\boldsymbol{\tau}_e, \quad \hat{\mathbf{U}}_h = \mathbf{R}\hat{\boldsymbol{\tau}}_h \quad (4.39)$$

where σ_1 is a positive constant. $\text{sat}(\cdot)$ denotes a saturation function ($\text{sat}(\cdot) \in [-1, 1]$). Note that ankle joints are only controlled by the wearer (i.e., $q_{r1} = q_1$, $e_1 = 0$ and $u_{r1} = 0$).

4.5.4 Analysis of the Tracking Performance

Regarding the motion-intention tracking controller, the stability of the human-exoskeleton system is addressed using the following proposition.

Proposition 4.3. The exoskeleton controller is given by (4.38), and $\mathbf{e}_1 = 0$, $\sigma > \|\tilde{\boldsymbol{\tau}}_d\|$. The virtual tracking error, \mathbf{s} , converges exponentially to zero for all $\mathbf{s}(0) \in R^3$.

Proof. Consider the following candidate Lyapunov Function:

$$V = \frac{1}{2} \mathbf{s}^T \mathbf{M}(\mathbf{q}) \mathbf{s}. \quad (4.40)$$

By differentiating both sides of (4.40), we obtain:

$$\dot{V} = \mathbf{s}^T \mathbf{M}(\mathbf{q}) \dot{\mathbf{s}} + \frac{1}{2} \mathbf{s}^T \dot{\mathbf{M}}(\mathbf{q}) \mathbf{s}. \quad (4.41)$$

Since $\dot{\mathbf{M}}(\mathbf{q}) - 2\mathbf{C}(\mathbf{q}, \dot{\mathbf{q}})$ is skew-symmetric, we have:

$$\mathbf{s}^T [\dot{\mathbf{M}}(\mathbf{q}) - 2\mathbf{C}(\mathbf{q}, \dot{\mathbf{q}})] \mathbf{s} = 0. \quad (4.42)$$

From (4.2), (4.42) and (4.38), equation (4.41) can be expressed as follows:

$$\begin{aligned} \dot{V} &= \mathbf{s}^T \mathbf{M}(\mathbf{q}) \dot{\mathbf{s}} + \mathbf{s}^T \mathbf{C}(\mathbf{q}, \dot{\mathbf{q}}) \mathbf{s} \\ &= \mathbf{s}^T (\mathbf{M}(\mathbf{q})c_1 \dot{\mathbf{e}} + \mathbf{M}(\mathbf{q})\ddot{\mathbf{e}} + \mathbf{C}(\mathbf{q}, \dot{\mathbf{q}})\mathbf{s}) \\ &= \mathbf{s}^T (\mathbf{M}(\mathbf{q})c_1 \dot{\mathbf{e}} + \mathbf{M}(\mathbf{q})\ddot{\mathbf{q}} - \mathbf{M}(\mathbf{q})\ddot{\mathbf{q}}_r + \mathbf{C}(\mathbf{q}, \dot{\mathbf{q}})\mathbf{s}) \\ &= \mathbf{s}^T (\mathbf{M}(\mathbf{q})c_1 \dot{\mathbf{e}} + \mathbf{U}_h + \mathbf{U}_e + \mathbf{J}_F^T \mathbf{F} - \mathbf{G}(\mathbf{q}) - \mathbf{C}(\mathbf{q}, \dot{\mathbf{q}})\dot{\mathbf{q}} - \mathbf{M}(\mathbf{q})\ddot{\mathbf{q}}_r + \mathbf{C}(\mathbf{q}, \dot{\mathbf{q}})\mathbf{s}) \\ &= \mathbf{s}^T (\mathbf{U}_h - \hat{\mathbf{U}}_h - \sigma \text{sat}(\mathbf{s})) \\ &= \mathbf{s}^T (\tilde{\mathbf{U}}_h - \sigma \text{sat}(\mathbf{s})) \leq 0. \end{aligned}$$

Therefore, the Lyapunov function is decreasing. This completes the proof. □

4.5.5 Robustness with Respect to Modeling Uncertainties

Considering the modeling uncertainties, the real human-exoskeleton system model can be represented as follows:

$$\mathbf{M}^*(\mathbf{q})\ddot{\mathbf{q}} + \mathbf{C}^*(\mathbf{q}, \dot{\mathbf{q}})\dot{\mathbf{q}} + \mathbf{G}^*(\mathbf{q}) = \mathbf{U} = \mathbf{U}_e + \mathbf{U}_h + \mathbf{J}_F^T \mathbf{F}, \quad (4.43)$$

where the parameter matrices satisfy:

$$\mathbf{M}^*(\mathbf{q}) = \mathbf{M}(\mathbf{q}) + \Delta\mathbf{M}(\mathbf{q}), \quad (4.44)$$

$$\mathbf{C}^*(\mathbf{q}, \dot{\mathbf{q}}) = \mathbf{C}(\mathbf{q}, \dot{\mathbf{q}}) + \Delta\mathbf{C}(\mathbf{q}, \dot{\mathbf{q}}), \quad (4.45)$$

$$\mathbf{G}^*(\mathbf{q}) = \mathbf{G}(\mathbf{q}) + \Delta\mathbf{G}(\mathbf{q}). \quad (4.46)$$

For both the identified and real human-exoskeleton systems, it is reasonable to assume that the parameter matrices have the following properties:

Property 4.1. The inertia matrices are symmetric and positive definite, i.e. we have:

$$\begin{aligned} \xi^T \mathbf{M}^*(\mathbf{q}) \xi &= \xi^T (\mathbf{M}^*(\mathbf{q}))^T \xi > 0 \\ \xi^T \mathbf{M}(\mathbf{q}) \xi &= \xi^T (\mathbf{M}(\mathbf{q}))^T \xi > 0, \quad \forall \mathbf{q}, \xi \in R^n. \end{aligned} \quad (4.47)$$

Property 4.2. The matrices $\frac{1}{2}\dot{\mathbf{M}}^*(\mathbf{q}) - \mathbf{C}^*(\mathbf{q}, \dot{\mathbf{q}})$ and $\frac{1}{2}\dot{\mathbf{M}}(\mathbf{q}) - \mathbf{C}(\mathbf{q}, \dot{\mathbf{q}})$ are all skew-symmetric and can be shown that:

$$\begin{aligned} \xi^T \left(\frac{1}{2}\dot{\mathbf{M}}^*(\mathbf{q}) - \mathbf{C}^*(\mathbf{q}, \dot{\mathbf{q}}) \right) \xi &= 0 \\ \xi^T \left(\frac{1}{2}\dot{\mathbf{M}}(\mathbf{q}) - \mathbf{C}(\mathbf{q}, \dot{\mathbf{q}}) \right) \xi &= 0, \quad \forall \mathbf{q}, \dot{\mathbf{q}}, \xi \in R^n. \end{aligned} \quad (4.48)$$

Property 4.3. Assume that the potential functions of the real and identified human-exoskeleton systems are $P_E^*(\mathbf{q}) > 0$ and $P_E(\mathbf{q}) > 0$. Then the gravitational terms in the corresponding models satisfy:

$$\mathbf{G}^*(\mathbf{q}) = \frac{\partial P_E^*(\mathbf{q})}{\partial \mathbf{q}}, \quad \mathbf{G}(\mathbf{q}) = \frac{\partial P_E(\mathbf{q})}{\partial \mathbf{q}}. \quad (4.49)$$

Lemma 4.2. The modeling uncertainty terms $\Delta\mathbf{M}(\mathbf{q})$, $\Delta\mathbf{C}(\mathbf{q}, \dot{\mathbf{q}})$ and $\Delta\mathbf{G}(\mathbf{q})$ also have the similar properties, i.e. we have:

$$\xi^T \Delta\mathbf{M}(\mathbf{q}) \xi = \xi^T (\Delta\mathbf{M}(\mathbf{q}))^T \xi > 0, \quad \forall \mathbf{q}, \xi \in R^n \quad (4.50)$$

$$\xi^T \left(\frac{1}{2}\Delta\dot{\mathbf{M}}(\mathbf{q}) - \Delta\mathbf{C}(\mathbf{q}, \dot{\mathbf{q}}) \right) \xi = 0, \quad \forall \mathbf{q}, \dot{\mathbf{q}}, \xi \in R^n \quad (4.51)$$

$$\Delta\mathbf{G}(\mathbf{q}) = \frac{\partial (P_E^*(\mathbf{q}) - P_E(\mathbf{q}))}{\partial \mathbf{q}}. \quad (4.52)$$

4.5. Active Impedance Controller Design for Multi-joint Movements

Proof. This lemma can be easily obtained from (4.44) to (4.46). □

Note that the real system model (4.43) can be rewritten as follows:

$$\mathbf{M}(\mathbf{q})\ddot{\mathbf{q}} + \mathbf{C}(\mathbf{q}, \dot{\mathbf{q}})\dot{\mathbf{q}} + \mathbf{G}(\mathbf{q}) = \mathbf{U} = \mathbf{U}_e + \mathbf{U}_h + \mathbf{J}_F^T \mathbf{F} + \mathbf{T}_d(\mathbf{q}, \dot{\mathbf{q}}, \ddot{\mathbf{q}}), \quad (4.53)$$

where the lumped disturbance is given by:

$$\mathbf{T}_d(\mathbf{q}, \dot{\mathbf{q}}, \ddot{\mathbf{q}}) = -\Delta\mathbf{M}(\mathbf{q})\ddot{\mathbf{q}} - \Delta\mathbf{C}(\mathbf{q}, \dot{\mathbf{q}})\dot{\mathbf{q}} - \Delta\mathbf{G}(\mathbf{q}). \quad (4.54)$$

Actually, the lumped disturbance $\mathbf{T}_d(\mathbf{q}, \dot{\mathbf{q}}, \ddot{\mathbf{q}})$ cannot be excluded in the estimated human torque $\hat{\mathbf{U}}_h$, because we use the nominal system parameters in the nonlinear disturbance observer (4.28). Thus, we have the following approximation in the steady state of tracking control:

$$\hat{\mathbf{U}}_h = \mathbf{U}_h + \mathbf{T}_d(\mathbf{q}, \dot{\mathbf{q}}, \ddot{\mathbf{q}}), \quad (4.55)$$

where \mathbf{U}_h is the generalized torque obtained from the actual human muscle strength. Therefore, the real desired impedance model used in the system is:

$$\lambda_1(\mathbf{M}(\mathbf{q})\ddot{\mathbf{q}}_r + \mathbf{C}(\mathbf{q}, \dot{\mathbf{q}})\dot{\mathbf{q}}_r) + \lambda_2\mathbf{G}(\mathbf{q}) = \hat{\mathbf{U}}_h = \mathbf{U}_h + \mathbf{T}_d(\mathbf{q}, \dot{\mathbf{q}}, \ddot{\mathbf{q}}). \quad (4.56)$$

The scaling matrices λ_1 and λ_2 are related to the desired robotic assistance and normally satisfy:

$$\|\lambda_1\|_\infty < 1, \quad \|\lambda_2\|_\infty < 1. \quad (4.57)$$

From (4.56), we know that even there is no human input \mathbf{U}_h , the reference trajectory \mathbf{q}_r might be unstable due to the lumped disturbance. To guarantee the safety of wearer, the stability of reference trajectory \mathbf{q} should be robust to the model uncertainty. The following theorem gives the sufficient condition of this robustness.

Proposition 4.4. For any $\forall \mathbf{q}_r \in R^n$, if the following inequalities:

$$\lambda_1\mathbf{M}(\mathbf{q}_r) + \Delta\mathbf{M}(\mathbf{q}_r) > 0, \quad (\lambda_2 - \mathbf{I})P_E(\mathbf{q}_r) + P_E^*(\mathbf{q}_r) > 0 \quad (4.58)$$

hold, then the equilibrium $\mathbf{q}_r - \mathbf{q}_{r0}$ is stable with $\lambda_2\mathbf{G}(\mathbf{q}_{r0}) + \Delta\mathbf{G}(\mathbf{q}_{r0}) = 0$.

Proof. Here we only investigate the situation where there is no human input and the trajectory tracking control has converged. The desired impedance model (4.56) can therefore be represented by:

$$\lambda_1(\mathbf{M}(\mathbf{q}_r)\ddot{\mathbf{q}}_r + \mathbf{C}(\mathbf{q}_r, \dot{\mathbf{q}}_r)\dot{\mathbf{q}}_r) + \lambda_2\mathbf{G}(\mathbf{q}_r) = \mathbf{T}_d(\mathbf{q}, \dot{\mathbf{q}}, \ddot{\mathbf{q}}). \quad (4.59)$$

By substituting (4.54) into (4.60), we obtain:

$$(\lambda_1 \mathbf{M}(\mathbf{q}_r) + \Delta \mathbf{M}(\mathbf{q}_r)) \ddot{\mathbf{q}}_r + (\lambda_1 \mathbf{C}(\mathbf{q}_r, \dot{\mathbf{q}}_r) + \Delta \mathbf{C}(\mathbf{q}_r, \dot{\mathbf{q}}_r)) \dot{\mathbf{q}}_r + \lambda_2 \mathbf{G}(\mathbf{q}_r) + \Delta \mathbf{G}(\mathbf{q}_r) = 0. \quad (4.60)$$

Obviously $\mathbf{q}_r - \mathbf{q}_{r0}$ is an equilibrium of system (4.60). Choose the Lyapunov candidate function as:

$$V = \frac{1}{2} \dot{\mathbf{q}}_r^T (\lambda_1 \mathbf{M}(\mathbf{q}_r) + \Delta \mathbf{M}(\mathbf{q}_r)) \dot{\mathbf{q}}_r + (\lambda_2 - \mathbf{I}) P_E(\mathbf{q}_r) + P_E^*(\mathbf{q}_r). \quad (4.61)$$

Then we have:

$$\begin{aligned} \dot{V} &= \dot{\mathbf{q}}_r^T (\lambda_1 \mathbf{M}(\mathbf{q}_r) + \Delta \mathbf{M}(\mathbf{q}_r)) \ddot{\mathbf{q}}_r + \frac{1}{2} \dot{\mathbf{q}}_r^T (\lambda_1 \dot{\mathbf{M}}(\mathbf{q}_r) + \Delta \dot{\mathbf{M}}(\mathbf{q}_r)) \dot{\mathbf{q}}_r \\ &\quad + \frac{d}{dt} [(\lambda_2 - \mathbf{I}) P_E(\mathbf{q}_r) + P_E^*(\mathbf{q}_r)] \\ &= -\dot{\mathbf{q}}_r^T [(\lambda_1 \mathbf{C}(\mathbf{q}_r, \dot{\mathbf{q}}_r) + \Delta \mathbf{C}(\mathbf{q}_r, \dot{\mathbf{q}}_r)) \dot{\mathbf{q}}_r + \lambda_2 \mathbf{G}(\mathbf{q}_r) + \Delta \mathbf{G}(\mathbf{q}_r)] \\ &\quad + \frac{1}{2} \dot{\mathbf{q}}_r^T (\lambda_1 \dot{\mathbf{M}}(\mathbf{q}_r) + \Delta \dot{\mathbf{M}}(\mathbf{q}_r)) \dot{\mathbf{q}}_r + [(\lambda_2 - \mathbf{I}) \frac{\partial P_E(\mathbf{q}_r)}{\partial t} + \frac{\partial P_E^*(\mathbf{q}_r)}{\partial t}] \\ &= \dot{\mathbf{q}}_r^T [\frac{1}{2} (\lambda_1 \dot{\mathbf{M}}(\mathbf{q}_r) + \Delta \dot{\mathbf{M}}(\mathbf{q}_r)) - (\lambda_1 \mathbf{C}(\mathbf{q}_r, \dot{\mathbf{q}}_r) + \Delta \mathbf{C}(\mathbf{q}_r, \dot{\mathbf{q}}_r))] \dot{\mathbf{q}}_r \\ &\quad - \dot{\mathbf{q}}_r^T [\lambda_2 \mathbf{G}(\mathbf{q}_r) + \Delta \mathbf{G}(\mathbf{q}_r)] + [(\lambda_2 - \mathbf{I}) \mathbf{q}_r^T \mathbf{G}(\mathbf{q}_r) + \mathbf{q}_r^T \mathbf{G}^*(\mathbf{q}_r)] \\ &\leq 0. \end{aligned}$$

Therefore, we can say that the equilibrium is stable. This completes the proof. \square

4.6 Experiments of Knee Joint Flexion/Extension Movements

The experiments were conducted with the participation of four healthy subjects (Table 4.1). The subjects are able to execute complete flexion and extension movements of the knee joint with no spasticity or contracture. All subjects were informed of the experimental protocols and gave their consent before participating in the experiments. Constraints on knee joint position, velocity, and acceleration were imposed, and security of the range of motion between full extension (90°) and full flexion (-30°) was ensured mechanically using mechanical joint limiters. All precautions were taken to not adversely affect the health of the participants.

4.6.1 Parametric Identification

The parameters of the human exoskeleton system (4.1) include two parts: the exoskeleton and the human limb parameters. To obtain the original impedance model of the human limb, these two parts are respectively identified using the following steps.

4.6. Experiments of Knee Joint Flexion/Extension Movements

Subjects	Sex	Age	Height (cm)	Weight (kg)
S ₁	Male	26	180	78
S ₂	Male	29	170	66
S ₃	Male	29	180	63
S ₄	Male	28	168	68

Table 4.1 – Subjects' Information

Systems	Inertia ($Kg \cdot m^2$)	Viscous friction ($Nm \cdot s \cdot rad^{-1}$)	Solid friction (Nm)	Gravitational torque (Nm)
EICOSI	0.08	0.408	0.187	0.4150
Subject S ₁	0.2800	1.9119	0	11.5534
Subject S ₂	0.2535	1.9599	0	9.5376
Subject S ₃	0.3030	2.1350	0	10.860
Subject S ₄	0.2260	1.9544	0	9.3176

Table 4.2 – System's identified parameters

A. Exoskeleton Parameters

During this step, only the exoskeleton is controlled in the sitting position. Sinusoidal angle trajectories, θ_r^e , with four different frequencies (0.2, 0.4, 0.6 and 0.8 Hz) are chosen as the reference trajectories. The exoskeleton is controlled using a basic proportional controller, $\tau_e = K_p(\theta_r^e - \theta)$, to track the reference trajectories. The real joint angle, θ , and the joint torque, τ_e , are recorded at 1 KHz. At each frequency, the identification process lasts approximately 25 seconds. The joint angular velocity and acceleration are calculated by once and twice derivation of the joint angle. According to the system model (4.1), it can be observed that the variables θ , $\dot{\theta}$, $\ddot{\theta}$ and τ_e are known, whereas the parameters J_e , B_e , A , and $\tau_{g,e}$ should be identified. On the basis of the system model (4.1) and the known variables, the remaining parameters are identified using the *regress* command, a linear least squares optimization based method, in MATLAB. The identified parameters are shown in Table 4.2.

B. Human Limb Parameters

The human limb parameters (J_h , B_h , and $\tau_{g,h}$) can be obtained using the dynamic model (4.1) if both the human exoskeleton parameters and the exoskeleton parameters are known. Because the exoskeleton parameters can be obtained using the aforementioned method, only the human exoskeleton parameters need to be identified. Similarly, the exoskeleton worn by the subjects is controlled to track a sinusoidal knee joint trajectory with four different frequencies (0.2, 0.4, 0.6 and 0.8 Hz). The subjects are asked not to exert any muscular effort

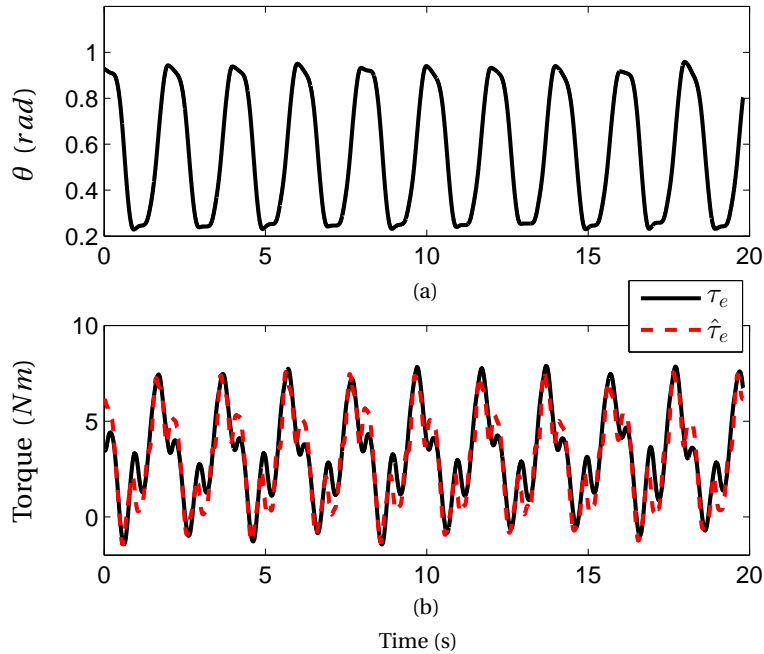


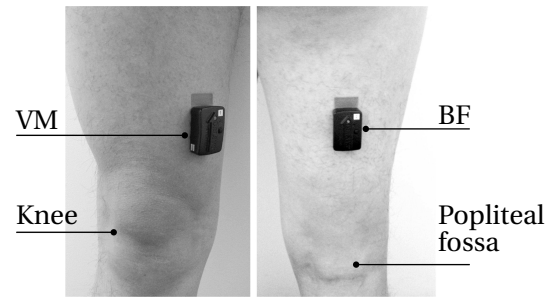
Figure 4.10 – Cross-validation results of one subject’s identified parameters. (a) the real knee joint angle. (b) the measured output torque of the actuator, τ_e , and the estimated output torque, $\hat{\tau}_e$, obtained using the human exoskeleton system (4.1) with the identified parameters.

Subject	Frequency (Hz)	$\ \Delta\ _{mean}$	$\ \Delta\ _{max}$
S_1	0.5	0.12	0.47
S_2	0.5	0.10	0.45
S_3	0.5	0.08	0.23
S_4	0.5	0.08	0.28

Table 4.3 – Magnitudes of the model uncertainties

4.6. Experiments of Knee Joint Flexion/Extension Movements

Figure 4.11 – EMG sensor placements for the muscles: *vastus medialis* (VM) and *biceps femoris* (BF).



(i.e., $\tau_{h,k} = 0$) during the identification process. The joint angles are also recorded during this period. At each frequency, the identification process lasts approximately 25 seconds as well. The unknown human exoskeleton parameters in the model (4.1) can be identified using the linear least squares optimization algorithm (i.e., the *regress* command in MATLAB) as well. The calculated human limb parameters are shown in Table 4.2. Note that the identified shank inertia J_h and gravity torque $\tau_{g,h}$ are similar to those estimated using the regression method proposed by P. De Leva [104]. For example, the identified values of J_h and $\tau_{g,h}$ of subject 2 are $2.2587 \text{ Kg} \cdot \text{m}^2$ and 9.2305 Nm , respectively, whereas the values estimated using the regression method presented in [104] are $2.2522 \text{ Kg} \cdot \text{m}^2$ and 9.33 Nm , respectively.

To evaluate the identified parameters and estimate the modeling error, a cross-validation study is performed. The exoskeleton worn by the subjects is controlled to track a 0.5 Hz sinusoidal reference angular position trajectory. Figure 4.10 shows a satisfactory convergence of the measured output torque of the actuator, τ_e , and the estimated output torque, $\hat{\tau}_e$, obtained using the human exoskeleton system (4.1) with the identified parameters. The average and maximum magnitudes of the modeling errors ($\|\Delta\|_{mean}$, $\|\Delta\|_{max}$) of each subject are calculated as shown in Table 4.3. All mean model errors are less than 12%.

4.6.2 Assessment Method

The main goal of this study is to decrease the impedance of the human exoskeleton system by providing active power assistance and thereby to further reduce the human effort required for limb motion. To evaluate the effectiveness of human effort reduction, EMG activity recordings of the knee muscle group (the *vastus medialis* (VM) and *biceps femoris* (BF)) are used as assessment metrics. The vastus medialis is one of the main muscles that drives the action of extending the knee in the sitting position, whereas the biceps femoris is one of the main muscles used in knee flexion. Two EMG sensors (Delsys, USA) are used for data acquisition in the following experiments (Figure 4.11). The measured raw EMG signals are processed using the following steps: high-pass filtering at 30 Hz using a fourth-order Butterworth filter, elimination of the measurement noise, and full-wave rectification.

To quantitatively analyze the relationship between the human joint torque and the corresponding EMG signals, a muscular dynamic model such as the Hill model and the EMG signals from all associated muscles are generally needed [128]. A simple quantitative method, which

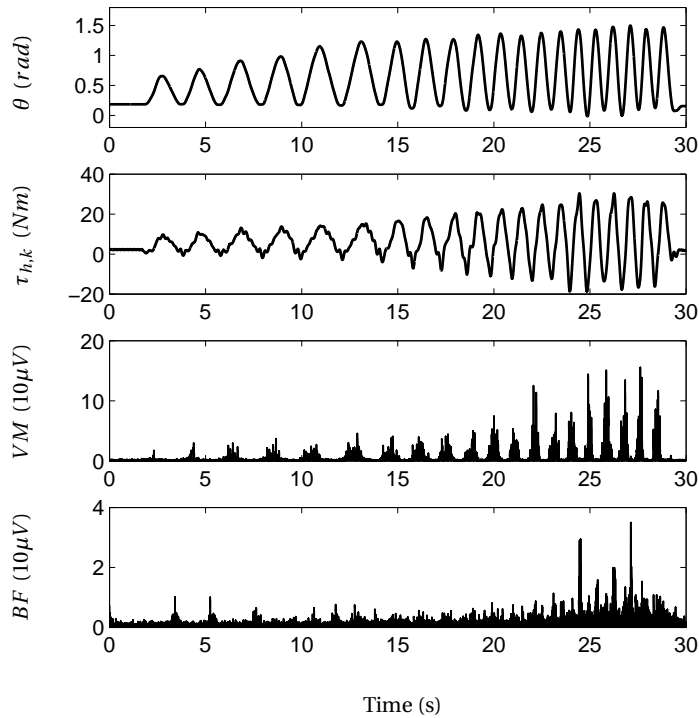


Figure 4.12 – The joint angles, the calculated human joint torque and the processed EMG signals of one subject during the correlation test.

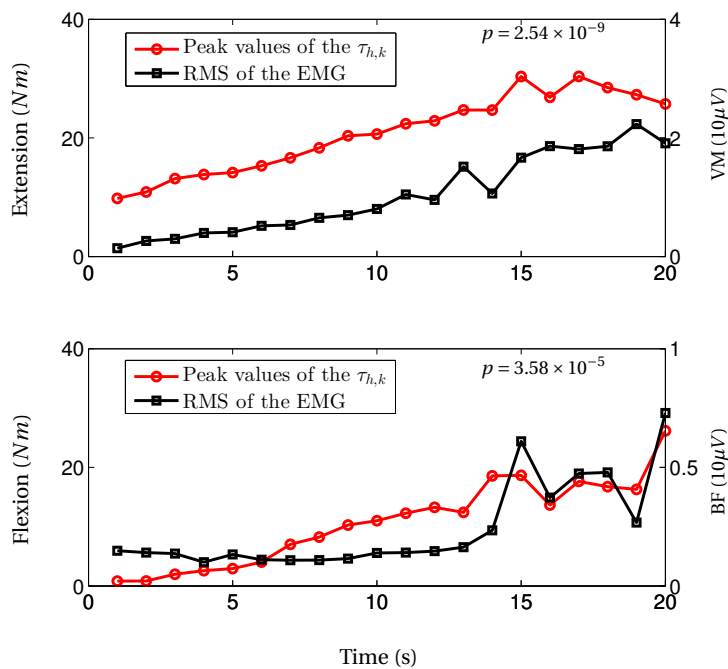


Figure 4.13 – The correlation between the amplitudes (i.e., the peak values) of the human joint torque and the RMS of the corresponding EMG signals of one subject [see Figure 4.12].

4.6. Experiments of Knee Joint Flexion/Extension Movements

uses EMG signal recordings from two muscles to give a reliable image of the human torque or human effort, is proposed. For flexion/extension knee joint movement, the root-mean-square (RMS) of the processed EMG signals is used as the assessment method to indicate the level of human joint torque.

Before beginning the experiments, a correlation test of the RMS of the EMG signals and the human knee joint torque, $\tau_{h,k}$, was conducted. Subjects wearing the exoskeleton were asked to perform flexion/extension movements with different amplitudes and frequencies (see Figure 4.12) while the exoskeleton was totally passive ($\tau_e = 0$). The EMG signals of the vastus medialis and biceps femoris were recorded. The human torque, $\tau_{h,k}$, is estimated using the human exoskeleton model (4.1) and the measured joint angle, θ . Figure 4.12 shows the knee joint angles, θ , the estimated human torque, $\tau_{h,k}$, and the processed EMG signals of one subject. The human torque, $\tau_{h,k}$, and the processed EMG signals show similar trends in terms of the knee joint angle's amplitude and frequency. Figure 4.13 shows the joint flexion/extension torque amplitude and the RMS of the associated muscles' EMG signals for each joint movement. There is a significant correlation ($p < 0.01$) between the EMG signals' RMS and the human torques for all subjects. Thus, it is rational to use the EMG signals' RMS to express the dynamic changes in the human torques and to reflect any increase or decrease in the related human effort.

4.6.3 Experimental Protocol

To show the effectiveness of the proposed AIC structure, two experiments were designed: the first is used to evaluate the reduction in human effort by decreasing joint impedance, and the second is conducted to verify the AIC's ability to separately compensate the desired inertia, damping and stiffness of the human joint impedance.

In the first experiment, four different impedance states were used, as follows:

- 1) Human joint impedance state (i.e., Z_h): the subjects swing their shanks without wearing the exoskeleton.
- 2) Human exoskeleton impedance state (i.e., $Z_h + Z_e$): the subjects swing their shanks while wearing the exoskeleton without any power assistance.
- 3) Exoskeleton impedance compensation state (i.e., $Z_d = Z_h$): the inertia, friction (damping) and gravity of the exoskeleton are all compensated (i.e., the desired impedance model is equal to the human limb model). Note that here $K_d = \alpha_1 \tau_{g,h}$ with $\alpha_1 = \frac{\sin(\theta)}{\theta}$.
- 4) Human impedance compensation state (i.e., $Z_d = 0.5Z_h$): the desired impedance of the AIC is set to 50% of the original human joint impedance. Note that the competition ratio is chosen based on the AIC's robustness with respect to the modeling uncertainties (4.26) and the real model errors (see Table 4.3).

The effectiveness of human effort reduction is evaluated by comparing the RMS of the EMG signals when the subjects perform the same flexion/extension movement under four different impedance conditions. Consider the fact that the gravity of the human shank-foot is used by the wearer to achieve knee joint flexion movements in the sitting position; the human joint flexion torque is not noticeable when the frequency of the joint movement is low. Hence, the joint extension torque (i.e., the EMG signals from the vastus medialis) is used as the main metric, whereas the EMG signals from the biceps femoris are measured to monitor the muscles' co-contraction. Correspondingly, the exoskeleton's power assistance is set to zero during flexion movements in all experiments.

The subjects are asked to move their shanks to track a virtual sinusoidal reference trajectory with 0.5-Hz frequency shown on a host PC display in front of the subject. The real knee joint angle is also shown on this PC display. Two IMU sensors (Xsens, Netherlands) attached to the shank and thigh, respectively, are used to measure the knee joint angle during the human joint impedance state. The knee joint angle is calculated based on the IMUs' measured gyros and accelerations [129].

In the second experiment, the desired inertia (J_d), damping (B_d) and stiffness (K_d) are further reduced from the values associated with the exoskeleton impedance compensation state. The effectiveness of human inertia, damping and stiffness compensation is evaluated by comparing the RMS of the EMG signals from the vastus medialis with those obtained under the exoskeleton impedance compensation state and the human joint impedance state. Furthermore, reference joint angle trajectories with different frequencies are used in this experiment. A low-frequency (0.25 Hz) reference trajectory is used to evaluate the effectiveness of the stiffness compensation. In this case, the influences of inertia and damping are relatively small. Conversely, a high-frequency (0.8 Hz) reference trajectory is employed to show the effectiveness of the inertia and damping compensation.

To avoid the occurrence of muscle fatigue in the subjects during the experiments, each continuous flexion/extension movement lasted no longer than 50 seconds, and one-minute rest period were provided to subjects between two consecutive flexion/extension movements.

4.6.4 Experimental Results

During all experiments, the EMG signals were recorded after the subjects were able to successfully track the virtual reference trajectories for a certain number of periods (> 5 periods). Figure 4.14 shows the knee joint angles and processed EMG signals of one subject during flexion/extension movements in four states: the human joint impedance state, the human-Exo impedance state, the exoskeleton impedance compensation state and the human impedance compensation state. The flexion/extension movements under different impedance states present nearly the same amplitudes and frequencies, and the measured EMG signals under each impedance state are relatively stable. For all experiments, the RMS of the EMG signals are calculated based on the data measured during 20 flexion/extension movements.

4.6. Experiments of Knee Joint Flexion/Extension Movements

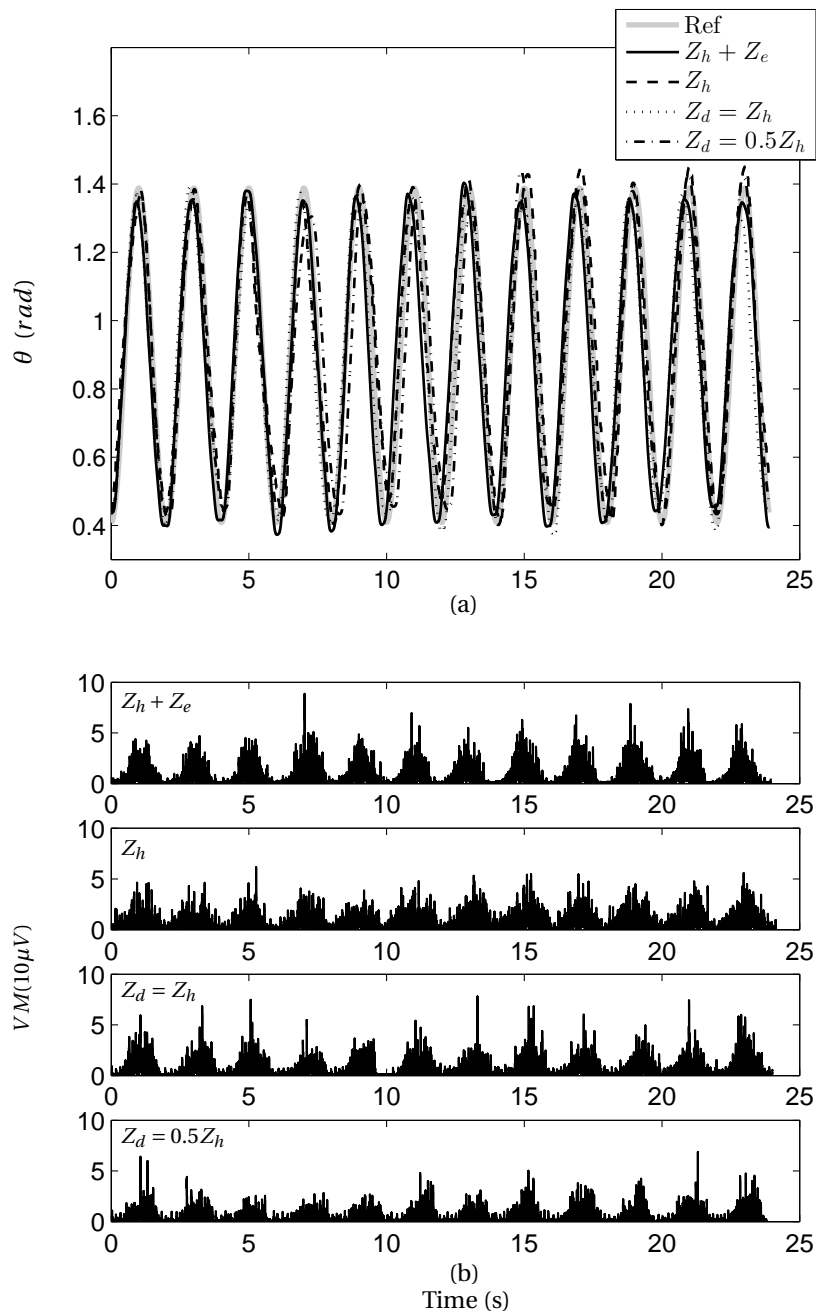


Figure 4.14 – One group of processed EMG signals during flexion/extension movements in the four states. (a) The knee joint angles. (b) the processed EMG signals of the vastus medialis.

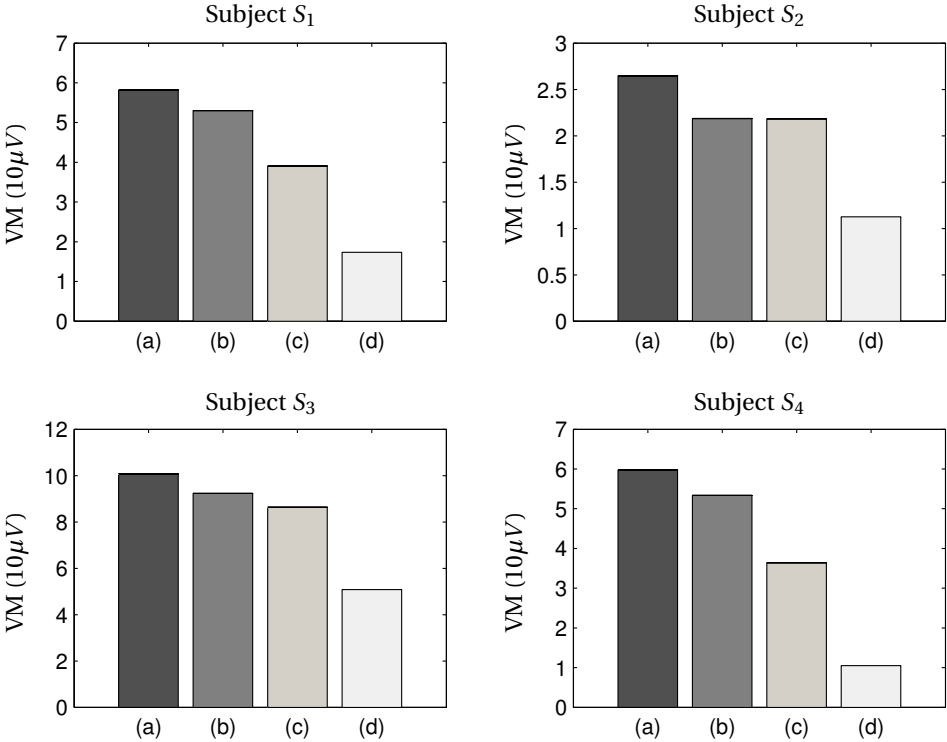


Figure 4.15 – The RMS of the processed EMG signals in the four states. (a) human exoskeleton impedance state (i.e., $Z_h + Z_e$). (b) human joint impedance state (i.e., Z_h). (c) exoskeleton impedance compensation state (i.e., $Z_d = Z_h$). (d) human impedance compensation state (i.e., $Z_d = 0.5Z_h$).

4.6. Experiments of Knee Joint Flexion/Extension Movements

Subjects	Z_h	$Z_h + Z_e$	$Z_d = Z_h$	$Z_d = 0.5Z_h$
S_1	100%	109.8%	73.7%	32.8%
S_2	100%	121.1%	99.8%	51.5%
S_3	100%	109.1%	93.6%	55.0%
S_4	100%	112.0%	68.2%	19.7%
Average	100%	113.0 %	83.8%	39.7%
Std		$\pm 5.5 \%$	$\pm 15.2\%$	$\pm 16.5\%$

Table 4.4 – Comparison of the RMS of the EMG signals measured in the four states

States	0.25 Hz	0.8 Hz
$K_d = 0.2\alpha_1\tau_{g,h}$	$54.02 \pm 15.71 \%$	- - -
$B_d = 0.1B_h$	$86.40 \pm 20\%$	$57.5 \pm 26.33\%$
$J_d = 0.5J_h$	$84.55 \pm 14.4 \%$	$62.32 \pm 26.45 \%$

Table 4.5 – Average reduction ratios of the RMS of EMG signals during inertia, damping and stiffness compensation

Figure 4.15 shows the RMS of the EMG signals of each subject. We observe that all subjects' EMG signal amplitudes (i.e., joint torques) increased after wearing the exoskeleton ($Z_h + Z_e$), compared with the amplitudes obtained when the subjects are not wearing the exoskeleton (Z_h). The average increase ratio is $13 \pm 5.5\%$ [see Table 4.4]. With the power assistance of the AIC, $Z_d = Z_h$, the subjects' EMG signals can be reduced to the same or slightly smaller levels than those observed during the human joint impedance state. These experiments show the same result as that predicted by the simulation (Section 4.4.3). Indeed, it can be stated that the human effort required to perform the same knee joint movement is reduced to the level of the state without wearing the exoskeleton. Moreover, all subjects' EMG signals can be significantly reduced ($60.3 \pm 16.5\%$) when a smaller desired impedance ($Z_d = 0.5Z_h$) is imposed. Table 4.4 shows the ratios of the changes in the EMG signals' RMS under the human exoskeleton impedance ($Z_h + Z_e$), the exoskeleton impedance compensation ($Z_d = Z_h$) and the human joint impedance compensation states ($Z_d = 0.5Z_h$) relative to the values obtained when the subjects are not wearing the exoskeleton (Z_h).

To verify the AIC's ability to compensate the original inertia, damping and stiffness of the human joint impedance, the human joint impedance state (i.e., $Z_d = Z_h$) is chosen as a baseline state. During the experiments, the inertia, damping and stiffness of the impedance model are reduced by 50%, 90% and 80%, respectively, from the baseline state (i.e., $J_d = 0.5J_h$, $B_d = 0.1B_h$ and $K_d = 0.2\alpha_1\tau_{g,h}$). Note that during each experiment, only one impedance parameter value is reduced; the other two values are kept the same as those of the baseline state. Here, a relatively high reduction ratio (0.5) is used for the inertia reduction because small desired inertias easily cause vibration or instability of the whole human-in-loop control

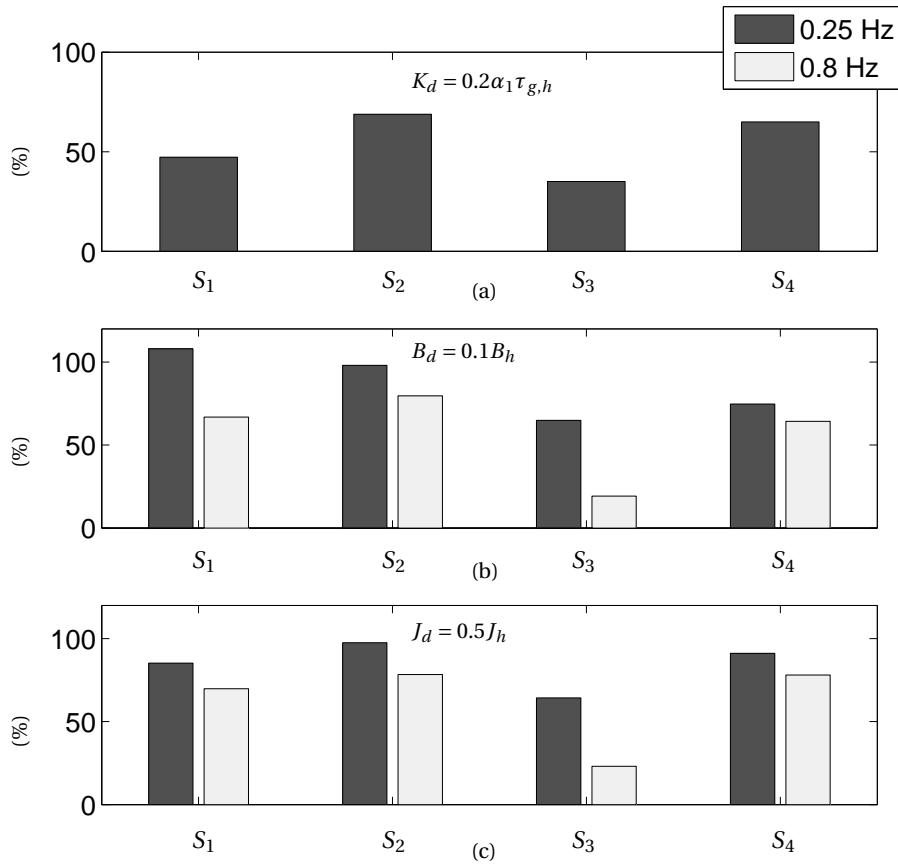


Figure 4.16 – The reduction ratios of the RMS of the EMG signals during inertia, damping and stiffness compensation compared to the baseline state $Z_d(J_h, B_h, \alpha_1\tau_{g,h})$. (a) $Z_d(J_h, B_h, 0.2\alpha_1\tau_{g,h})$; (b) $Z_d(J_h, 0.1B_h, \alpha_1\tau_{g,h})$; (c) $Z_d(0.5J_h, B_h, \alpha_1\tau_{g,h})$.

system (Figure 4.3).

Figure 4.16 shows the reduction ratios of the EMG signals' RMS during inertia, damping and stiffness compensation compared to the baseline state. For low-frequency (i.e., 0.25 Hz) joint movements, the EMG signal levels of all subjects are efficiently reduced ($54.02 \pm 15.71\%$) by stiffness compensation (see Figure 4.16(a)), whereas the reduction in the EMG signals during damping and inertia compensation is not significant ($86.40 \pm 20\%$, $84.55 \pm 14.4\%$) [see Figure 4.16(b), Figure 4.16(c)]. In contrast, a relatively high reduction in the EMG signal levels ($57.5 \pm 26.33\%$, $62.32 \pm 26.45\%$) can be observed during damping and inertia compensation when the subjects swing their legs with a high frequency (0.8 Hz) [see Figure 4.16(b), Figure 4.16(c)]. These experimental results fully match the hypothesis considered in the experimental protocol section. The average reduction ratios of the RMS of the EMG signals during stiffness, damping and inertia compensation are shown in Table 4.5.

During the experiments, the EMG signals of the biceps femoris are measured to monitor the co-contraction of the muscles. The experimental results show that there is no noticeable increase in muscle co-contraction during impedance reduction. In contrast, the EMG signals of the biceps femoris show a slight increase during the knee joint extension movements when the desired impedance is smaller than the original human joint impedance. At the same time, the EMG signals of the vastus medialis are reduced to a relatively small level. This means that the subjects produced an additional torque to stop the joint movement.

Regarding the stability and safety of the proposed method, the experimental results show that a relatively small desired inertia easily results in instability of the whole human-in-loop control system. It should be noted that small desired inertia may cause large changes in the velocity of the movement. During the design of the system, the main frequency range of human movement should be taken into account, and the relatively small desired inertia should be carefully adjusted to guarantee safety. On the other hand, all subjects felt that it is more comfortable and easier to track the reference trajectories when the human inertia is partially compensated.

4.7 Simulations and Experiments of Sit-to-Stand Movements

The experiments are implemented using the E-ROWA exoskeleton. The subject wearing the exoskeleton was asked to perform STS movements without the upper limbs' assistance, as shown in Figure 4.17. The EMG signals of the muscles from both knee extensor groups, the vastus lateralis, are recorded to evaluate the effectiveness of the AIC. The raw EMG signals are measured using two EMG sensors (Delsys, USA) that were placed on both legs. The measured EMG signals are subsequently processed using the following steps: high-pass filtering at 30 Hz using a fourth-order Butterworth filter; elimination of the measurement noise; full-wave rectification; low-pass filtering at 10 Hz using a fourth-order Butterworth filter; and normalization [64].

4.7.1 Parametric Identification

The experiments were conducted with a healthy subject (Sex: male; Age: 28; Weight: 73 kg; Height: 170 cm). The human parameters were identified based on the weight and height of the wearer using the regression method proposed in [104]. In terms of the exoskeleton parameters, the masses of the shank, thigh and upper part can be estimated from CAD data, while the inertia, I_{ei} , damping (viscous friction), B_{ei} , and coefficient distribution of the center of gravity, k_{ei} , of each part (shank, thigh and HAT) must be identified. During the identification procedure, the passive pendulum test method is used. The lower part of the E-ROWA is hanged on a shelf, so it could be considered a 3-DoF passive pendulum model. Considering that there is no actuator at the ankle joint of the E-ROWA, the shank parameters cannot be identified using this method. Hence, these parameters were identified separately using a 1-DoF passive pendulum test (i.e., the shank part is considered as the pendulum model, while the upper part of the exoskeleton is hung). Note that the parameters of the three parts (shank, thigh and HAT) are identified separately. During the parametric identification of each part, the remaining joints were locked. For each part, the identification process is divided into two steps: first, five different static forces are provided by the actuator, and then, a passive pendulum test is implemented. According to the system model (4.2), the coefficient distribution of the center of gravity, k_{ei} , of each part can be measured during the first step, while the inertia, I_{ei} , and damping, B_{ei} , can be identified during the second step. The least squares optimization algorithm is used to process the measured data. The identified parameters of the human body as well as the exoskeleton frames are shown in Table 4.6. Note that the viscous frictions of the exoskeleton joints are very small, so they can be neglected, as discussed in Section 4.2.2.



Figure 4.17 – The STS transfer task for experimental evaluation with the assistance of the E-ROWA exoskeleton.

4.7. Simulations and Experiments of Sit-to-Stand Movements

Parameters	Values
l_1, l_2, l_3	0.4062, 0.3951, 0.7950 (m)
m_{h1}, m_{h2}, m_{h3}	6.3218, 20.6736, 44.1212 (kg)
k_{h1}, k_{h2}, k_{h3}	0.5541, 0.5905, 0.4093
I_{h1}, I_{h2}, I_{h3}	0.0678, 0.3494, 1.8475 ($kg \cdot m^2$)
m_{e1}, m_{e2}, m_{e3}	1.8700, 4.5000, 8.1900 (kg)
k_{e1}, k_{e2}, k_{e3}	0.6824, 0.3538, 0.2119
I_{e1}, I_{e2}, I_{e3}	0.0182, 0.0389, 0.1417 ($kg \cdot m^2$)
B_{e1}, B_{e2}, B_{e3}	0.000, 0.0524, 0.0758 ($Nm \cdot s \cdot rad^{-1}$)

Table 4.6 – Identified system's parameters

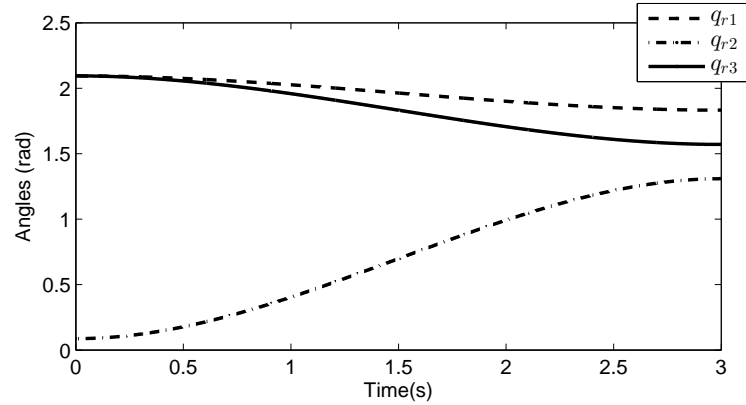


Figure 4.18 – The reference trajectory of the whole system.

4.7.2 Simulation Study

To verify the effectiveness and robustness of the AIC, a simulation study is performed. Note that the human controller is also included in the whole system, as shown in Figure 4.3. To simulate the human brain and muscles, a PID controller is used [102]. Additionally, a direct method is used to replace the GRF to detect the "Seat-Off" time, as follows:

$$\beta_F = \frac{(y_2 - h_{so})^2}{(y_{2,0} - h_{so})^2}, \quad y_2 = l_1 \sin(\theta_1) + l_2 \sin(\theta_2) \quad (4.62)$$

where h_{so} is a given height. y_2 represents the position of the hip joint, while $y_{2,0}$ shows the position of the hip joint in the sitting position.

A given reference STS trajectory is shown in Figure 4.18. The Human-EXO system is controlled using a PID under the AIC controller. To assess the impact of the impedance parameter on the efficiency of the proposed AIC, five simulations were performed with different desired values (i.e., $\lambda_h = \lambda_k = 1, 0.8, 0.6, 0.4, 0.2$). The required human torques ($\tau_{h,h}, \tau_{h,k}, \tau_{h,a}$, the output of the PID controller), as shown in Figure 4.19, show clear decreases with the reduction of the

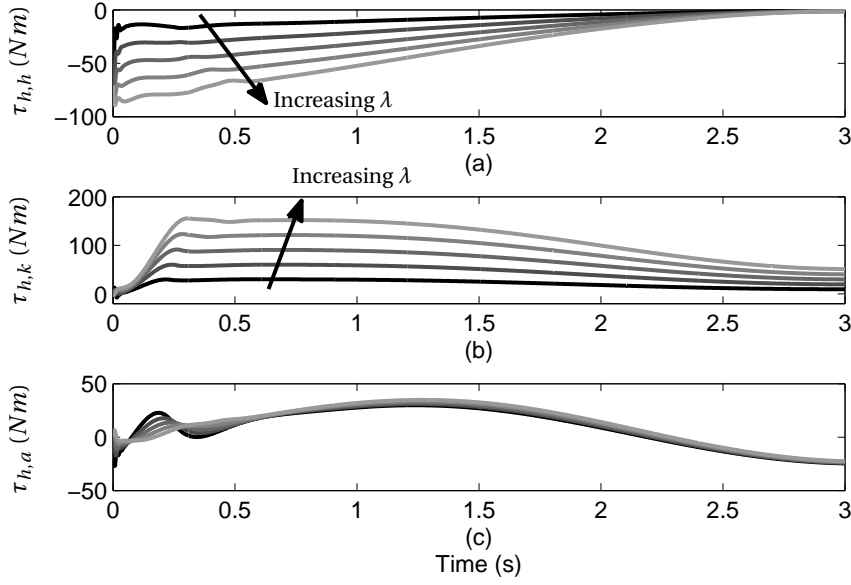


Figure 4.19 – Human torques with different λ ($\lambda_h = \lambda_k = \lambda = 1, 0.8, 0.6, 0.4, 0.2$). (a) the human hip-joint torque. (b) the human knee-joint torque; (c) the human ankle-joint torque.

desired impedance. In other words, the required human torques for achieving similar STS movements can be reduced to a desired level by designing an appropriate desired impedance model.

To verify the robustness properties shown in Section 4.5.5, a given modeling uncertainty is added to the Human-EXO model as follows: $\Delta \mathbf{M}(\mathbf{q}) = \alpha \mathbf{M}(\mathbf{q})$, $\Delta \mathbf{C}(\mathbf{q}, \dot{\mathbf{q}}) = \alpha \mathbf{C}(\mathbf{q}, \dot{\mathbf{q}})$, $\Delta G(\mathbf{q}) = \alpha G(\mathbf{q})$, $\Delta \mathbf{J}_F^T F = \alpha \mathbf{J}_F^T F$. Here, α is a constant, $\alpha = -0.286$. Three simulations were performed with different desired impedance parameters ($\lambda_h = \lambda_k = 0.5, 0.4, 0.28$). According to the stability condition (4.26), the AIC closed loop system becomes unstable if λ_h and λ_k are smaller than 0.286. Figure 4.20 shows the assistance torques provided by the exoskeleton, indicating clearly that if λ_h and λ_k are higher than 0.286, the system is stable, while instability is reached immediately when λ_h and λ_k become lower than 0.286. As a consequence, the desired impedance model (4.9) should be designed based on the modeling accuracy.

4.7.3 Preliminary Experiments

The main goal of the AIC is to reduce the required human torque for achieving a successful STS movement. First, a comparison experiment was carried out to evaluate the estimated human torque obtained using the HJTO. The subject was asked to carry out three STS movements (at a normal speed) without the exoskeleton's support. The joint angles are shown in Figure 4.21(a). It can be observed that the estimated human torque, $\hat{\tau}_k$, shows a very similar curve to the processed EMG signals *during the STS movement* (Figure 4.21(a)). Second, the subject was asked to perform five STS movements (at a normal speed) with the exoskeleton's

4.7. Simulations and Experiments of Sit-to-Stand Movements

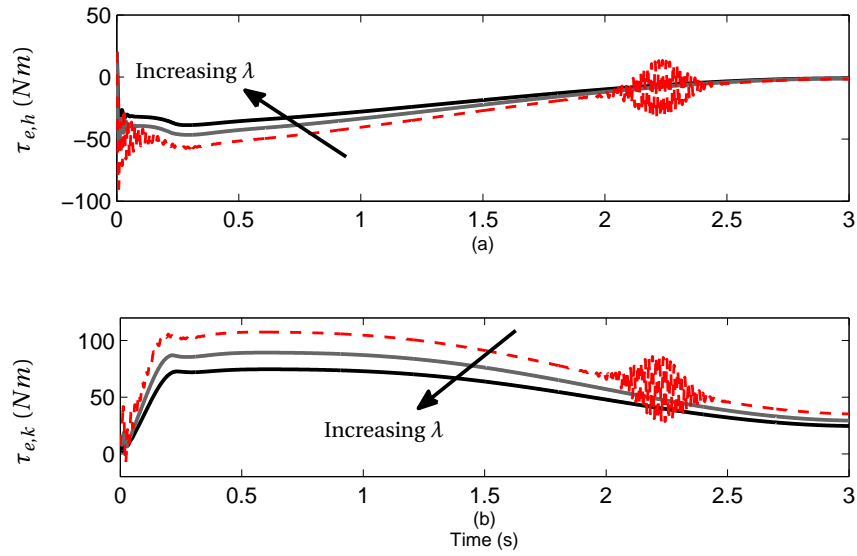


Figure 4.20 – Evaluation of the robust limitations ($\lambda = \lambda_h = \lambda_k = 0.5, 0.4, 0.28$ and $\alpha = -0.286$). (a) the assistive torque on the hip joint; (b) the assistive torque on the knee joint.

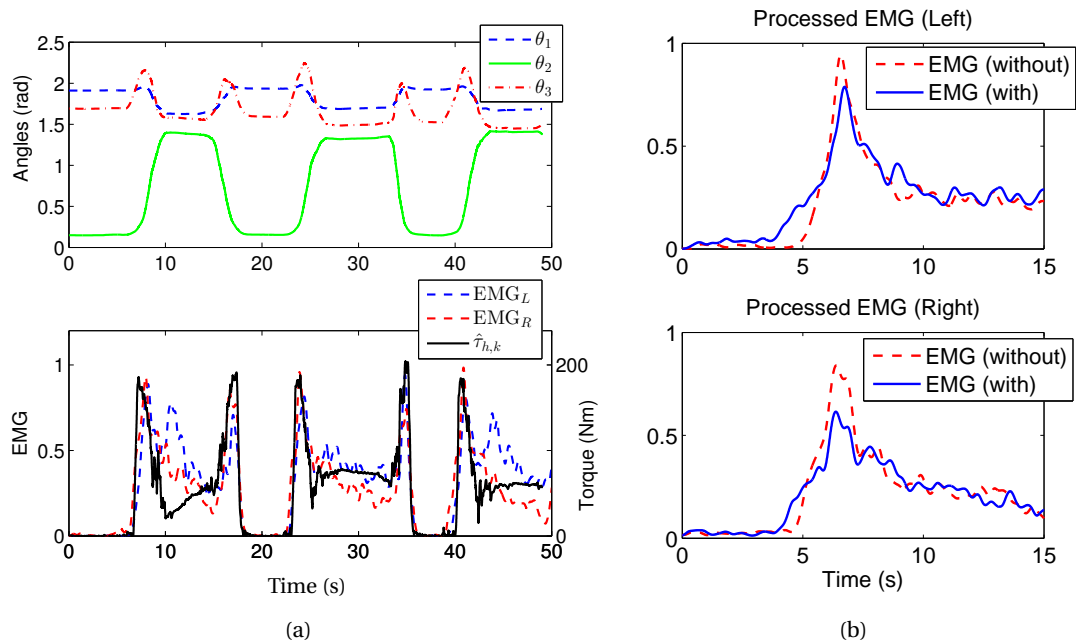


Figure 4.21 – Evaluation of the effectiveness of the AIC using EMG activities. (a) comparison of the estimated human knee torque, $\hat{\tau}_{h,k}$, between the EMG activities of the *Vastus Lateralis* during three STS movements (Standing up \rightarrow sitting down \rightarrow standing up \rightarrow sitting down \rightarrow standing up). (b) comparison of the EMG activities of the *Vastus Lateralis* during the STS movement with and without exoskeleton's assistance.

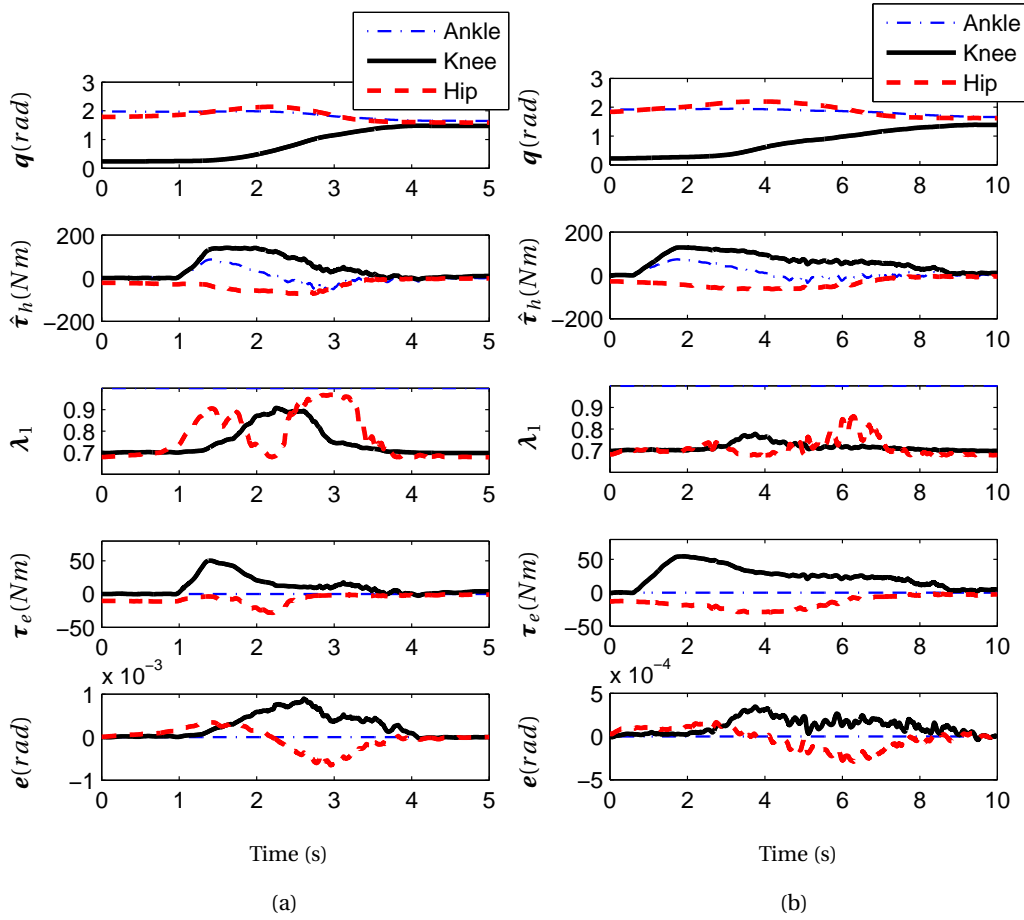


Figure 4.22 – Effectiveness of the AIC with two different standing up speeds. (a) standing up with normal speed. (b) standing up with low speed.

assistance ($\lambda_h = \lambda_k = 0.8$). Figure 4.21(b) shows two groups of EMG signals with and without the exoskeleton's assistance. It can be observed that the maximum value of the EMG is reduced when the wearer is assisted by the exoskeleton. The average reduction percentage of the five groups is approximately 12% for a healthy subject.

Finally, the "assist-as-needed" control strategy is evaluated. The subject was asked to perform the STS movement at two different speeds: a normal speed and a lower speed. The lower-speed STS movement is used to simulate the wearer who has a lack of muscular strength. The joint angles (q), estimated human joint torques ($\hat{\tau}_h$), assistance ratio (λ_1), output torques of the exoskeleton (τ_e) and tracking error (e), are shown in Figure 4.22. It can be observed that the exoskeleton provides a relatively high power assistance (see Figure 4.22(a)) to the wearer during the whole STS movement when the wearer's STS speed is relatively low, while a short and low power assist (see Figure 4.22(b)) is provided for a normal STS speed movement. The tracking error of controller is bounded in a very small range ($\leq 10^{-3}$ rad).

4.8 Conclusion

Based on the proposed active impedance control structure, the original impedance of the human exoskeleton system can be adapted to a desired level. If the desired impedance is smaller than the human limb impedance, active impedance assistance can be obtained from the exoskeleton. Thus, the corresponding human effort needed to perform the same movements can be reduced with the exoskeleton's power assistance. The proposed structure of the system model used in this study, including the torque observer, the sliding mode controller and the desired impedance mode, can be easily used for controlling single-joint and multi-joint human exoskeleton systems (i.e., *Case Study I*: knee joint flexion/extension movements and *Case Study II*: STS movements).

From the wearer's point of view, the proposed method is also a human-centered intention based assistive strategy (i.e., no reference trajectory is required). It can be widely used to assist the wearer in performing various activities of daily living, such as walking, sit-to-stand, and stair ascent/descent. In terms of the human exoskeleton model needed to apply the proposed impedance reduction control structure, the parametric identification method proposed in this chapter can be used. Additionally, the impedance parameters of each joint can be estimated using similar identification methods [130], whereas the human limb kinetic parameters (e.g., inertia and gravity) can be estimated using regression methods [104, 131]). In this chapter, note that the identified human shank parameters are similar to those estimated using the methods provided by [104].

It should be noted that it is sometimes necessary to separately compensate the inertia, damping and stiffness of human joints during daily living activities such as walking. For example, the force of gravity on the lower limb is usually used by the wearer to swing the leg during the early period of the swing phase. Hence, the ability to compensate a single part of the joint impedance is also important. Many existing impedance reduction methods effectively lower the whole impedance magnitude of human-interactive robot systems (e.g., [132]) or augment the human muscular torque (e.g., [102]). However, few of them are able to increase/decrease a single part of the impedance (i.e., the inertia, damping or stiffness) based on a generalized control structure. Using the proposed AIC structure, the inertia, damping and stiffness of the original impedance of the human-exoskeleton system can be adjusted separately. A primary advantage of the proposed method is that it is able to provide different impedance assistances according to the gait mode and phase. For example, in [88], authors proposed a control approach to facilitate the recovery of walking following stroke by separately providing gravity compensation, joint stiffness and damping reinforcement according to a gait phase state machine.

During the experiments of case study I, the effectiveness of the proposed method was evaluated by assisting four healthy subjects as they performed flexion/extension movements in a sitting position. To assess the level of the human knee joint torque, the RMS of the processed EMG signals during each shank swing movement was chosen as a metric. The correlation

between the change in the human joint torque and the RMS of the EMG signals was verified. In the experiments, four states were defined to show that the proposed method can mask the impedance of the exoskeleton and reduce the human effort to the same or a lower level than that required without the exoskeleton. Satisfactory results were obtained during the experiments. With a desired impedance equal to half the original human joint impedance, the RMS of the EMG signal can be reduced by approximately 60%. The ability of the proposed method to separately adjust the inertia, damping and stiffness was also demonstrated using experiments.

During the experiments of case study II, the proposed method is used to assist dependent people in performing safe sit-to-stand movement. The potential users are supposed to have a certain lower limb motion ability, but not sufficient for a successful STS movement. In this case, the active impedance assistance of the exoskeleton can reduce the mechanical impedance of the human-exoskeleton system to a level lower than the wearer's motor ability. Additionally, a time-varying desired impedance model is proposed based on the wearer's motor ability. The effectiveness of the proposed methods was evaluated by simulations and experiments. The experimental results show that the proposed active impedance approach can efficiently estimate the human joint torques, reduce the human-exoskeleton impedance, and provide appropriate power support to the wearer.

The main advantages of the proposed control strategy over the existing ones are as follows:

- i) Only the joint angle information is required for the implementation of the proposed structure. No additional EMG sensors or torque/force sensors are needed.
- ii) The proposed AIC was designed following a generalized way. It can easily be used with different exoskeletons, and to assist various daily living activities.
- iii) A relatively low impedance can be achieved using the desired impedance model. When traditional impedance compensation methods based on torque sensors are used, the impedance reduction is usually limited due to the stability problem caused by the sensor non-collocation [113].

Consider that the proposed AIC control is a model-based control strategy, the system performance or stability are relatively sensitive to the model accuracy as discussed in Section 4.4.4 and Section 4.5.5. Hence, accurate parameter identification methods are required, particularly for multi-joint systems. In this chapter, the parameters of the multi-joint exoskeleton E-ROWA was estimated based on the passive pendulum test, in which the test frequency was limited in a relatively small and low range, while the human parameters were estimated using a regression method proposed in [104]. The identified model is not very accurate. However, it can be further improved using some advanced identification methods (e.g., [133, 134]). In this case, we believe that a better performance of the proposed AIC could be obtained.

Summary

In this chapter, a nonlinear impedance reduction control structure of a knee-joint exoskeleton is proposed to reduce human effort by supplying active impedance assistance. The control structure consists of three parts: a nonlinear joint torque observer, a desired impedance model and a sliding mode controller. The proposed strategy adapts the impedance model of the human exoskeleton system to a desired level that is smaller than the original human limb impedance level. From the application point of view, it is convenient to adjust the inertia, damping and stiffness of the resulting impedance based on the proposed structure. In addition, the hardware requirements of the exoskeleton are relatively simple compared with those of existing methods; only joint angle sensors are used. Two cases (i.e., knee joint flexion/extension movement assistance and STS movement assistance) were studied using the proposed AIC structure. Correspondingly, single-joint and multi-joint controllers were designed in detail. Theoretical analyses of the characteristics and robustness with respect to the model uncertainties of the proposed control structure are provided under the two case studies.

5 Gait-mode Based Multi-task Assistive Control Strategy

5.1 Introduction

WALKING is a difficult task for people suffering from muscular impairments and weaknesses. The lack of muscular strength and endurance limits the walking time and may result in walking failure. The walking motion consists of various *modes* according to the ground condition, e.g., level walking, stairs ascent/decent, etc, and the human body shows significantly different kinetic characteristics in different gait modes [57]. In a gait mode, the walking motion can be further distinguished by the ground contact condition, e.g., loading response, initial contact, etc., which are often called the *gait phases*.

In order to assist people with walking difficulties, powered exoskeletons have been developed recently. Due to the complexity of the gait motions, the control algorithms for the exoskeletons should take into account different gait motions. An intuitive method is to utilize different control methods for different gait motions; for this purpose, finite-state control strategies have been proposed [6, 8, 9, 78, 86, 88, 89]. In these approaches, different assistive strategies are selected according to the states (e.g., gait phases, gait modes, etc.) detected by motion detection algorithms. To realize continuous and smooth transitions between different power-assist strategies, the gait motions need to be quickly and accurately detected.

In this chapter, a fast gait mode detection algorithm is proposed to estimate three common daily living activities such as level walking, stair ascent and stair descent. Here, the “fast” means that the transition between gait modes can be detected at the early beginning of a new gait step. Dynamic information such as velocity and position of the wearer’s foot during walking are selected as features. The gait mode transitions can be quickly estimated using the foot velocity (i.e., low latency), and accurately detected based on the foot position (i.e., high detection success rate). Although the foot velocity and position can be estimated using IMUs, long-term accuracy of these measured features cannot be guaranteed in practice, due to the current technical limitations of the IMUs such as drifts [135, 136]. This is also considered as a main reason that limits the application of these dynamic information in currently developed

gait mode detection methods. In this study, to ensure accurate estimation of the features, an update algorithm is proposed by combining a zero-velocity detection method and the use of a human kinematic model. The advantages of these two methods are integrated using a Kalman filter according to the wearer's postures and foot states. Based on the actually estimated dynamic features, a fuzzy logic algorithm is used to estimate the continuous likelihood of each gait mode.

A hybrid power assist strategy of a lower limb exoskeleton (E-ROWA, Figure 5.1) is also developed to provide different assistances for the wearer according to his/her gait modes. Compared to traditional finite-state machine algorithms that switching different strategies according to the changes of the defined states (e.g., gait modes and phases), an alternative method is presented. In the proposed strategy, the assistive torques are directly calculated based on the outputs of all assistive strategies and the likelihoods of the associated gait modes and phases. This can provide smooth assistive torques, and efficiently avoid the sudden changes of the assistive torques.

The potential wearers are assumed to have partial motor ability for achieving a desired swing leg movement (e.g., most elders), since the gait modes are detected according to movements of the wearer's swing leg. The effectiveness of the proposed approaches is evaluated by experiments conducted with three healthy subjects wearing the lower limb exoskeleton E-ROWA. Latency and success rate of gait mode detection are selected as performance criteria. The effectiveness of the gait mode based assistive strategy is evaluated using EMG muscular activities.

5.2 A Wearable Robot for Walking Assistance

5.2.1 E-ROWA

In the study of this chapter, the E-ROWA exoskeleton is used to implement and evaluate our proposed method. In order to measure the relative kinematics of the human body wearing the exoskeleton, a body segment coordination system, B , is built based on the standards of the International Society of Biomechanics (ISB) (see Figure 5.1) [137]. The wearer's hip, knee and ankle joint angles can be measured using the angular sensors embedded in the exoskeleton. As it regards the hardware of the E-ROWA exoskeleton, they have been presented in the General Introduction chapter (i.e., Chapter 1).

5.2.2 Inertial Measurement Units (IMUs)

In addition to the encoder sensors embedded in the exoskeleton E-ROWA, two Inertial Measurement Units (IMUs), Xsens MTi sensor, are mounted on both shoes, as shown in Figure 5.1. Each IMU consists of a 3D accelerometer, a 3D gyroscope and a 3D magnetometer. The rotation matrix of the IMU with respect to the global coordination system, G , can be measured

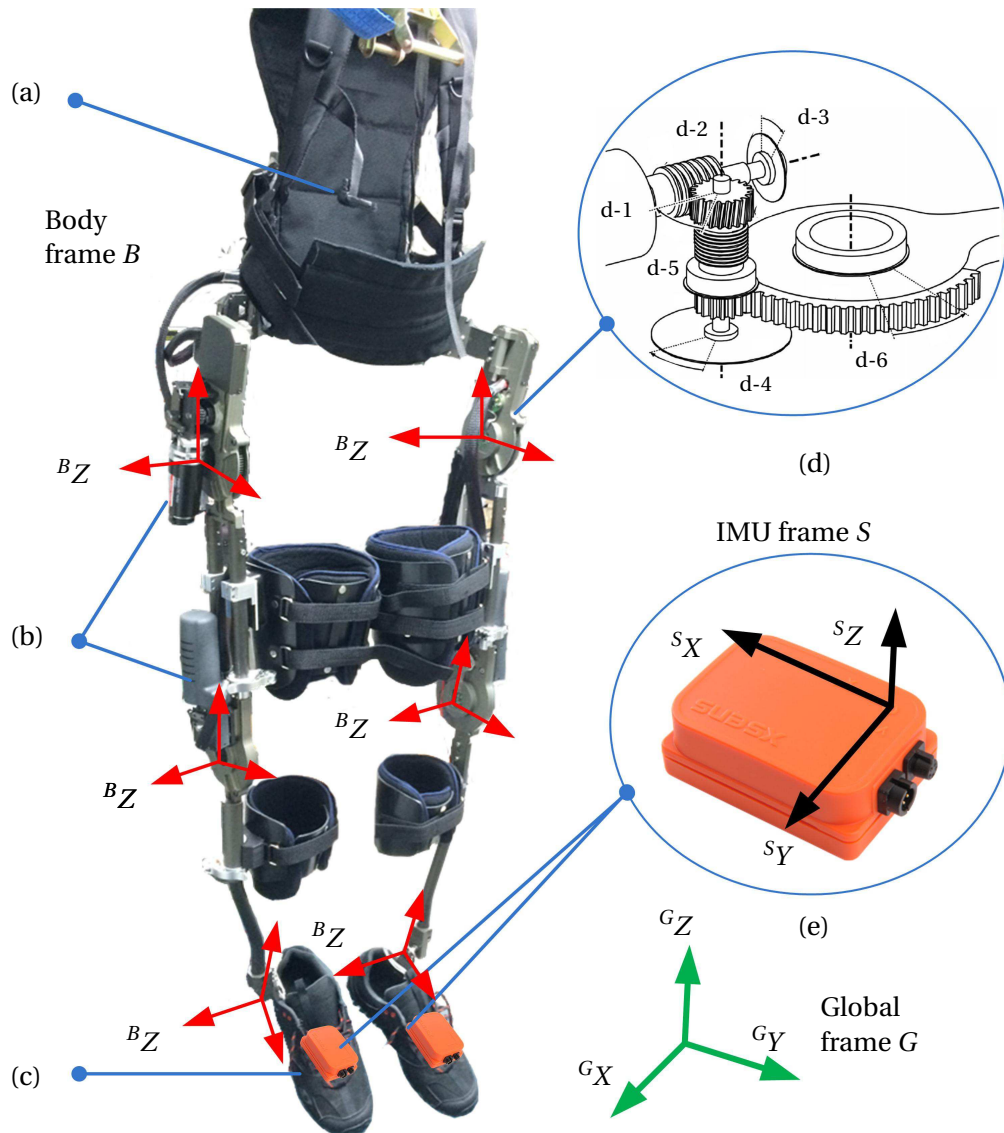


Figure 5.1 – Lower limb exoskeleton E-ROWA. (a) controller and power unit. (b) cRSEA. (c) smart shoe. (d) the structure of the cRSEA (d-1: DC motor, d-2: worm gear and worm wheel, d-3, d-4: angle sensors, d-5: spring, d-6: hip/knee joint) [41]. (e) IMU sensor. In standing position, the body frame B , is designed as follows: origin, center of rotation; X, forward in sagittal plane; Y, up; Z, right in frontal plane. The global frame G , is defined as: X, local magnetic north direction; Y: local magnetic west direction; Z, vertical direction.

based on the measurements of the accelerometer, gyroscope and magnetometer [138]. In this study, the rotation matrix provided by the Xsens MTi sensor is directly used.

The transformation matrix from the sensor frame, S , to the body frame, B , is denoted by:

$${}^B\mathbf{R}_{S,i} = {}^S\mathbf{R}_{B,j}^{-1} = [{}^S\mathbf{X}_{B,j} \ {}^S\mathbf{Y}_{B,j} \ {}^S\mathbf{Z}_{B,j}]^{-1} \in \mathbb{R}^{3 \times 3}, \quad (5.1)$$

where ${}^S\mathbf{X}_{B,j}$, ${}^S\mathbf{Y}_{B,j}$ and ${}^S\mathbf{Z}_{B,j}$ denote the foot frame's unit x-axis, y-axis and z-axis respectively measured by the IMUs. ${}^S\mathbf{R}_{B,j}$ represents the orientation of the foot in the attached sensor's frame, where $j \in \{1, 2\}$ denotes the number the IMU. In order to calculate the transformation matrix ${}^B\mathbf{R}_{S,j}$, a simple calibration procedure is required and is shown in the Appendix B.

5.3 Human Gait Mode Detection

5.3.1 Reference Point

The human gait is divided into two phases: stance and swing. Generally, during the swing phase, humans adjust the posture of their swing legs according to the terrains to prepare the next step. In this study, in order to estimate the human gait modes such as level walking and stair ascent/descent, the relative motions of the swing foot are explored. Calculation of the kinematics of the swing foot requires a reference point, ${}^G\mathbf{O}$, that is set at the stance foot. During the whole stride, the reference point is fixed, and is assumed to be stationary. In this setting, the movement of the swing foot is used to detect the gait mode. The location of the reference point, ${}^G\mathbf{O}$, changes during walking, and is updated for each step. The equations updating the reference point are given as:

$${}^G\mathbf{O}(k) = \begin{cases} \mathbf{p}_l, & \text{for } D_l(k) = 1 \text{ and } D_r(k) = 0 \\ \mathbf{p}_r, & \text{for } D_l(k) = 0 \text{ and } D_r(k) = 1 \\ {}^G\mathbf{O}(k-1), & \text{otherwise,} \end{cases} \quad (5.2)$$

where ${}^G\mathbf{O}(k)$ is the reference point at the k th sampling instance. \mathbf{p}_l and \mathbf{p}_r represent respectively the position of the left and right foot in the global coordination system G . D_l and D_r , $\in \{0, 1\}$, are binary variables that represent the states of the left and right foot respectively. 0 and 1 denote the moving and stationary states respectively.

The period in which the reference point remains unchanged is defined to one reference-point transformation period (RPTP). In order to accurately denote the state of the foot during one RPTP, two foot states are defined: reference and non-reference. The foot whose position is chosen as the reference point is considered as the reference foot while the other foot is the

non-reference one, as follows:

$$O_{foot}(k) = \begin{cases} 0, & \text{for } D_l(k) = 1 \text{ and } D_r(k) = 0 \\ 1, & \text{for } D_l(k) = 0 \text{ and } D_r(k) = 1 \\ O_{foot}(k-1), & \text{otherwise,} \end{cases} \quad (5.3)$$

where $O_{foot}(k)$ represents the reference foot, i.e., $O_{foot}(k) = 0$ and $O_{foot}(k) = 1$ mean that the reference point is at the left and right foot, respectively.

5.3.2 Gait Modes

Three common gait modes of the daily living activities are studied in this chapter, that are Level Walking (LW), Stair Ascent (SA) and Stair Descent (SD). In order to detect these gait modes in real time, features characterizing the gait mode should be extracted at each time step. The movements of the non-reference foot with respect to the reference point are different in the reference frame of the foot B , particularly in terms of horizontal and vertical positions, as well as horizontal and vertical velocities (see Figure 5.2).

In one RPTP, the movement of the non-reference foot is divided into three phases: approaching the reference point (P_1), away from the reference point (P_2) and stopping (P_3). In the "stopping" phase, the absolute horizontal positions, $\hat{\mathbf{p}}_h = \sqrt{\hat{\mathbf{p}}_x^2 + \hat{\mathbf{p}}_z^2}$, of the non-reference foot during level walking are much longer than those during stair ascent/descent (see Figure 5.2(a)); the vertical positions, $\hat{\mathbf{p}}_y$, also show significant differences during the three gait modes (see Figure 5.2(b)). In the "away from the reference point" phase, the horizontal velocities, $\dot{\hat{\mathbf{p}}}_h$ can be used to distinguish the level walking mode from the remaining gait modes (see Figure 5.2(c)), while the stair ascent and stair descent modes can be estimated using the vertical velocity, $\dot{\hat{\mathbf{p}}}_y$ (see Figure 5.2(d)). One should note that the gait modes can be fast detected from the period P_2 . At the same time, a high success rate of the gait mode detection can be obtained with the increase of the foot position, $\hat{\mathbf{p}}_h$ and $\hat{\mathbf{p}}_y$, from period P_2 to period P_3 . Hence, the horizontal/vertical positions ($\hat{\mathbf{p}}_h$, $\hat{\mathbf{p}}_y$) and horizontal/vertical velocities ($\dot{\hat{\mathbf{p}}}_h$, $\dot{\hat{\mathbf{p}}}_y$) of the non-reference foot with respect to the reference point are selected as the main features for gait mode detection.

5.3.3 Gait Mode Detection

According to its definition in Section 5.3.2, the feature $\hat{\mathbf{p}}$ can be calculated by (5.1)–(5.3):

$$\hat{\mathbf{p}}(k) = {}^B R_S {}^G R_S^T [\mathbf{p}_r(k) + O_{foot}(k)[\mathbf{p}_l(k) - \mathbf{p}_r(k)] - {}^G \mathbf{O}(k)], \quad (5.4)$$

where ${}^G R_S$ shows the rotation matrix provided by the IMU placed at the reference foot during the stationary state.

Fast and accurate gait mode detection requires accurate measurement of the features, $\hat{\mathbf{p}}_h$, $\hat{\mathbf{p}}_y$,

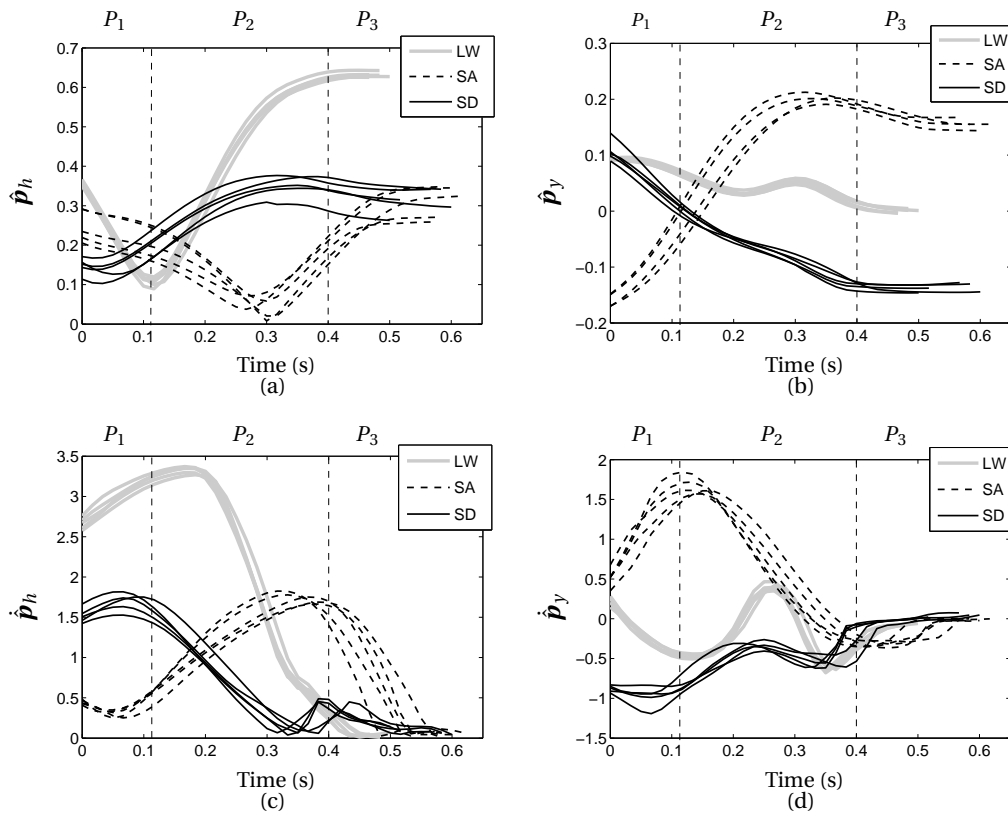


Figure 5.2 – The main features of different gait modes (level walking (LW), stair ascent (SA) and stair descent (SD)) in one RTP: (a), (b), (c) and (d) show respectively the absolute horizontal positions (\hat{p}_h), the vertical positions (\hat{p}_y), the horizontal and vertical velocities (\hat{p}_h , \hat{p}_y) of the non-reference foot during five gait cycles. P_1 , P_2 and P_3 denote three phases respectively: approaching the reference point, away from the reference point and stopping.

$\dot{\mathbf{p}}_h$ and $\dot{\mathbf{p}}_y$, during the daily living walking motions. Although the position (i.e., $\mathbf{p}_l, \mathbf{p}_r$ in (5.4)) and velocity (i.e., $\mathbf{v}_l = \dot{\mathbf{p}}_l$ and $\mathbf{v}_r = \dot{\mathbf{p}}_r$) of the foot can be calculated by integrating the foot's acceleration twice and once respectively, their accurate values cannot be preserved more than few seconds [136, 139]. Indeed, the position and velocity errors increase with time, even for a tiny sensor drift in the orientation or acceleration of the IMU. Hence, some correction methods should be used to guarantee accurate position and velocity measurements of each foot when using IMUs.

■ Velocity Update

Identifying the stationary state is critical for the reference point update method in (5.2). At the same time, during the stationary state, the velocity of the foot is assumed to be equal to zero, while the measured foot velocity may not be exactly equal to zero when integrating the acceleration. Hence, the stationary state (i.e., zero-velocity instant) can be used to correct the foot velocity obtained by integrating the acceleration [136].

To detect the zero-velocity instant, ground reaction forces are usually used during level walking [81, 139]. Due to the fact that various foot contact conditions may occur during different gait modes when the foot velocity is equal to zero, more complex situations should be considered for using the ground reaction forces. On the other hand, some detection methods have been proposed using the measured acceleration or angular velocity of foot [135]. Considering the fact that the change of the angular velocity of the swing foot is not significant during the stair ascent/descent, only the acceleration is taken into account. During the stationary state, the total acceleration of the foot is relatively small, so a threshold can be used to distinguish the stationary state from the moving state. However, the detection results are easily influenced by the small fluctuations of the measured acceleration of the foot. To overcome this problem, an improved zero-velocity detector is proposed by integrating the measured acceleration and its variance, as follows:

$$D(k) = \begin{cases} 1, & \text{for } \frac{1}{N} \sum_{\lambda=k-N}^k \check{\mathbf{a}}^T(\lambda) \mathbf{P}_a \check{\mathbf{a}}(\lambda) < D_{th}, \\ 0, & \text{otherwise,} \end{cases} \quad (5.5)$$

where $\check{\mathbf{a}} = {}^G\mathbf{R}_S \mathbf{a}_{imu} - \mathbf{g} \in \mathbb{R}^{3 \times 1}$, which is the net accelerations in the X , Y , and Z axes of the global reference frame G . $\mathbf{a}_{imu} \in \mathbb{R}^{3 \times 1}$ represents the measured accelerations using the IMUs and $\mathbf{g} = [0 \ 0 \ -9.8]^T$ is the gravitational acceleration vector. $\mathbf{P}_a \in \mathbb{R}^{3 \times 3}$ is the associated diagonal covariance matrix of the accelerations. N denotes the width of the detection time horizon. D_{th} is a threshold that can be set according to the variance of the accelerations in a stationary case.

The modified measured foot velocity is then obtained by:

$$\check{\mathbf{v}}(k) = (1 - D(k)) [\check{\mathbf{v}}(k-1) + \check{\mathbf{a}}(k)T], \quad (5.6)$$

where T represents the sampling period.

■ Position Update

By integrating the measured foot velocity, $\check{\mathbf{v}}$, the foot position can be also calculated. Since the features for gait mode detection are the relative movements between the two feet (5.4), a position error occurs, and increases with time even if there is a small error between the measured velocities of two feet. To correct this relative position error, a kinematic model of the lower limbs is used. Based on the body coordination system B , the position of each joint or the end point of each segment with respect to the stance foot can be calculated as follows:

$${}^0T_n = \prod_{i=0}^n {}^iT_{i+1}, \quad (5.7)$$

where n represents the sequence number of the segment from the reference point. ${}^iT_{i+1}$ shows the transformation matrix that is given by:

$${}^iT_{i+1} = \begin{bmatrix} {}^iR_{i+1} & {}^iR_{i+1} {}^iL_{i+1} \\ \mathbf{0}_{1 \times 3} & 1 \end{bmatrix} \in \mathbb{R}^{4 \times 4}, \quad (5.8)$$

where ${}^iR_{i+1} \in \mathbb{R}^{3 \times 3}$ denotes the rotation matrix describing frame $i + 1$ relative to frame i . ${}^iL_{i+1} \in \mathbb{R}^{3 \times 1}$ represents the position vector from joint $i + 1$ to joint j .

From (5.1), (5.2) and (5.8), the foot position can be calculated by:

$$\check{\mathbf{p}} = {}^G R_S {}^S R_B [{}^0T_{n,14} {}^0T_{n,24} {}^0T_{n,34}]^T + {}^G \mathbf{O}, \quad (5.9)$$

where ${}^0T_{n,rc}$ denotes the element of the matrix 0T_n at the r th row and c th column.

It should be noted that the rotation angle of the adduction/abduction and rotation movements of the hip joint are not taken into account. These angles are almost zero during walking movement in the sagittal plane. However, a certain measurement error occurs when the wearer is turning. Additionally, the measurement accuracy using the kinematic model also depends on the accuracy of the measured segment lengths.

5.3.4 Sensor Fusion Using Kalman Filter

In order to integrate the advantages of the proposed methods and eliminate their disadvantages (as discussed in Section 5.3.3), a Kalman filter is used to ensure sensors fusion of the foot's position and velocity. The Kalman filter is designed in the following.

Define the state vector for establishing a Kalman filtering system as:

$$\mathbf{X} = \begin{bmatrix} \mathbf{p} & \mathbf{v} & \mathbf{a} & \mathbf{e}_a \end{bmatrix}^T \in \mathbb{R}^{12 \times 1}, \quad (5.10)$$

where \mathbf{p} , \mathbf{v} and \mathbf{a} represent respectively the 3D positions, velocities and accelerations of the foot in the global coordination frame G . \mathbf{e}_a denotes the acceleration drifts. The state space equation of the state vector in (5.10) is:

$$\mathbf{X}(k+1) = \mathbf{A}\mathbf{X}(k) + \boldsymbol{\omega}, \quad (5.11)$$

where

$$\mathbf{A} = \begin{bmatrix} \mathbf{I}_3 & T\mathbf{I}_3 & 0.5T^2\mathbf{I}_3 & -0.5T^2\mathbf{I}_3 \\ \mathbf{0}_3 & \mathbf{I}_3 & T\mathbf{I}_3 & -T\mathbf{I}_3 \\ \mathbf{0}_3 & \mathbf{0}_3 & \mathbf{I}_3 & \mathbf{0}_3 \\ \mathbf{0}_3 & \mathbf{0}_3 & \mathbf{0}_3 & \mathbf{I}_3 \end{bmatrix} \in \mathbb{R}^{12 \times 12}, \quad (5.12)$$

where \mathbf{A} represents the discrete-time state-transition-matrix, and $\boldsymbol{\omega}$, the process noise with variance $\mathbf{Q}(k)$. \mathbf{I}_3 and $\mathbf{0}_3$ represent identity and zero matrices, respectively.

The observation state of the Kalman filter is

$$\mathbf{Z}(k) = \check{\mathbf{X}}(k+1) = \mathbf{H}(k)\mathbf{X}(k) + \mathbf{v} \quad (5.13)$$

where $\mathbf{H}(k)$ denotes the measurement matrix. \mathbf{v} represents the measurement error that is assumed to be white noise and with normal probability distribution, $p(\mathbf{v}) \sim N(0, \mathbf{R}(k))$.

As discussed in Section 5.3.3, the measured velocity is not reliable during the zero-velocity instant (i.e., $D(k) = 1$ as in (5.5)), and is corrected using zero velocity. At the same time, during the zero velocity state, the measured acceleration $\check{\mathbf{a}}$ is considered as the bias (i.e., $\check{\mathbf{e}}_a = \check{\mathbf{a}}$). Hence, the $\mathbf{H}(k)$ is given by:

$$\mathbf{H} = \text{diag}(\mathbf{I}_3, D(k)\mathbf{I}_3, \mathbf{I}_3, D(k)\mathbf{I}_3) \in \mathbb{R}^{12 \times 12}. \quad (5.14)$$

The measurement noise covariance, $\mathbf{R}(k)$, can be expressed as follows:

$$\mathbf{R}(k) = \text{diag}(R_p(k)\mathbf{I}_3, R_v(k)\mathbf{I}_3, R_a\mathbf{I}_3, R_e\mathbf{I}_3) \in \mathbb{R}^{12 \times 12} \quad (5.15)$$

where R_a and R_e are constants that represent the measurement noise covariances of the acceleration and its bias respectively. $R_p(k)$ and $R_v(k)$ represent the measurement noise covariance of the position and velocity, respectively.

To avoid sudden change of the Kalman filter output due to the zero-velocity update, the

measurement noise covariance of the foot's velocity during the stationary state is designed by:

$$R_v(k) = D(k)\alpha_v\sqrt{\check{\mathbf{a}}_x^2(k) + \check{\mathbf{a}}_y^2(k) + \check{\mathbf{a}}_z^2(k)} + r_v \quad (5.16)$$

where α_v and r_v denote two positive constants respectively.

One should notice that R_v decreases with the reduction of the amplitude of the measured acceleration during the stationary state (i.e., $D(k) = 1$), and is set to be r_v when the foot is in real stationary state or the moving state (i.e., $D(k) = 0$).

In terms of position measurement, a time-varying measurement noise covariance is also used to integrate the advantages of the acceleration-based and kinematic-model based method, i.e.

$$R_p(k) = \alpha_1|\theta_{h,l}(k) - \theta_{h,r}(k)| + \alpha_2(|\theta_{k,l}(k)| + |\theta_{k,r}(k)|) + \alpha_3(|\theta_{a,l}(k)| + |\theta_{a,r}(k)|) \quad (5.17)$$

where θ_h , θ_k and θ_a represent the angles of the hip, knee and ankle joints respectively, while the subscripts l and r denote left and right leg respectively. Assume that all joint angles in the standing posture are zero. α_1 , α_2 and α_3 are three weight factors. Due to the symmetry of the exoskeleton, the measured foot position shows a relatively high accuracy around the standing posture. The measurement error on swing foot's position, $\check{\mathbf{p}}$, increases with the amplitude of the joint angles.

The estimated state is then calculated as in [140], i.e.

$$\hat{\mathbf{X}}(k+1) = \mathbf{A}\hat{\mathbf{X}}(k) + \mathbf{P}(k)\mathbf{H}^T(k)(\mathbf{H}(k)\mathbf{P}(k)\mathbf{H}^T(k) + \mathbf{R}(k))^{-1}(\mathbf{Z}(k) - \mathbf{H}(k)\mathbf{A}\hat{\mathbf{X}}(k)) \quad (5.18)$$

where $\mathbf{P}(k)$ is the error covariance that is updated using the Joseph form equation:

$$\mathbf{P}(k+1) = (\mathbf{I}_{12} - \mathbf{K}(k)\mathbf{H}(k))\mathbf{P}(k)(\mathbf{I}_{12} - \mathbf{K}(k)\mathbf{H}(k))^T + \mathbf{K}(k)\mathbf{R}(k)\mathbf{K}(k)^T \quad (5.19)$$

where $\mathbf{K}(k)$ denotes the Kalman gain, i.e.

$$\mathbf{K}(k) = \mathbf{P}(k)\mathbf{H}^T(k)(\mathbf{H}(k)\mathbf{P}(k)\mathbf{H}^T(k) + \mathbf{R}(k))^{-1} \quad (5.20)$$

The Kalman filter algorithm introduced in this section is to be applied for each of the left and right legs separately. Based on the aforementioned sensor fusion methods, the modified position and velocity of each foot can be expressed as follows:

$$\mathbf{p} = \begin{bmatrix} \mathbf{p}_l \\ \mathbf{p}_r \end{bmatrix} \quad \text{and} \quad \mathbf{v} = \begin{bmatrix} \dot{\mathbf{p}}_l \\ \dot{\mathbf{p}}_r \end{bmatrix}. \quad (5.21)$$

5.3.5 Fuzzy Logic based Approach for Gait Mode Detection

According to the analysis given in Section 5.3.2, the three gait modes (i.e., level walking, stair ascent/descent) can be detected based on the kinematic features of the non-reference foot such as horizontal position (\hat{p}_h), vertical position (\hat{p}_y), horizontal velocity ($\dot{\hat{p}}_h$) and vertical velocity ($\dot{\hat{p}}_y$). Since different features and varying feature values are used to detect the gait modes in different periods of a RPTP, it is difficult to use a threshold-based method to estimate the gait modes. On the other hand, fuzzy-logic based methods have been efficiently used to identify human states based on accurately extracted multiple features [141–143]. Furthermore, continuous likelihoods of gait modes are required to generate smooth assistive torques of the exoskeleton. This will be illustrated in Section 5.4.3.

A standard Mamdani fuzzy inference system [144] is used. Based on the characteristics of the features (i.e., \hat{p}_h , \hat{p}_y , $\dot{\hat{p}}_h$ and $\dot{\hat{p}}_y$), the Bell-shaped functions are chosen as the membership functions. Each feature is described by three levels: small, middle and large. Consequently, three membership functions are used. The linguistic antecedent variable parameters were chosen based on the kinematic data of the healthy subjects during normal walking (see Figure 5.2). For example, Figure 5.3(a) shows the linguistic variable of the feature, \hat{p}_y . The variables of the remaining features are designed using the same method. Regarding the fuzzy consequent variables, features for three gait modes are all defined with respect to the same terms: small, middle and large. At the same time, same consequent variables are used for three gait modes, as shown in Figure 5.3(b). Table 5.1 shows the fuzzy rules designed from the analysis given in Section 5.3.2. A centroid-based method is used for defuzzification. The outputs of the fuzzy interface, performed at each time step, are three likelihood values of the level walking, stair ascent and stair descent respectively, i.e.

$$\mathbf{U}_m = \begin{bmatrix} u_{lw} & u_{sa} & u_{sd} \end{bmatrix} \in \mathbb{R}^{1 \times 3}, \quad (5.22)$$

where the components, $u_{lw}, u_{sa}, u_{sd} \in [0, 1]$, denote the likelihoods of the three gait modes, i.e., level walking, stair ascent and stair descent, respectively.

The fuzzy rules are divided into two parts: Rules 1-6 are designed to detect the gait mode for the “stopping” period, P_3 , while Rules 8-15 for the “away from the reference point” period, P_2 (see Figure 5.2). Hence, the gait mode can be fast detected at the beginning of each step (i.e., P_2). The success rate of gait mode detection is improved with the increase of the movement amplitude (i.e., P_3). Note that the gait mode is assumed to remain unchanged during period P_1 , due to the fact that we have homogeneous terrain during one step.

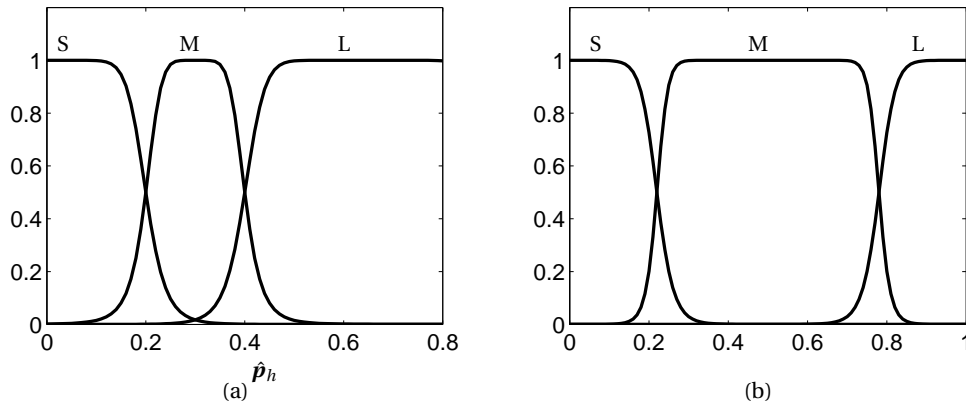


Figure 5.3 – Membership functions (S: Small; M: Middle; L: Large). (a) the linguistic antecedent variables of the horizontal position \hat{p}_h . (b) the linguistic consequent variables of three gait modes.

Rules		\hat{p}_h	\hat{p}_y	$\dot{\hat{p}}_h$	$\dot{\hat{p}}_y$		LW	SA	SD
1		S	M	S	M		L	S	S
2		N/A	L	N/A	M		S	L	S
3	IF	L	M	N/A	N/A	THEN	L	S	S
4		M	S	N/A	N/A		S	S	L
5		L	S	N/A	N/A		M	S	L
6		L	L	N/A	N/A		M	L	S
7		L	M	S	M		L	S	S
8		S	M	L	M		L	S	S
9		M	M	L	M		L	S	S
10		M	M	M	M		L	S	S
11	IF	S	M	M	M	THEN	L	S	S
12		N/A	M	N/A	L		S	L	S
13		S	L	N/A	S		S	S	L
14		S	M	N/A	S		S	S	L
15		M	M	N/A	S		S	S	L

L: Large; M: Middle; S: Small; N/A: Not applied

Table 5.1 – Fuzzy Rules (Rule-I)

5.4 Assistive Torque Control based on Gait Mode Detection

5.4.1 Assistive Strategies According to Gait Modes

Based on the estimated gait mode, a hybrid assistive control strategy is proposed to provide physical support to the wearer's leg by the exoskeleton. The required assistive joint torques are generated according to the lower limb motor function performed by the wear during different walking motions (i.e., gait modes and phases). A main function of the human lower-limb muscles is to support the body's gravity during walking. Additionally, the lower-limb antagonist muscles co-contract in special moments to adjust the joint impedance for achieving some special functions such as "soft" stop (e.g., during the "initial contact" of level walking or stair descent) and maintaining balance (e.g., during the "middle stance" phase of stair ascent). Furthermore, during the swing phase, the wearer's leg should move freely in order to adjust the gait postures. Therefore, four assistive strategies are used in this study: partial gravity compensation (GC), virtual spring (VS) based impedance assistance, virtual damper (VD) based impedance assistance and zero impedance (ZI) assistance. The partial gravity compensation reduces the wearer's efforts during the stance phase and the wearer can freely adjust the movements of the swing leg with zero impedance applied by the exoskeleton. The virtual spring based impedance assistance is used to enforce the joint stiffness and the virtual damper based one is used to reduce the impact effects.

To select appropriate assistances for each gait mode, four gait phases are further defined: early stance (S_1), middle stance (S_2), late stance (S_3) and swing phase (S_4). The middle stance is defined as the phase in which the wearer's shank and thigh are aligned and the shank supposed to be perpendicular to the horizontal plane. The early stance is defined as the phase from the foot initial contact to the middle stance, while the late stance is the phase from the middle stance to the end of the stance phase.

Based on the wearer's gait mode and gait phase, different assistive strategies such as GC, VS, VD and ZI are selected during walking (see Figure 5.4 and Table 5.2). In order to reduce the human efforts, the partial gravity compensation (GC) is used during all stance phases (early stance, middle stance and late stance) of the three gait modes. During the middle stance of level walking, the knee joint should perform a high stiffness to prevent the flexion/extension movements. Likewise, the hip and knee joints show the same characteristics during the middle stance and late stance of stair ascent. Thus, the virtual spring is used to enforce the joints' stiffness at the equilibrium points, and prevent the instability during these phases. In the meantime, the virtual damper is selected to help the joint achieving the "soft" impact with the ground during the early stance of level walking and stair descent. During the swing phase, a zero impedance (ZI) control strategy is used.

The assistive torques related to the four strategies are calculated using the following methods.

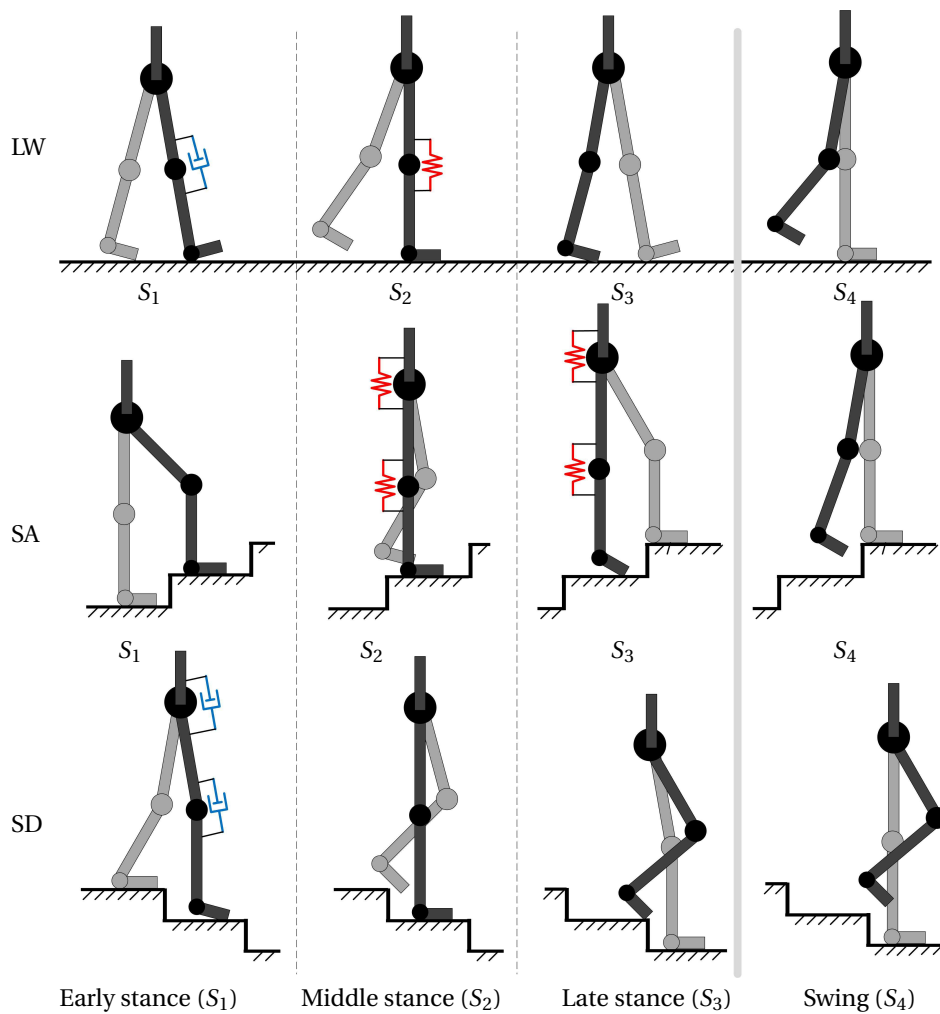


Figure 5.4 – Defined gait phases of three gait modes (level walking (LW), stair ascent (SA) and stair descent (SD)) as well as the associated assistive strategies.

Gait Modes	Joint	S ₁	S ₂	S ₃	S ₄
LW	Hip	GC	GC	GC	ZI
	Knee	GC+VD	GC+VS	GC	ZI
SA	Hip	GC	GC+VS	GC+VS	ZI
	Knee	GC	GC+VS	GC+VS	ZI
SD	Hip	GC+VD	GC	GC	ZI
	Knee	GC+VD	GC	GC	ZI

Table 5.2 – Gait mode and phase based assistive strategy

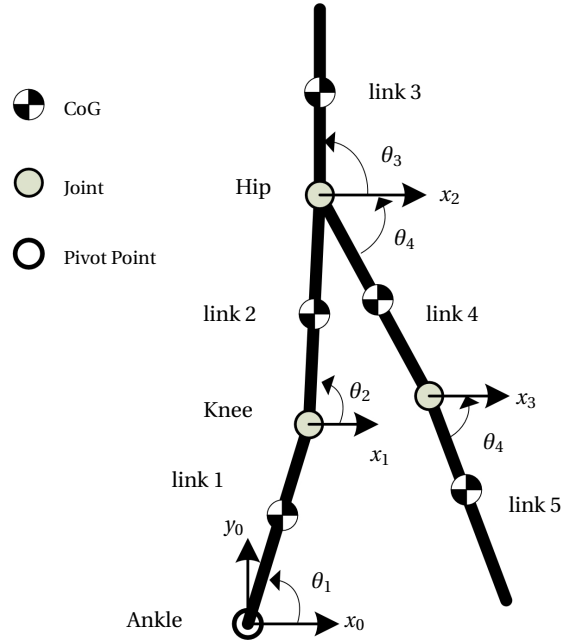


Figure 5.5 – Human model during walking. CoG denotes the center of gravity.

■ Partial Gravity Compensation (GC)

The human body is modeled using a five-link model as shown in Figure 5.5. Since the partial gravity compensation is used to reduce the human torques of the stance leg, the ankle joint of the associated leg is considered as the pivot. The required torque for the hip and knee joints to support the body's gravity (in the sagittal plane) can be expressed as follows [122]:

$$\boldsymbol{\tau}_{GC} = \eta \begin{bmatrix} l_4 \times f_4 + l_{g,4} \times G_4 + l_{g,3} \times G_3 \\ l_2 \times f_3 + l_{g,2} \times G_2 \end{bmatrix}, \quad (5.23)$$

where η is the assistance ratio. f_i represents the force acting on the joint i by the $i + 1$ th link (i.e., segment), and G_i , the gravitational force of link i . l_i and $l_{g,i}$ are the locations of the joint and the center of gravity, respectively.

■ Virtual Spring (VS)

Based on the virtual spring, the assistive joint torques are calculated as follows:

$$\boldsymbol{\tau}_{VS} = \begin{bmatrix} \alpha_{m,h}(\theta_h - \theta_{sh}) \\ \alpha_{m,k}(\theta_k - \theta_{sk}) \end{bmatrix}, \quad (5.24)$$

where $\alpha_{m,h}$ and $\alpha_{m,k}$ represent the stiffness parameters of the hip and knee joint, respectively, for the gait mode m . θ_h and θ_k are the measured hip and knee joint angles, while θ_{sh} and

Subphases	GRF	Foot position
S ₁	Large	Small
S ₂	Large	Zero
S ₃	Large	Large
S ₄	Small	Not applied

Table 5.3 – Fuzzy rules for gait phase detection (Rule-II)

θ_{sk} represent the initial angular positions of the hip and knee joints in standing position, respectively.

■ **Virtual Damper (VD)**

The assistive joint torques from the virtual dampers are calculated as follows:

$$\boldsymbol{\tau}_{VD} = \begin{bmatrix} \beta_{m,h}(\dot{\theta}_h - \dot{\theta}_{dh}) \\ \beta_{m,k}(\dot{\theta}_k - \dot{\theta}_{dk}) \end{bmatrix}, \quad (5.25)$$

where $\beta_{m,h}$ and $\beta_{m,k}$ denote the damping coefficients. $\dot{\theta}_{dh}$ and $\dot{\theta}_{dk}$ represent the corresponding desired angular velocities of the hip and knee joints, respectively.

■ **Zero Impedance (ZI)**

When the desired assistive torque is zero, the resistive torque should also be zero. Therefore, in such a case, zero-impedance control should be realized by setting $\boldsymbol{\tau}_{ZI} = 0$.

5.4.2 Gait Phases Detection

To implement the proposed hybrid assistive strategy shown in Section 5.4.1, the defined gait phases should be detected as well. Since the wearer is supposed to have partial motor ability (e.g., most elderly people), two features that are the GRF (F_{grf}) and the relative forward position ($\hat{\boldsymbol{p}}_x = \hat{\boldsymbol{p}}_{l,x} - \hat{\boldsymbol{p}}_{r,x}$ or $\hat{\boldsymbol{p}}_{r,x} - \hat{\boldsymbol{p}}_{l,x}$) of the other foot are chosen to detect the associated gait phase. The features' characteristics of each gait phase are analyzed as follows: 1) the GRF, F_{grf} , is relatively large during the stance phase (including the early stance (S₁), middle stance (S₂) and late stance (S₃)), while it is relatively small during the swing phase (S₄); 2) during the early stance (S₁), the forward position, $\hat{\boldsymbol{p}}_x$, of the reference foot is larger than the one of the other foot, while it is smaller during the late stance (S₃). The forward positions of two feet are close during the middle stance (S₂). Table 5.3 shows the features' characteristics of each gait phase. Based on these features, a fuzzy logic method is used to estimate the likelihood of each gait phase.

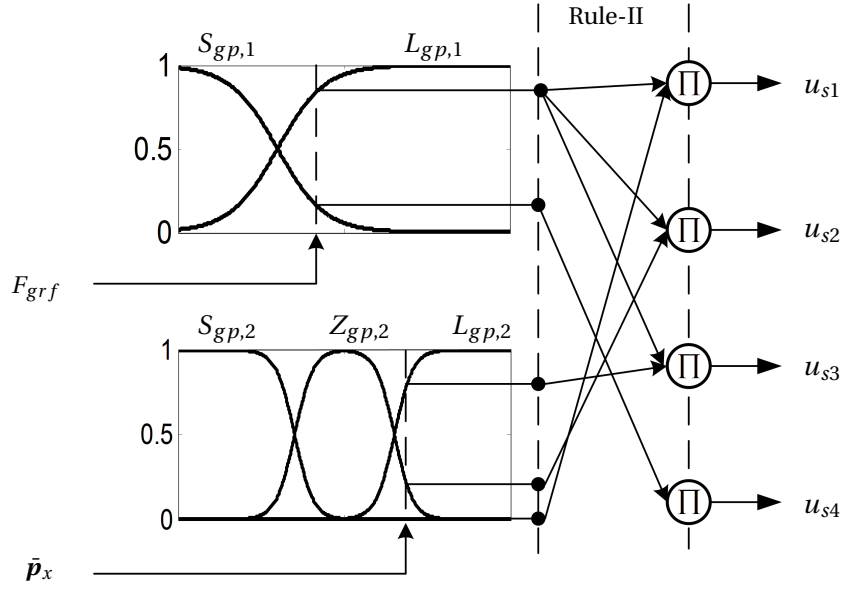


Figure 5.6 – The fuzzy logic based detection approach of the gait phases.

To define the “Large”, “Zero” and “Small” labels shown in Table 5.3, three membership functions are used:

$$\begin{aligned}
 L_{gp,f}(x_f) &= \frac{1}{2} [\tanh(\rho_f(x_f - \gamma_f)) + 1], \\
 S_{gp,f}(x_f) &= 1 - l_f(x_f), \\
 Z_{gp,f}(x_f) &= \begin{cases} 1 - s_f, & \text{if } x_f \leq \frac{\gamma_f + \delta_f}{2} \\ 1 - l_f, & \text{if } x_f > \frac{\gamma_f + \delta_f}{2} \end{cases} \quad (5.26)
 \end{aligned}$$

where $L_{gp,f}$, $Z_{gp,f}$, and $S_{gp,f}$ represent “Large”, “Zero” and “Small” membership functions, respectively. The x_f and ρ_f represent the measured values and the sensitivity coefficients of the features (i.e., F_{grf} (if $f = 1$), \bar{p}_x (if $f = 2$)), respectively. δ_f and γ_f denote the threshold values ($\gamma_f \geq \delta_f$).

Based on the fuzzy rules shown in Table 5.3 and the membership values of each feature, the likelihood of each gait phase can be calculated as shown in Figure 5.6 [143]. For example, the likelihood of early stance phase is calculated as follows:

$$u_{s1} = L_{gp,1}(F_{grf})S_{gp,2}(\bar{p}_x). \quad (5.27)$$

The likelihoods of the remaining gait phases are calculated using the same method. The likelihood matrix gathering all gait phases is denoted by:

$$\mathbf{U}_s = \begin{bmatrix} u_{s1} & u_{s2} & u_{s3} & u_{s4} \end{bmatrix} \in \mathbb{R}^{1 \times 4}, \quad (5.28)$$

where $u_{s1}, u_{s2}, u_{s3}, u_{s4} \in [0, 1]$ represent the likelihoods of the early stance, middle stance, late stance and swing phases, respectively.

5.4.3 Assistive Torque Generation

To avoid the sudden change of the assistive torques and increase the comfort of the wearer, a torque generation method is proposed to provide the continuous and smooth assistive torques based on the estimated likelihoods of gait modes and gait phases:

$$\boldsymbol{\tau} = \mathbf{U}_s \begin{bmatrix} \mathbf{M}_h \boldsymbol{\tau}_c^T \begin{bmatrix} 1 \\ 0 \end{bmatrix} \\ \mathbf{M}_k \boldsymbol{\tau}_c^T \begin{bmatrix} 0 \\ 1 \end{bmatrix} \end{bmatrix}, \quad (5.29)$$

where $\boldsymbol{\tau}_c = \begin{bmatrix} \boldsymbol{\tau}_{GC} & \boldsymbol{\tau}_{VS} & \boldsymbol{\tau}_{VD} & \boldsymbol{\tau}_{ZI} \end{bmatrix} \in \mathbb{R}^{2 \times 4}$, and $\mathbf{M}_h \in \mathbb{R}^{4 \times 4}$ and $\mathbf{M}_k \in \mathbb{R}^{4 \times 4}$ denote the likelihood matrices of the different assistive strategies for the hip and knee joints, respectively. \mathbf{U}_s denotes the likelihoods of the four gait sub-phases in (5.28). Based on the assistive strategy proposed in Table 5.2 and the likelihoods of the gait modes (5.22), \mathbf{M}_h and \mathbf{M}_k can be expressed as follows:

$$\mathbf{M}_h = \begin{bmatrix} 1 & 0 & u_{sd} & 0 \\ 1 & u_{sa} & 0 & 0 \\ 1 & u_{sa} & 0 & 0 \\ 0 & 0 & 0 & 1 \end{bmatrix} \quad (5.30)$$

and

$$\mathbf{M}_k = \begin{bmatrix} 1 & 0 & u_{sd} & 0 \\ 1 & u_{lw} + u_{sa} & 0 & 0 \\ 1 & u_{lw} + u_{sa} & 0 & 0 \\ 0 & 0 & 0 & 1 \end{bmatrix}. \quad (5.31)$$

According to the controller classification defined in [7], the whole structure of the proposed controller is shown in Figure 5.7. In this control structure, the gait mode detection is considered as the perception layer; the estimation of the required assistive torques according to gait modes constitutes the translation layer; the torque controller of the exoskeleton represents the execution layer. This chapter mainly addresses the design of the perception and translation layers. In the execution layer, a basic PID torque controller is used.

5.4. Assistive Torque Control based on Gait Mode Detection

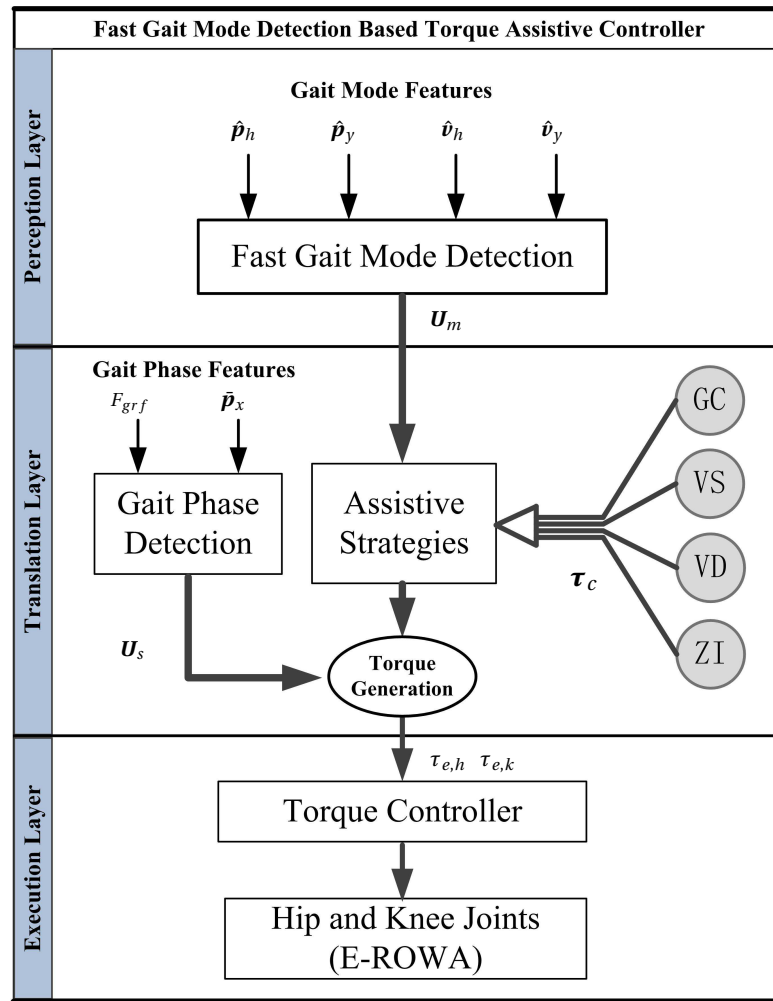


Figure 5.7 – The whole three-layer control structure. $\hat{p}_h, \hat{p}_y, \hat{v}_h$ and \hat{v}_y denote the position and velocity of the wearer’s foot. U_m is the estimated likelihoods of gait modes. F_{grf} and \bar{p}_x represent the ground reaction force and the relative foot position, respectively. U_s is the estimated likelihoods of gait phases. τ_c denotes the assistive torques from different strategies, while $\tau_{e,h}$ and $\tau_{e,k}$ represent the smoothed assistive hip and knee joint torques.

5.5 Experimental Verifications

5.5.1 Detection of the Zero-velocity Instant

In this experiment, the effectiveness of the proposed zero-velocity detection method is evaluated. As discussed in Section 5.3.3, zero-velocity detection plays a crucial role during the reference point and velocity update. A healthy subject (subject A, see Table 5.4) was asked to perform the level walking activity while wearing the E-ROWA exoskeleton and the IMU sensors. The zero-velocity instant was detected using both the proposed method (i.e., equation (5.5)) and the GRF-based methods [139]. During level walking, the foot velocity is considered to be zero when the heel and toes contact the ground at the same time (i.e. the GRF at the heel and toes levels are both higher than a relatively small threshold value). Hence, the GRF based method is used as the reference method in the following.

During the experiment, the sampling frequency of each IMU is set to 100 Hz. The length of the detection window, N , is set to 5. In order to avoid the influence of the foot movements during the stance phase, a relatively high detection threshold is chosen, $D_{th} = 3.5$. Figure 5.8 shows the detection results of five strides using both methods. It can be seen that the zero-velocity instant can be efficiently detected using the proposed method (5.5). Note that use of GRF-based methods is not always suitable for some gait modes. For example, during the stair ascent, the heel part does not always contact the ground. However, the use of the proposed method is not limited to the foot contact conditions.

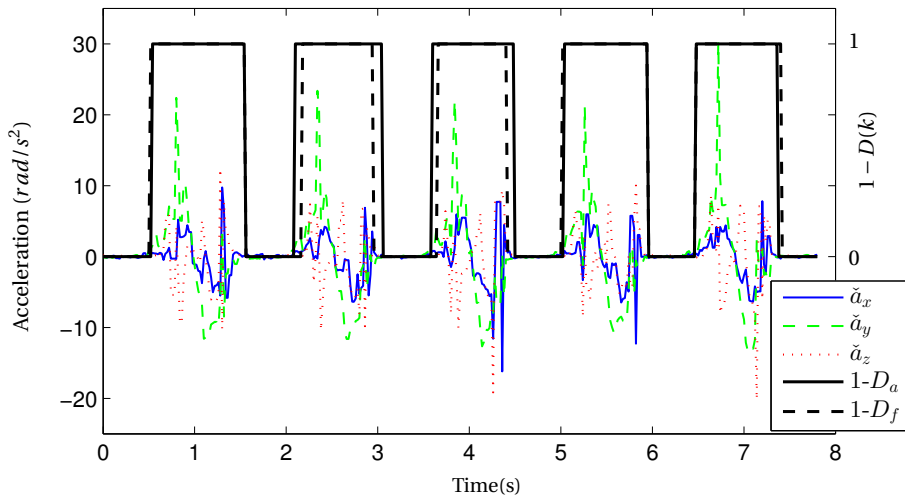


Figure 5.8 – Detection of the zero-velocity instant. \check{a}_x , \check{a}_y and \check{a}_z denote the measured foot accelerations in three axes. D_a and D_f represent the zero-velocity detection results (1: stationary state, 0: moving state) using the proposed method and the GRF respectively.

5.5. Experimental Verifications

Subjects	Sex	Age (years)	Height (m)	Weight (kg)
Subject A	Male	28	170	70
Subject B	Male	28	178	90
Subject C	Male	29	181	65

Table 5.4 – Subjects' Information

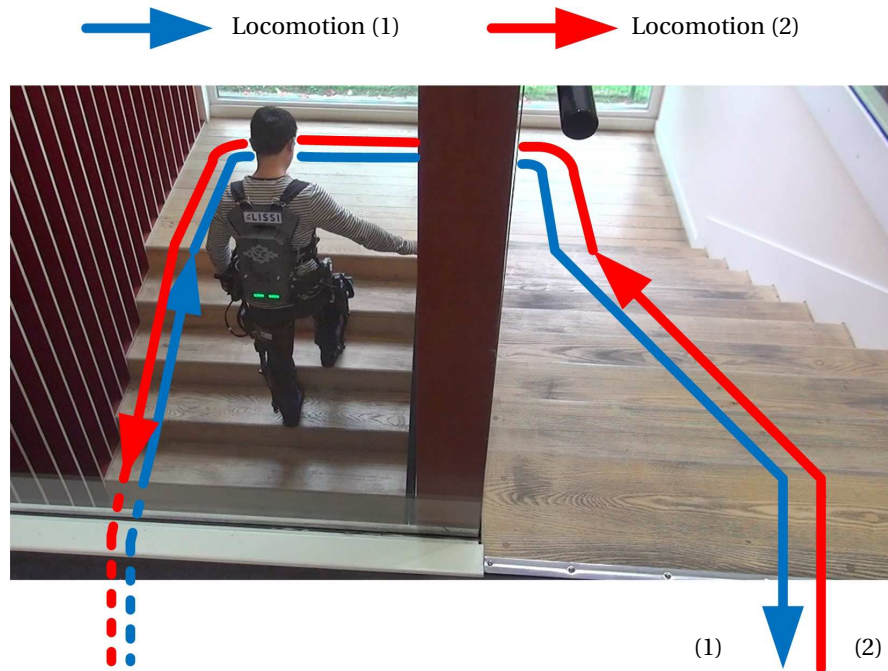


Figure 5.9 – Locomotion activities. (1): (a) standing → (b) level walking → (c) stair ascent → (d) level walking → (e) stair ascent → (f) level walking → (f) standing. (2) (a) standing → (b) level walking → (c) stair descent → (d) level walking → (e) stair descent → (f) level walking → (g) standing.

5.5.2 Gait Modes Detection

Three healthy subjects participated in this experiment. Table 5.4 shows the information related to the subjects. They were asked to walk on different terrains (level walking, stair ascent/descent) at their normal speed while wearing the exoskeleton and the IMU sensors. The latency and success rate of the gait mode detection are evaluated in this experiment. A real indoor stairs environment is used to evaluate the performance of the proposed methods, as shown in Figure 5.9. There are twenty stair steps with the same height (16 cm) and depth (30 cm). The subjects were asked to perform the following activities: Locomotion (1) ((a) standing → (b) level walking → (c) stair ascent → (d) level walking → (e) stair ascent → (f) level walking → (f) standing); Locomotion (2) ((a) standing → (b) level walking → (c) stair descent → (d) level walking → (e) stair descent → (f) level walking → (g) standing). The

Figures 5.10 and 5.12 show the extracted features (i.e., \hat{p}_h , \hat{p}_y , $\dot{\hat{p}}_h$ and $\dot{\hat{p}}_y$) during the Locomotion (1) and (2) of the subject A, respectively. For the same gait mode, the accuracy of extracted features are not sensitive to the measurement time and the walking distances. For example, the measured step height, i.e., the vertical position (i.e., \hat{p}_y at the end of the step) of each step during stair ascent/descent is almost constant, and equal to the stair height (\hat{p}_y ; mean = $0.161m$, std = $0.00897m$). At the same time, it can be observed that the features are different as function of the gait modes, as discussed in Section 5.3.2.

Regarding the fuzzy logic based approach for gait mode detection, the linguistic variables of four extracted features are chosen based on the normal terrains such as the stair height ($\geq 0.1m$) and normal walking speed of the adults. Figures 5.11 and 5.13 show the estimated likelihoods of three gait modes. As discussed in Section 5.3.2, the gait mode is detected from the beginning of the defined period P_2 (see Figure 5.2). Here, the moment, $\bar{p}_x = 0.05m$, is used to denote the beginning of the period P_2 . During period P_2 , the gait mode can be fastly detected based on the velocity features, $\dot{\hat{p}}_h$ and $\dot{\hat{p}}_y$, although the likelihoods of the detected gait mode is relatively as low as $0.5 \sim 1$. However, likelihoods of the detected gait mode rise quickly ($< 0.15s$) to a relatively high value (≈ 1) with the increase of the position features (see Figures 5.11(a) and 5.13(a)). Figures 5.11(b) and 5.13(b) show the detected gait modes and the vertical tracking positions ($p_{l,y}$ and $p_{r,y}$) of the two feet. It can be observed that each stair step can be clearly and accurately detected (i.e., the features accuracy does not decrease with time); the transitions among the three gait modes can be detected at the beginning of each step ($\bar{p}_x \approx 0.05m$);

In order to evaluate the success rate of the proposed gait mode detection method, each subject was asked to perform three groups of locomotion activities: Locomotion (1) and Locomotion (2), as shown in Figure 5.9. The success rates of gait mode detection are shown in Table 5.5. Note that the success rates are calculated based on the detected gait modes and the real terrains. During the period P_2 , the success rate is higher than 96%, while it is 100% during period P_3 . When the wearer performs the level walking with a relatively high foot clearance, the detected gait mode at the beginning of period P_2 may show stair descent for a short movement ($< 0.15s$) (Subject B). At the same time, during stair descent, if the wearer reduces the speed before going down the next stair, a level walking mode may be detected for a short moment; e.g., Subject C.

5.5.3 Assistive Torque Generation

Based on the estimated gait modes and gait phases, different assistive strategies (GC, VS, VD and ZI) are selected to provide torque assistance at the hip and knee joint level (see Table 5.2). The associated parameters of the GC, VS and VD control strategies are shown in Table 5.6. Considering the subjects' motor ability and the maximum output torques of the exoskeleton, a relatively low assistive ratio of partial gravity compensation, $\eta = 0.2$, is used. The desired hip and knee angular positions (i.e., θ_{sh} and θ_{sk}) of virtual spring (VS) for level walking and

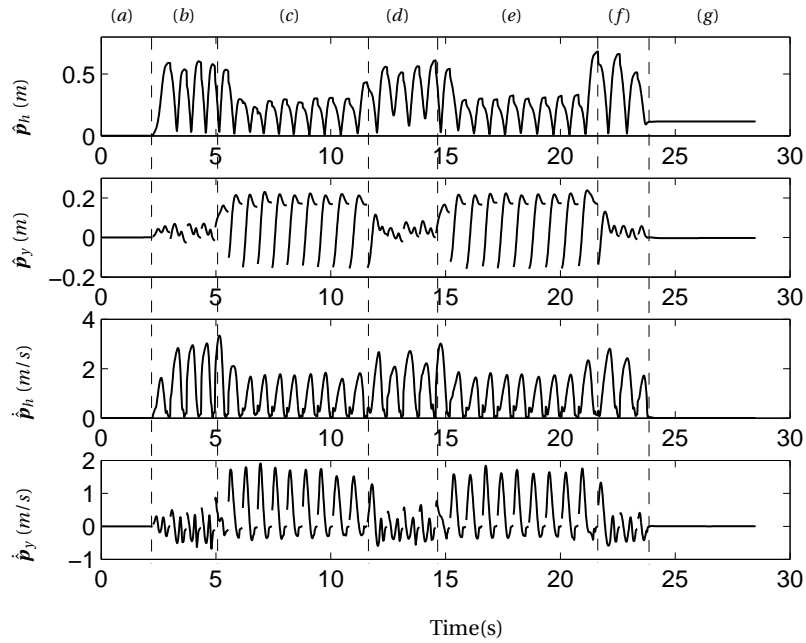


Figure 5.10 – Detection of the gait modes: extracted features during the locomotion activities (1): (a) standing → (b) level walking → (c) stair ascent → (d) level walking → (e) stair ascent → (f) level walking → (g) standing.

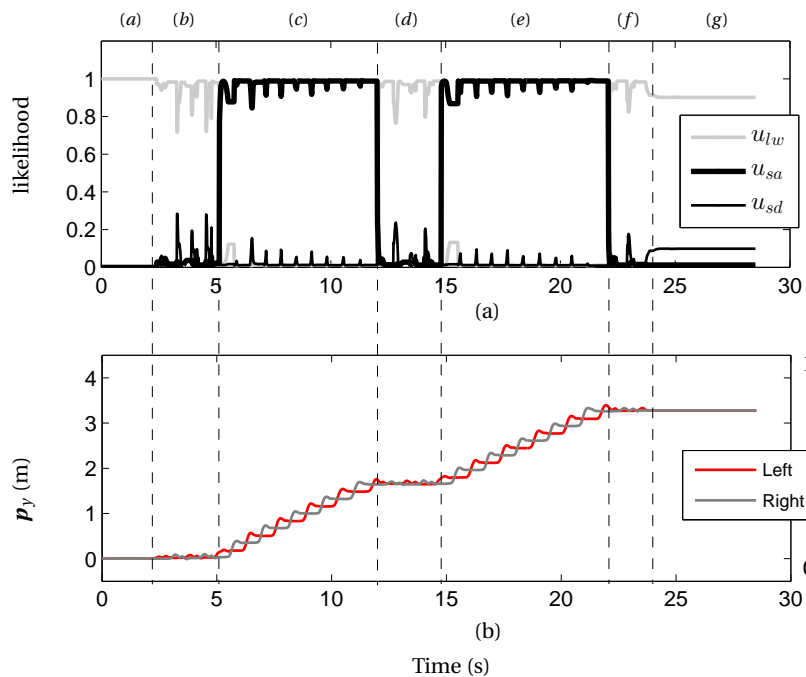


Figure 5.11 – Detection of the gait modes during the locomotion activities (2): (a) standing → (b) level walking → (c) stair ascent → (d) level walking → (e) stair ascent → (f) level walking → (g) standing. “Left” and “Right” in figure (b) denote the tracking vertical positions of left and right foot, $p_{l,y}$ and $p_{r,y}$, respectively.

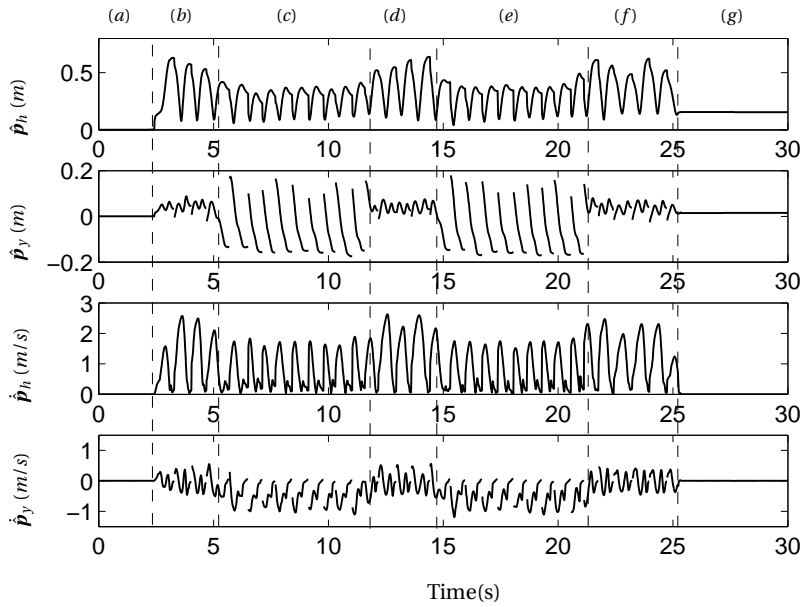


Figure 5.12 – Detection of the gait modes: extracted features during the locomotion activities (2): (a) standing level → (b) walking → (c) stair descent → (d) level walking → (e) stair descent → (f) level walking → (g) standing.

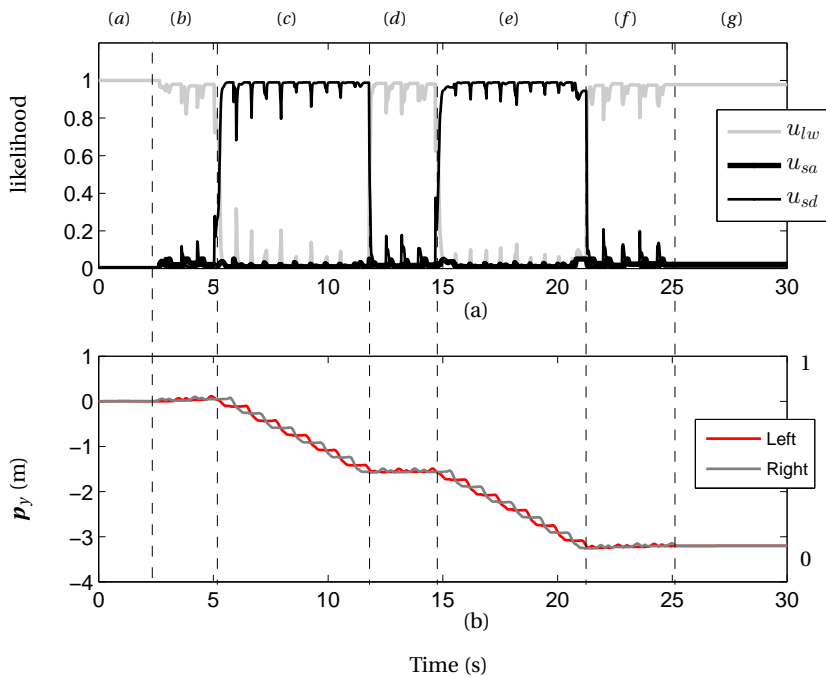


Figure 5.13 – Detection of the gait modes during the locomotion activities (2): (a) standing → (b) walking → (c) stair descent → (d) level walking → (e) stair descent → (f) level walking → (g) standing. “Left” and “Right” in figure (b) denote the tracking vertical potions of left and right foot, $p_{l,y}$ and $p_{r,y}$, respectively.

5.5. Experimental Verifications

Gait Mode	LW	SA	SD
	$(S_{p2}, S_{p3})/S_N$	$(S_{p2}, S_{p3})/S_N$	$(S_{p2}, S_{p3})/S_N$
Subject A	(47, 47)/47	(60, 60)/60	(60, 60)/60
Subject B	(48, 50)/50	(60, 60)/60	(60, 60)/60
Subject C	(42, 42)/42	(60, 60)/60	(59, 60)/60

S_N -Step number; S_{p2} , S_{p3} - successful detected steps in period P_2 and P_3 respectively.

Table 5.5 – Success rate of gait mode detection

stair ascent are chosen according to the associated equilibrium hip and knee joint angles of the normal gait during the corresponding gait phases [57], in which they can be considered to be constant. In terms of the desired angular velocities ($\dot{\theta}_{dk}$) of the knee joint of the virtual damper (VD), they are considered to be zero during the early stance of level walking and stair descent. At the same time, the desired angular velocities ($\dot{\theta}_{dh}$) of hip joint during early stance of stair descent is also considered to be equal to zero. The reminding parameters of the virtual spring and virtual damper are chosen based on wearer's motor ability.

Figure 5.14 shows the measured features, the GRF, F_{grf} , and the relative forward foot position, \bar{p}_x , of one gait step during level walking, stair ascent and stair descent, respectively. Figures 5.15 shows the associated hip and knee joint angles (θ_h and θ_k), the estimated likelihoods of the gait phases (U_s), the assistive hip and knee joint torques ($\tau_{e,h}$ and $\tau_{e,k}$), respectively. It can be noted that continuous likelihoods of the four gait phases can be obtained based on the GRF, F_{grf} , and relative forward foot position, \bar{p}_x . Regarding the assistive torques, it can be observed that the virtual spring and damper act at the knee joint level during level walking (see the torque $\tau_{VS,k}$ and $\tau_{VD,k}$ in Figure 5.15a). However, the assistive torques are relatively small when the wearer performs a normal gait during early stance, S_1 , and middle stance, S_2 . During stair ascent, the virtual spring provides a relatively big torque during the middle stance, S_2 , when the hip and knee joint angles do not reach the associated equilibrium points (see $\tau_{VS,h}$ and $\tau_{VS,k}$ in Figure 5.15b). During the stair descent, the virtual damper provides the assistive torques at the early stance, S_1 , to reduce the floor impact (see $\tau_{VD,h}$ and $\tau_{VD,k}$ in Figure 5.15c). Additionally, although the likelihoods of the estimated gait modes are relatively small during a short moment of the middle stance, S_2 , (see Figures 5.11(a) and 5.13(a)), there is a relatively small impact on the assistive torques.

It should be also noted that the fast gait mode detection plays an important role for the transitions of different assistive strategies. For example, largely bending the knee joint, θ_k , during mid stance of level walking or stair ascent is considered as an abnormal movement, and may cause fall risk, while it is a required movement for stair descent [57], (also see θ_k in Figure 5.15c). The stiffness of the knee joint during the middle stance under the level walking and stair ascent is enforced using the virtual spring (see $\tau_{VS,k}$ in Figures 5.15a and 5.15b),

Strategies	Parameters	Values
GC	η	0.2
VS	$a_{m,h}, a_{m,k}$	20, -25 (Nm/rad)
	θ_{sh}, θ_{sk}	0.1745, 0.1396 (rad)
VD	$\beta_{m,h}, \beta_{m,k}$	4, -2 (Nm·s·rad ⁻¹)
	$\dot{\theta}_{dh}, \dot{\theta}_{dk}$	0, 0 (rad/s)

Table 5.6 – Parameters of three assistive control strategies

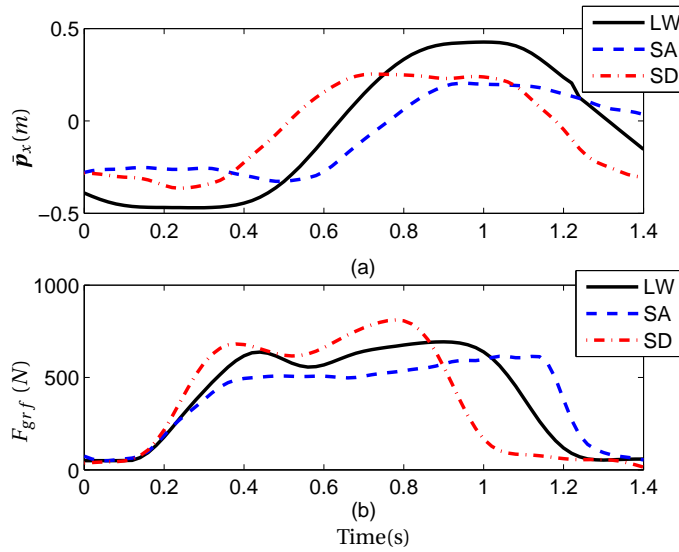


Figure 5.14 – Torque generation for three gait modes: gait phase features (a) the relative forward foot position. (b) the GRF.

while only the partial gravity compensation is used during the middle stance of stair descent (see $\tau_{VS,k}$ in Figure 5.15c). Hence, incorrect gait mode detection may increase the human efforts during stair descent or fall risk in level walking or stair ascent. In this case, a fast gait mode detection provides transparent transitions between these assistive strategies.

5.5.4 Comparison Study

In order to show the effectiveness of the proposed strategy in terms of assistive torques, a comparison experiment was implemented. A subject (Subject A) was asked to perform two groups of stair ascent/descent activities (see Figure 5.9) in three states: baseline state (i.e., without wearing the exoskeleton), non-assistive state (i.e., in exoskeleton without assistance), assistive state (i.e., in exoskeleton with assistance). The wearer was asked to implement these activities with their normal gait patterns, and keep the similar walking speed during same activities. EMG signals of the muscles from the extensor groups (i.e., vastus lateralis) of

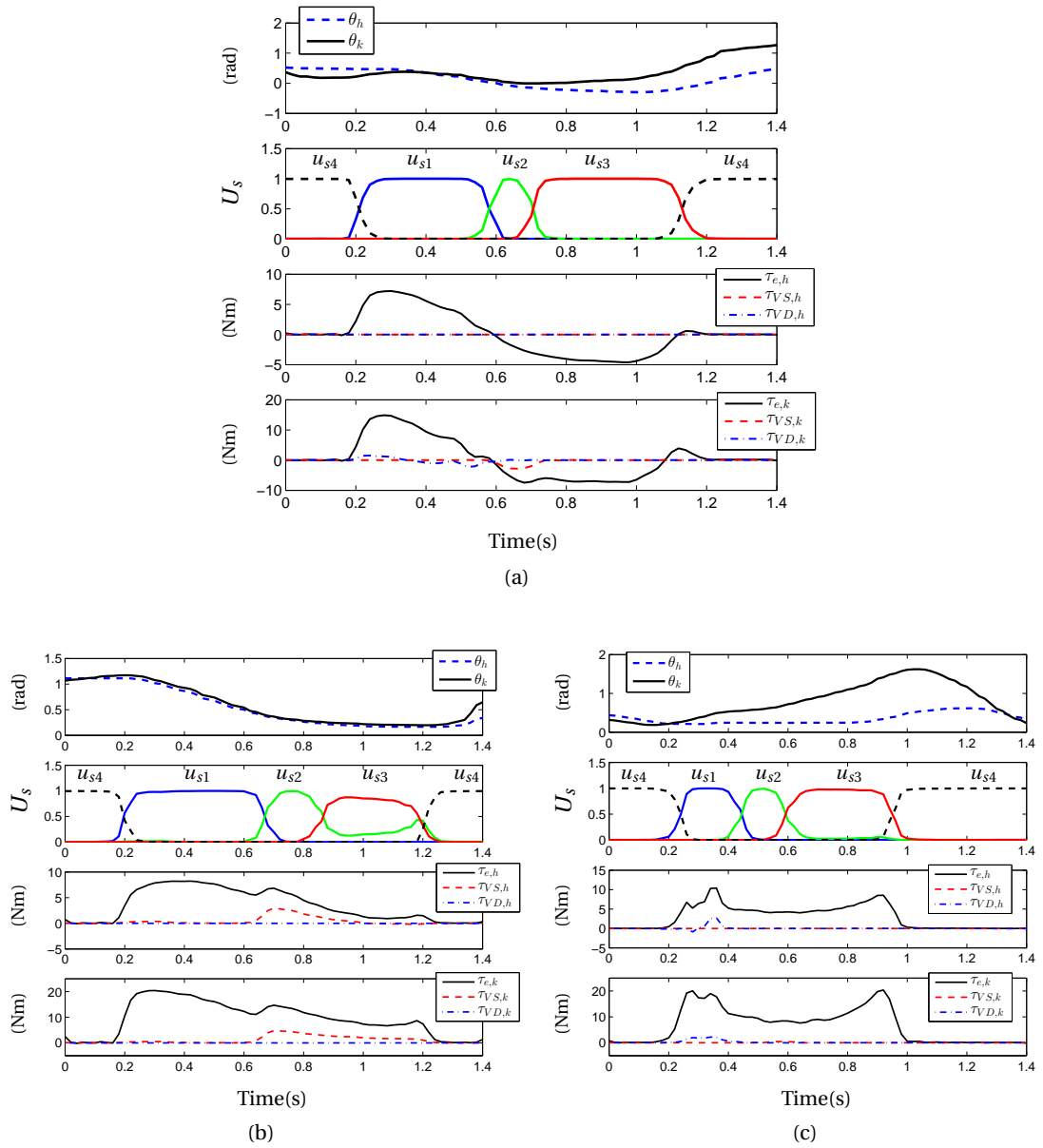


Figure 5.15 – Generated assistive torques during level walking (a), stairs ascent (b) and stair descent (c). $\tau_{e,h}$ and $\tau_{e,k}$ represent the assistive torques at hip and knee joint level, respectively.

the right knee joint are measured during the locomotion activities. It should be noted that the vastus lateralis plays an important role in generating assistive torque during the whole stance phase of both stair ascent and descent. This is also why these two activities are chosen. Although the activities of this muscle cannot be used to estimate the accurate human knee joint torque, its amplitude and trend can be used to show the human effort. The measured EMG signals during the above three cases are processed using the following steps: high-pass filtering at 30 Hz using a fourth-order Butterworth filter; elimination of the measurement noise; full-wave rectification; low-pass filtering at 10 Hz using a fourth-order Butterworth filter.

Figure 5.16 shows one group of the processed EMG signals of the vastus lateralis. One can notice that the EMGs signals of the vastus lateralis show similar curves in above three states. This implies that the assistive torque of the exoskeleton is in accordance with the one generated by the wearer's muscles. In terms of the amplitudes of the EMG signals of three states, Figure 5.17 shows the ratios of EMG signals' peak values during the non-assistive and assistive states compared to the baseline state. During stair descent, the EMG signals' peak values of non-assistive state increase by $12.25 \pm 7.38\%$, while decrease to the similar level as those during the baseline state when the wearer is assisted. During stair ascent, the peak values in non-assistive state increase a little ($2.44 \pm 4.73\%$), while decrease by $-11.44 \pm 4.55\%$ in assistive state compared to those during the baseline state. The results indicate that the human effect can be efficiently reduced with the proposed assistive strategy. It can be further infer that the human effort can be more reduced with the increase of the maximum output torques of the exoskeleton and the assistive ratios as shown in Table 5.6.

5.6 Conclusion

In this chapter, a fast gait mode detection based assistive control strategy of a lower limb exoskeleton is proposed to assist the dependent people to achieve three common gait modes (level walking, stair ascent/descent) during daily living activities. The horizontal and vertical positions and velocities of the swing foot are chosen as the gait mode features to achieve the fast detection that are required for the real-time assistive control. A Kalman filter based fusion method is proposed to ensure the accurate estimations of the features by combining a zero-velocity update algorithm and a kinematic model based method. A fuzzy logic based approach is proposed to estimate the likelihoods of the gait modes. In each gait mode, four gait phases are further detected depending on the relative position between the feet and the ground reaction force. Based on the estimated gait mode and associated gait phases, the appropriate assistive strategy, including gravity compensation, virtual spring, virtual damper, and zero impedance assistance, is selected for different gait modes. The experimental results show that the latency and success rate both satisfy the requirements for long-term walking. The effectiveness of the proposed assistive strategy is evaluated with healthy subjects. It shows that the exoskeleton can provide efficient assistance for the wearer according to his/her gait modes.

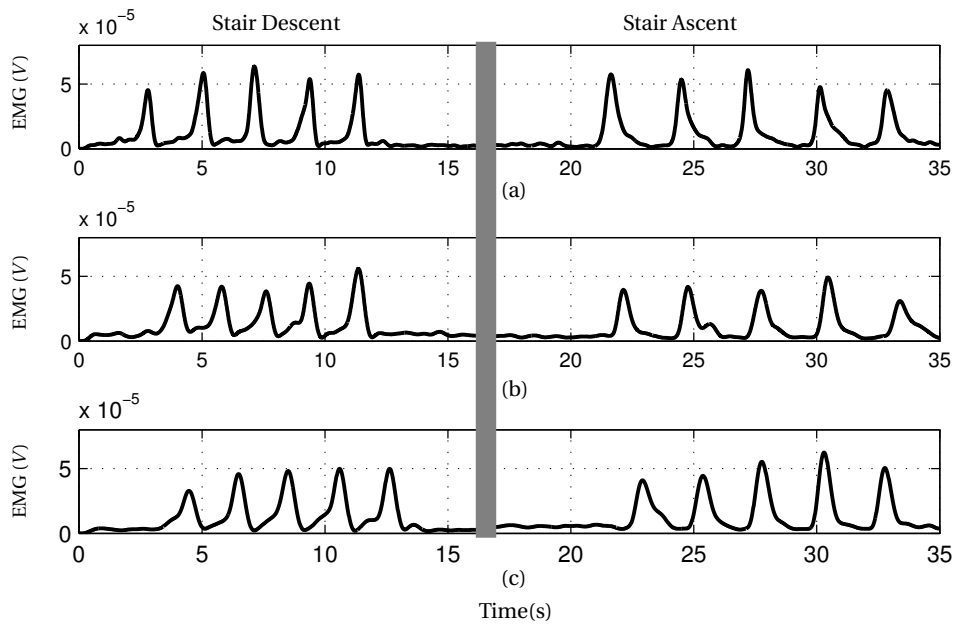


Figure 5.16 – One group of processed EMG signals during stair descent and ascent in three cases: (a) wearing the exoskeleton without assistance, (b) wearing the exoskeleton with assistance, (c) without wearing the exoskeleton.

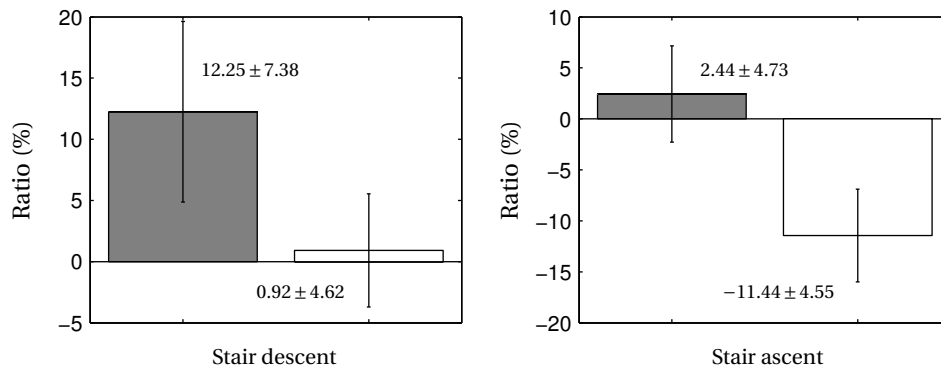


Figure 5.17 – Comparison of the peak values of the processed EMG signals. The *gray bars* denote the ratios of the EMG signals' peak values during the non-assistive state compared to the baseline state, while the *white bars* denote the ratios of the EMG signals' peak values in the assistive state compared to the baseline state.

Since the proposed methods can be easily achieved and only low-cost sensors, such as force sensing resistors, IMUs and angle sensors are required, the proposed method can be widely used in lower-limb power-assist exoskeleton systems in practice. In the future work, more gait modes, such as ramp ascent/descent, can be further studied based on the proposed structure. A new feature extracted using the IMU sensors, i.e., the foot inclination angle, could be introduced to fast identify the ramp ascent/descent by cooperating with the proposed features. In the meantime, experiments conducted with different subjects (e.g., elderly people), and with varied walking speed will be studied.

Summary

Different gait modes, such as level walking and stair ascent/descent, show different lower-limb kinematic and kinetic characteristics. Therefore, an accurate perception of the gait modes is critical for a wearable robot to provide appropriate power assistance. In this chapter, a fast gait mode detection method based on a body sensor system is proposed. A fuzzy logic based algorithm is utilized to estimate the likelihoods of gait modes in real-time. Since the proposed fast gait mode detection makes it possible to select appropriate kinematic and kinetic models for each gait mode, assistive torques required for assisting the human motions can be obtained more naturally and immediately. The proposed methods are all verified by experiments with a lower limb exoskeletal assistive robot, called E-ROWA.

6 Conclusions and Outlook

AN envisioned important application of lower limb exoskeletons is to assist individuals with limited muscular capabilities during daily living activities. This requires that the exoskeleton be able to provide natural, efficient and robust physical power assistance by taking into account the wearer's sensor-motor ability. In other words, it is necessary to develop human intention based assistive strategies as well as control methods that are robust with respect to disturbances and efficient to accomplish the wearer's desired movement. In this dissertation, we focus on the development of control strategies that are classed into three types: joint-level tracking control, intention-based single-task assistive control and intention-based multi-task power assistive control. For each type, we proposed a self-contained control strategy. Our major contributions are summarized as follows:

- Joint level tracking control strategy:
 1. We developed a robust tracking control approach of a knee-joint lower limb exoskeleton by combining a nonlinear disturbance observer with sliding mode control. The proposed method improves the control bandwidth and tracking precision and reduces the chattering effect. On this basis, we proposed a disturbance observer based terminal sliding mode control approach that can further ensure that the tracking error converges to the sliding surface in finite time.
 2. The stability of the proposed disturbance-based sliding mode control and terminal sliding mode control were both theoretically analyzed using the Lyapunov function. The convergence time of the proposed disturbance observer based terminal sliding mode control was theoretically discussed under two cases: when there exist initial tracking errors as well as when there exist non-initial tracking errors caused by disturbances.
 3. The proposed methods were all evaluated by experiments with the participation of different subjects. Comparison experiments were conducted to show the performance of basic SMC, NDO-based SMC and NDO-based TSMC in terms of tracking precision, convergence time and robustness. The results showed that the proposed NDO-based TSMC significantly improved the tracking performance, convergence time and robust-

ness with respect to modeling uncertainties and disturbances compared to the other two methods.

- Intention based single-task assistive control strategy:
 1. We developed an active impedance control structure that provides power assistance for the wearer by compensating the original impedance of the human exoskeleton system to a desired level. The human joint torque, which indicates the human motion intention, was estimated using a nonlinear observer. We developed a nonlinear disturbance observer based sliding mode control for lower limb exoskeletons to ensure the accurate tracking of the desired joint trajectory. The proposed structure can be easily used for assisting different lower limb activities.
 2. We developed a single-joint active impedance control approach to assist in knee joint flexion/extension movements using the EICOSI exoskeleton. The proposed controller is sufficiently robust to compensate not only for friction and gravity but also for system inertia without affecting the stability of the system. The characteristics and performance of the proposed control approach were theoretically analyzed. The root-mean-square (RMS) of the EMG signal is used and cross-evaluated as a metric to show the changes in human effort when performing the same joint movements with different impedance states. The experimental results show that the original inertia, damping and gravity of the human joint can be efficiently reduced and the magnitude of the subjects' EMG signals can be reduced by up to 60%. To the best of our knowledge, the proposed approach, in which a nonlinear general torque-sensor-less control method is proposed to reduce the human muscular activity using inertia, damping and stiffness compensation, is unique in the field of robot-aided physical assistance.
 3. We further extended the active impedance control structure to the multi-joint case and developed a nonlinear control approach to assist dependent people with lower limb muscular weakness during sit to stand movements. We designed a sit-to-stand dynamic model of the human exoskeleton system, in which the seat forces were assumed to compensate for human gravity at the sitting position and fade to zero after the sit-off point. The increasing rates of the seat forces were indicated using the changes of the ground reaction forces. We proposed a time-varying desired impedance model according to the wearer's STS speed, which is commonly used to indicate the human lower limb motor ability. The nonlinear multi-joint active impedance control approach was designed in a generalized way. We analyzed and simulated the performance of the proposed approach as well as its robustness with respect to system modeling uncertainties. The effectiveness of the proposed methods was evaluated by experiments with a healthy subject. The results showed that the proposed active impedance approach can efficiently estimate the human joint torques and provide appropriate power support to the wearer.

-
- Gait mode based multi-task assistive control strategy:
 1. We developed a fast gait mode detection algorithm to estimate three common daily living activities such as level walking and stair ascent/descent. The proposed algorithm is able to detect the transition between gait modes at the early beginning of a new gait step. This is achieved by using kinematic features namely the velocity and position of the wearer's foot during walking. The gait mode transitions can be quickly estimated using the foot velocity (i.e., low latency) and accurately detected based on the foot position (i.e., high detection success rate). We proposed a feature update algorithm to ensure accurate feature estimation by combining a zero-velocity detection method and the use of a human kinematic model. The advantages of these two methods are integrated using a Kalman filter according to the wearer's postures and foot states. Based on the actually estimated dynamic features, a fuzzy logic based algorithm is used to estimate the continuous likelihood of each gait mode. To the best of our knowledge, this is the first attempt to detect the human gait modes using features such as the velocity and position of the wearer's foot during walking.
 2. We developed a hybrid power assistive strategy of a lower limb exoskeleton (E-ROWA) to provide different assistances to the wearer according to the gait mode. The proposed assistive strategy is an alternative method to the traditional finite-state machine algorithms that switch between different strategies according to the changes of the defined states (e.g., gait modes and phases). The assistive torques of the proposed strategy are directly calculated based on the outputs of all assistive approaches and the likelihoods of the associated gait modes and phases. This can provide smooth assistive torques and efficiently avoid sudden changes.
 3. The proposed approaches were all evaluated by experiments with the lower limb exoskeleton E-ROWA. Three healthy subjects participated in the experiments. The results showed that the latency and success rate of the gait mode detection both satisfied the requirements for long-term walking. Using the proposed assistive strategy, the exoskeleton could provide efficient assistance for the wearer according to his/her gait modes. The proposed gait mode based assistive approach can be easily achieved, and only low-cost sensors, such as force-sensing resistors, IMUs and angle sensors, are required.

Based on the promising results presented in this dissertation, we believe that the proposed methods contribute an important step towards the efficient control of lower limb exoskeletons for assisting in the daily living activities of individuals suffering from muscular weakness. In addition, the proposed methods can be further extended in several research directions. One promising direction would be the development of a control strategy that combines gait motion detection algorithms used for high-level control and the active impedance control structure presented as the mid-level control strategy. This integration can enable the lower limb exoskeleton to provide human intention based power assistance during different daily living activities. The proposed gait mode detection algorithm mainly focuses on locomotive activities such as level walking and stair ascent/descent. It can be further extended to detect

other gait modes, such as ramp walking and sit-to-stand, using the FSR sensors and the IMU mounted on the wearer's foot. Regarding the hardware requirements of the gait mode detection algorithm, the joint angles could also be measured using the IMU sensors. This will allow other types of exoskeletons, such as a single-joint exoskeleton, to use the proposed gait mode detection algorithm. Additionally, the proposed active impedance control can be used for assisting in various activities, since it is designed in a generalized way.

Our approach to identify the parameters of the multi-joint exoskeleton E-ROWA is based on the passive pendulum test, in which the test frequency was limited in a relatively small and low range. Hence, one can further study advanced parameter identification approaches to obtain more accurate system parameters. As discussed in Section 4, a higher power assistance ratio could be used if we could obtain a more accurate human-exoskeleton system model.

The proposed control strategies were mainly evaluated by experiments conducted on healthy subjects. The assistive effectiveness was assessed using the reduction of the associated muscular EMG signals. Although we believe that the same effectiveness can be obtained for assisting individuals with limited muscular strength, more experiments on the elderly or infirm need to be implemented in future work. We believe that the proposed active impedance control would also be applicable for rehabilitation purposes, as it can reduce the required human efforts to perform the same movements and thereby encourage the wearers to practice their own motor abilities.

A Modeling of the Sit-to-Stand Movement

Let s_i , c_i , s_{ij} and c_{ij} be the abbreviations of $\sin(\theta_i)$, $\cos(\theta_i)$, $\sin(\theta_i - \theta_j)$ and $\cos(\theta_i - \theta_j)$ respectively, with $i, j = 1, 2, 3$.

The matrix $\mathbf{M}(\mathbf{q})$ in (4.2) is given by:

$$\mathbf{M}(\mathbf{q}) = [M_{ij}]_{3 \times 3} \quad (\text{A.1})$$

where

$$M_{11} = I_{e1} + I_{h1} + l_1^2 m_{e2} + l_1^2 m_{e3} + l_1^2 m_{h2} + l_1^2 m_{h3} + k_{e1}^2 l_1^2 m_{e1} + k_{h1}^2 l_1^2 m_{h1}$$

$$M_{22} = I_{e2} + I_{h2} + l_2^2 m_{e3} + l_2^2 m_{h3} + k_{e2}^2 l_2^2 m_{e2} + k_{h2}^2 l_2^2 m_{h2}$$

$$M_{33} = m_{e3} k_{e3}^2 l_3^2 + m_{h3} k_{h3}^2 l_3^2 + I_{e3} + I_{h3}$$

$$M_{12} = l_1 l_2 (m_{e3} + m_{h3} + k_{e2} m_{e2} + k_{h2} m_{h2}) c_{12}$$

$$M_{13} = l_1 l_3 (k_{e3} m_{e3} + k_{h3} m_{h3}) c_{13}$$

$$M_{23} = l_2 l_3 (k_{e3} m_{e3} + k_{h3} m_{h3}) c_{23}$$

$$M_{21} = M_{12}$$

$$M_{31} = M_{13}$$

$$M_{32} = M_{23}.$$

The matrices $\mathbf{C}(\mathbf{q}, \dot{\mathbf{q}})$ and $\mathbf{G}(\mathbf{q})$ in (4.2) are given by:

$$\mathbf{C}(\mathbf{q}, \dot{\mathbf{q}}) = [C_{ij}]_{3 \times 3}, \quad \mathbf{G}(\mathbf{q}) = [G_{ij}]_{1 \times 3}. \quad (\text{A.2})$$

Appendix A. Modeling of the Sit-to-Stand Movement

where

$$\begin{aligned}
 C_{11} &= C_{22} = C_{33} = 0 \\
 C_{12} &= l_1 l_2 s_{12} (m_{e3} + m_{h3} + k_{e2} m_{e2} + k_{h2} m_{h2}) \dot{\theta}_2 \\
 C_{13} &= l_1 l_3 s_{13} (k_{e3} m_{e3} + k_{h3} m_{h3}) \dot{\theta}_3 \\
 C_{21} &= -l_1 l_2 s_{12} (m_{e3} + m_{h3} + k_{e2} m_{e2} + k_{h2} m_{h2}) \dot{\theta}_1 \\
 C_{23} &= l_2 l_3 s_{23} (k_{e3} m_{e3} + k_{h3} m_{h3}) \dot{\theta}_3 \\
 C_{31} &= -l_1 l_3 s_{13} (k_{e3} m_{e3} + k_{h3} m_{h3}) \dot{\theta}_1 \\
 C_{32} &= -l_2 l_3 s_{23} (k_{e3} m_{e3} + k_{h3} m_{h3}) \dot{\theta}_2 \\
 G_{11} &= (m_{e2} + m_{e3} + m_{h2} + m_{h3} + k_{e1} m_{e1} + k_{h1} m_{h1}) g l_1 c_1 \\
 G_{12} &= (m_{e3} + m_{h3} + k_{e2} m_{e2} + k_{h2} m_{h2}) g l_2 c_2 \\
 G_{13} &= (k_{e3} m_{e3} + k_{h3} m_{h3}) g l_3 c_3 .
 \end{aligned}$$

The matrices \mathbf{J}_Θ and \mathbf{J}_F in (4.2) are as follows:

$$\mathbf{J}_\Theta = \begin{bmatrix} 1 & 0 & 0 \\ 1 & 1 & 0 \\ 1 & 1 & 1 \end{bmatrix}, \quad \mathbf{J}_F = \begin{bmatrix} l_1 s_1 & l_2 s_2 & 0 \\ l_1 c_1 & l_2 c_2 & 0 \end{bmatrix}. \quad (\text{A.3})$$

The matrices c_x and c_y in (4.5) are expressed as follows:

$$c_x = \frac{k_1 g c_1}{l_2 s_{12}}, \quad c_y = \frac{k_2 g}{l_2 s_{12}} \quad (\text{A.4})$$

where

$$\begin{aligned}
 k_1 &= (m_{e2}(l_2 - k_{e2} l_2) + m_{h2}(l_2 - k_{h2} l_2) + k_{e1} l_2 m_{e1} + k_{h1} l_2 m_{h1}) c_2 - (k_{e3} l_3 m_{e3} \\
 &\quad + k_{h3} l_3 m_{h3}) c_3 \\
 k_2 &= (m_{e2} + m_{e3} + m_{h2} + m_{h3} + k_{e1} m_{e1} + k_{h1} m_{h1}) l_2 c_1 s_2 - (m_{e3} + m_{h3} + k_{e2} m_{e2} \\
 &\quad + k_{h2} m_{h2}) l_2 c_2 s_1 - (k_{h3} m_{h3} + k_{e3} m_{e3}) l_3 c_3 s_1 .
 \end{aligned}$$

B Calibration Procedure of the IMU

Alignment

Firstly, the wearer is asked to stay in a standing posture where the vertical axis ${}^B Y_j$ of each foot is considered to be equal to the gravity vector as measured by the IMU. Secondly, the wearer is asked to perform a flexion/extension movement around the ankle joints in the sagittal plane. The axis ${}^B Z_j$ of the foot is defined using the direction of the angular velocity measured by the attached IMUs. Note that ${}^B Z_j$ is equal to the direction of the angular velocity during flexion movements, or the opposite direction during extension movements. Hence, the three unit vectors of orientation ${}^S R_{B,j}$ can be denoted by:

$$\begin{cases} {}^S Y_{B,j} = \frac{\mathbf{g}_{stand,j}}{|\mathbf{g}_{stand,i}|} \\ {}^S Z_{B,j} = d \frac{\boldsymbol{\omega}_{joint,i}}{|\boldsymbol{\omega}_{joint,j}|} \\ {}^S X_{B,j} = \frac{{}^S Z_{B,j} \times {}^S Y_{B,j}}{|{}^S Z_{B,j} \times {}^S Y_{B,j}|} \end{cases} \quad (\text{B.1})$$

where $\mathbf{g}_{stand,j}$ denotes the measured gravity vector of each IMU in the standing posture. d represents the rotation direction of each joint ($d = \{-1, 1\}$), and $\boldsymbol{\omega}_{joint,j}$, the measured angular velocity.

Consider that the measured vectors ${}^S Y_{B,j}$ and ${}^S Z_{B,j}$ in (B.1) may not be orthogonal due to the presence of the measurement error, the orientation ${}^S R_{B,j}$ is modified as follows:

$${}^S R_{B,j} = [{}^S X_{B,j} \ {}^S Y_{B,j} \ {}^S X_{B,j} \times {}^S Y_{B,j}] \quad (\text{B.2})$$

One can notice that the measured ${}^S Z_{B,j}$ axis is replaced by the term ${}^S X_{B,j} \times {}^S Y_{B,j}$. This is due to the fact that it is not easy for the wearer to ensure flexion/extension movements are always in the sagittal plane.

Glossary

AIC	Active Impedance Control
BF	Biceps Femoris
cRSEA	compact Rotary Series Elastic Actuator
DoF	Degree of Freedom
E-ROWA	Exoskeletal-Robotic Orthotics for Walking Assistance
EICOSI	Exoskeleton Intelligently COMMunicating and Sensitive to Intention
EMG	Electromyography
FSR	Force Sensing Resister
GC	partial Gravity Compensation
GRF	Ground Reaction Force
HJTO	Human Joint Torque Observer
IMU	Inertial Measurement Unit
LW	Level Walking
MAE	Mean Absolute Error
NDO	Nonlinear Disturbance Observer
RMS	Root-Mean-Square
RPTP	Reference-Point Transformation Period
SA	Stair Ascent
SCI	Spinal Cord Injuries
SD	Stair Descent
SEA	Series Elastic Actuator
SMC	Sliding Mode Control
STS	Sit-to-Stand
TSMC	Robust Terminal Sliding Mode Control

Glossary

VD	Virtual Damping
VM	Vastus Medialis
VS	Virtual Spring
ZI	Zero Impedance

Bibliography

- [1] (2012). [Online]. Available: <http://www.unfpa.org/webdav/site/global/shared/documents/publications/2012/UNFPA-Report-Chapter1.pdf>
- [2] D. Bourbonnais and S. V. Noven, "Weakness in patients with hemiparesis," *American Journal of Occupational Therapy*, vol. 43, no. 5, pp. 313–319, 1989.
- [3] S. Barreca, S. L. Wolf, S. Fasoli, and R. Bohannon, "Treatment interventions for the paretic upper limb of stroke survivors: a critical review," *Neurorehabilitation and Neural Repair*, vol. 17, no. 4, pp. 220–226, 2003.
- [4] W. Huo, S. Mohammed, J. C. Moreno, and Y. Amirat, "Lower limb wearable robots for assistance and rehabilitation: A state of the art," *IEEE Systems Journal*, vol. 10, no. 3, pp. 1068–1081, 2016.
- [5] E. Guizzo and H. Goldstein, "The rise of the body bots," *IEEE Spectrum*, vol. 42, no. 10, p. 42, 2005.
- [6] A. M. Dollar and H. Herr, "Lower extremity exoskeletons and active orthoses: challenges and state-of-the-art," *IEEE Transactions on Robotics*, vol. 24, no. 1, pp. 144–158, 2008.
- [7] M. R. Tucker, J. Olivier, A. Pagel, H. Bleuler, M. Bouri, O. Lambercy, J. del R Millán, R. Riener, H. Vallery, and R. Gassert, "Control strategies for active lower extremity prosthetics and orthotics: a review," *Journal of Neuroengineering and Rehabilitation*, vol. 12, no. 1, pp. 1–29, 2015.
- [8] S. Wang, L. Wang, C. Meijneke, E. Van Asseldonk, T. Hoellinger, G. Cheron, Y. Ivanenko, V. La Scaleia, F. Sylos-Labini, M. Molinari *et al.*, "Design and control of the mindwalker exoskeleton," *IEEE Transactions on Neural Systems and Rehabilitation Engineering*, vol. 23, no. 2, pp. 277–286, 2015.
- [9] R. J. Farris, H. A. Quintero, and M. Goldfarb, "Preliminary evaluation of a powered lower limb orthosis to aid walking in paraplegic individuals," *IEEE Transactions on Neural Systems and Rehabilitation Engineering*, vol. 19, no. 6, pp. 652–659, 2011.
- [10] S. Mohammed, Y. Amirat, and H. Rifai, "Lower-limb movement assistance through wearable robots: state of the art and challenges," *Advanced Robotics*, vol. 26, no. 1-2, pp. 1–22, 2012.

Bibliography

- [11] R. E. Cowan, B. J. Fregly, M. L. Boninger, L. Chan, M. M. Rodgers, and D. J. Reinkensmeyer, "Recent trends in assistive technology for mobility," *Journal of Neuroengineering and Rehabilitation*, vol. 9, no. 1, p. 1, 2012.
- [12] P. Harmo, T. Taipalus, J. Knuuttila, J. Vallet, and A. Halme, "Needs and solutions-home automation and service robots for the elderly and disabled," in *IEEE/RSJ International Conference on Intelligent Robots and Systems*, 2005, pp. 3201–3206.
- [13] H. Herr, "Exoskeletons and orthoses: classification, design challenges and future directions," *Journal of Neuroengineering and Rehabilitation*, vol. 6, no. 1, p. 1, 2009.
- [14] H. Kazerooni and R. Steger, "The berkeley lower extremity exoskeleton," *Journal of Dynamic Systems, Measurement, and Control*, vol. 128, no. 1, pp. 14–25, 2006.
- [15] G. S. Sawicki, K. E. Gordon, and D. P. Ferris, "Powered lower limb orthoses: applications in motor adaptation and rehabilitation," in *9th International Conference on Rehabilitation Robotics*, 2005, pp. 206–211.
- [16] A. B. Zoss, H. Kazerooni, and A. Chu, "Biomechanical design of the berkeley lower extremity exoskeleton (BLEEX)," *IEEE/ASME Transactions on Mechatronics*, vol. 11, no. 2, pp. 128–138, 2006.
- [17] A. Chu, H. Kazerooni, and A. Zoss, "On the biomimetic design of the berkeley lower extremity exoskeleton (BLEEX)," in *IEEE International Conference on Robotics and Automation*, 2005, pp. 4345–4352.
- [18] S. Karlin, "Raiding iron man's closet [geek life]," *IEEE Spectrum*, vol. 8, no. 48, p. 25, 2011.
- [19] G. T. Huang, "Wearable robots," *Technology Review*, vol. 4, 2004.
- [20] K. Yamamoto, K. Hyodo, M. Ishii, and T. Matsuo, "Development of power assisting suit for assisting nurse labor." *JSME International Journal Series C: Mechanical Systems, Machine Elements and Manufacturing*, vol. 45, no. 3, pp. 703–711, 2002.
- [21] K. Yamamoto, M. Ishii, K. Hyodo, T. Yoshimitsu, and T. Matsuo, "Development of power assisting suit (miniaturization of supply system to realize wearable suit)," *JSME International Journal Series C: Mechanical Systems, Machine Elements and Manufacturing*, vol. 46, no. 3, pp. 923–930, 2003.
- [22] M. Vukobratovic, D. Hristic, and Z. Stojiljkovic, "Development of active anthropomorphic exoskeletons," *Medical and Biological Engineering*, vol. 12, no. 1, pp. 66–80, 1974.
- [23] H. Kawamoto and Y. Sankai, "Power assist method based on phase sequence and muscle force condition for hal," *Advanced Robotics*, vol. 19, no. 7, pp. 717–734, 2005.
- [24] (2016). [Online]. Available: <http://rewalk.com/>

- [25] R. J. Farris, H. A. Quintero, and M. Goldfarb, "Performance evaluation of a lower limb exoskeleton for stair ascent and descent with paraplegia," in *Annual International Conference of the IEEE Engineering in Medicine and Biology Society (EMBC)*, 2012, pp. 1908–1911.
- [26] M. Bortole, A. Venkatakrishnan, F. Zhu, J. C. Moreno, G. E. Francisco, J. L. Pons, and J. L. Contreras-Vidal, "The H2 robotic exoskeleton for gait rehabilitation after stroke: early findings from a clinical study," *Journal of Neuroengineering and Rehabilitation*, vol. 12, no. 1, pp. 1–14, 2015.
- [27] K. Suzuki, G. Mito, H. Kawamoto, Y. Hasegawa, and Y. Sankai, "Intention-based walking support for paraplegia patients with robot suit hal," *Advanced Robotics*, vol. 21, no. 12, pp. 1441–1469, 2007.
- [28] Y. Hasegawa, J. Jang, and Y. Sankai, "Cooperative walk control of paraplegia patient and assistive system," in *IEEE/RSJ International Conference on Intelligent Robots and Systems (IROS)*, 2009, pp. 4481–4486.
- [29] T. Sakurai and Y. Sankai, "Development of motion instruction system with interactive robot suit hal," in *IEEE International Conference on Robotics and Biomimetics (ROBIO)*, 2009, pp. 1141–1147.
- [30] H. Kawamoto and Y. Sankai, "Power assist system HAL-3 for gait disorder person," *Computers Helping People With Special Needs*, pp. 19–29, 2002.
- [31] Y. Ohta, H. Yano, R. Suzuki, M. Yoshida, N. Kawashima, and K. Nakazawa, "A two-degree-of-freedom motor-powered gait orthosis for spinal cord injury patients," *Proceedings of the Institution of Mechanical Engineers, Part H: Journal of Engineering in Medicine*, vol. 221, no. 6, pp. 629–639, 2007.
- [32] G. A. Pratt and M. M. Williamson, "Series elastic actuators," in *IEEE/RSJ International Conference on Intelligent Robots and Systems*, 1995, pp. 399–406.
- [33] J. Pratt, B. Krupp, and C. Morse, "Series elastic actuators for high fidelity force control," *Industrial Robot: An International Journal*, vol. 29, no. 3, pp. 234–241, 2002.
- [34] A. Valiente, "Design of a quasi-passive parallel leg exoskeleton to augment load carrying for walking," Master's thesis, Massachusetts institute of Technology, 2005.
- [35] M. B. Wiggin, G. S. Sawicki, and S. H. Collins, "An exoskeleton using controlled energy storage and release to aid ankle propulsion," in *IEEE International Conference on Rehabilitation Robotics*, 2011, pp. 1–5.
- [36] J. A. Blaya and H. Herr, "Adaptive control of a variable-impedance ankle-foot orthosis to assist drop-foot gait," *IEEE Transactions on Neural Systems and Rehabilitation Engineering*, vol. 12, no. 1, pp. 24–31, 2004.

Bibliography

- [37] K. W. Hollander, R. Ilg, T. G. Sugar, and D. Herring, "An efficient robotic tendon for gait assistance," *Journal of Biomechanical Engineering*, vol. 128, no. 5, pp. 788–791, 2006.
- [38] A. W. Boehler, K. W. Hollander, T. G. Sugar, and D. Shin, "Design, implementation and test results of a robust control method for a powered ankle foot orthosis (AFO)," in *IEEE International Conference on Robotics and Automation*, 2008, pp. 2025–2030.
- [39] J. F. Veneman, R. Ekkelenkamp, R. Kruidhof, F. C. van der Helm, and H. van der Kooij, "A series elastic-and bowden-cable-based actuation system for use as torque actuator in exoskeleton-type robots," *International Journal of Robotics Research*, vol. 25, no. 3, pp. 261–281, 2006.
- [40] A. Jafari, N. G. Tsagarakis, B. Vanderborght, and D. G. Caldwell, "A novel actuator with adjustable stiffness (awas)," in *IEEE/RSJ International Conference on Intelligent Robots and Systems (IROS)*, 2010, pp. 4201–4206.
- [41] K. Kong, J. Bae, and M. Tomizuka, "A compact rotary series elastic actuator for human assistive systems," *IEEE/ASME Transactions on Mechatronics*, vol. 17, no. 2, pp. 288–297, 2012.
- [42] G. Carpino, D. Accoto, F. Sergi, N. L. Tagliamonte, and E. Guglielmelli, "A novel compact torsional spring for series elastic actuators for assistive wearable robots," *Journal of Mechanical Design*, vol. 134, no. 12, p. 121002, 2012.
- [43] C.-P. Chou and B. Hannaford, "Static and dynamic characteristics of mckibben pneumatic artificial muscles," in *IEEE International Conference on Robotics and Automation*, 1994, pp. 281–286.
- [44] F. Daerden and D. Lefeber, "Pneumatic artificial muscles: actuators for robotics and automation," *European Journal of Mechanical and Environmental Engineering*, vol. 47, no. 1, pp. 11–21, 2002.
- [45] N. Costa and D. G. Caldwell, "Control of a biomimetic "soft-actuated" 10 dof lower body exoskeleton," in *IEEE/RAS-EMBS International Conference on Biomedical Robotics and Biomechatronics*, 2006, pp. 495–501.
- [46] D. P. Ferris, K. E. Gordon, G. S. Sawicki, and A. Peethambaran, "An improved powered ankle-foot orthosis using proportional myoelectric control," *Gait & posture*, vol. 23, no. 4, pp. 425–428, 2006.
- [47] Y. Saito, K. Kikuchi, H. Negoto, T. Oshima, and T. Haneyoshi, "Development of externally powered lower limb orthosis with bilateral-servo actuator," in *9th International Conference on Rehabilitation Robotics*, 2005, pp. 394–399.
- [48] C. S. Haines, M. D. Lima, N. Li, G. M. Spinks, J. Foroughi, J. D. Madden, S. H. Kim, S. Fang, M. J. de Andrade, F. Göktepe *et al.*, "Artificial muscles from fishing line and sewing thread," *Science*, vol. 343, no. 6173, pp. 868–872, 2014.

- [49] S. Lee, S. Crea, P. Malcolm, I. B. Galiana, A. Asbeck, and C. J. Walsh, "Controlling negative and positive power at the ankle with a soft exosuit," in *IEEE International Conference on Robotics and Automation (ICRA)*, 2016, pp. 3509–3515.
- [50] A. Tsukahara, R. Kawanishi, Y. Hasegawa, and Y. Sankai, "Sit-to-stand and stand-to-sit transfer support for complete paraplegic patients with robot suit hal," *Advanced robotics*, vol. 24, no. 11, pp. 1615–1638, 2010.
- [51] H. Kawamoto, S. Lee, S. Kanbe, and Y. Sankai, "Power assist method for hal-3 using emg-based feedback controller," in *IEEE International Conference on Systems, Man and Cybernetics*, vol. 2, 2003, pp. 1648–1653.
- [52] C. Fleischer and G. Hommel, "A human–exoskeleton interface utilizing electromyography," *IEEE Transactions on Robotics*, vol. 24, no. 4, pp. 872–882, 2008.
- [53] C. Fleischer, A. Wege, K. Kondak, and G. Hommel, "Application of emg signals for controlling exoskeleton robots," *Biomedizinische Technik*, vol. 51, no. 5/6, pp. 314–319, 2006.
- [54] C. Fleischer, C. Reinicke, and G. Hommel, "Predicting the intended motion with emg signals for an exoskeleton orthosis controller," in *IEEE/RSJ International Conference on Intelligent Robots and Systems*, 2005, pp. 2029–2034.
- [55] C. Fleischer and G. Hommel, "Embedded control system for a powered leg exoskeleton," in *Embedded Systems–Modeling, Technology, and Applications*. Springer, 2006, pp. 177–185.
- [56] N. Karavas, A. Ajoudani, N. Tsagarakis, J. Saglia, A. Bicchi, and D. Caldwell, "Tele-impedance based stiffness and motion augmentation for a knee exoskeleton device," in *IEEE International Conference on Robotics and Automation (ICRA)*, 2013, pp. 2194–2200.
- [57] R. Riener, M. Rabuffetti, and C. Frigo, "Stair ascent and descent at different inclinations," *Gait Posture*, vol. 15, no. 1, pp. 32–44, 2002.
- [58] K. Kong and M. Tomizuka, "Control of exoskeletons inspired by fictitious gain in human model," *IEEE/ASME Transactions on Mechatronics*, vol. 14, no. 6, pp. 689–698, 2009.
- [59] M. Grün and U. Konigorski, "Observer based method for joint torque estimation in active orthoses," in *Mathematical Modelling*, vol. 7, no. 1, 2012, pp. 199–204.
- [60] G. Aguirre-Ollinger, J.-E. Colgate, M.-A. Peshkin, and A. Goswami, "Inertia compensation control of a one-degree-of-freedom exoskeleton for lower limb assistance: initial experiments," *IEEE Transactions on Neural Systems and Rehabilitation Engineering*, vol. 20, no. 1, pp. 68–77, 2012.
- [61] H. Kazerooni, J.-L. Racine, L. Huang, and R. Steger, "On the control of the berkeley lower extremity exoskeleton (BLEEX)," in *Proceedings of the IEEE International Conference on Robotics and Automation*, 2005, pp. 4364–4371.

Bibliography

- [62] G. Aguirre-Ollinger, J.-E. Colgate, M.-A. Peshkin, and A. Goswami, "Design of an active one-degree-of-freedom lower-limb exoskeleton with inertia compensation," *International Journal of Robotics Research*, vol. 30, no. 4, pp. 486–499, 2011.
- [63] G. Aguirre-Ollinger, J.-E. Colgate, M.-A. Peshkin, and A. Groswami, "A 1-DOF assistive exoskeleton with virtual negative damping: Effects on the kinematic response of the lower limbs," in *Proceedings of the IEEE International Conference on Intelligent Robots and Systems*, 2007, pp. 1938–1944.
- [64] G. Aguirre-Ollinger, J. E. Colgate, M. A. Peshkin, and A. Goswami, "Active-impedance control of a lower-limb assistive exoskeleton," in *IEEE International Conference on Rehabilitation Robotics*, 2007, pp. 188–195.
- [65] D. Baiden and O. Ivlev, "Human-robot-interaction control for orthoses with pneumatic soft-actuators—concept and initial trails," in *IEEE international conference on Rehabilitation robotics (ICORR)*, 2013, pp. 1–6.
- [66] H. Huang, T. Kuiken, R. D. Lipschutz *et al.*, "A strategy for identifying locomotion modes using surface electromyography," *IEEE Transactions on Biomedical Engineering*, vol. 56, no. 1, pp. 65–73, 2009.
- [67] C. Hintermüller, C. Guger, and G. Edlinger, "Brain-computer interface: generic control interface for social interaction applications," in *International Work-Conference on Artificial Neural Networks*, 2011, pp. 386–392.
- [68] A. J. McDaid, S. Xing, and S. Q. Xie, "Brain controlled robotic exoskeleton for neurorehabilitation," in *IEEE/ASME International Conference on Advanced Intelligent Mechatronics*, 2013, pp. 1039–1044.
- [69] J. L. Contreras-Vidal and R. G. Grossman, "Neurorex: A clinical neural interface roadmap for eeg-based brain machine interfaces to a lower body robotic exoskeleton," in *35th Annual International Conference of the IEEE Engineering in Medicine and Biology Society (EMBC)*, 2013, pp. 1579–1582.
- [70] E. Mikołajewska and D. Mikołajewski, "Neuroprostheses for increasing disabled patients' mobility and control," *Advances in Clinical and Experimental Medicine*, vol. 21, no. 2, pp. 263–272, 2012.
- [71] M. A. Lebedev and M. A. Nicolelis, "Brain-machine interfaces: past, present and future," *Trends in Neurosciences*, vol. 29, no. 9, pp. 536–546, 2006.
- [72] A. H. Do, P. T. Wang, C. E. King, S. N. Chun, and Z. Nenadic, "Brain-computer interface controlled robotic gait orthosis," *Journal of Neuroengineering and Rehabilitation*, vol. 10, no. 1, pp. 1–9, 2013.
- [73] J. L. Pons, "Rehabilitation exoskeletal robotics," *IEEE Engineering in Medicine and Biology Magazine*, vol. 29, no. 3, pp. 57–63, 2010.

-
- [74] D. J. Reinkensmeyer and M. L. Boninger, "Technologies and combination therapies for enhancing movement training for people with a disability," *Journal of Neuroengineering and Rehabilitation*, vol. 9, no. 1, p. 1, 2012.
- [75] S. Musallam, B. Corneil, B. Greger, H. Scherberger, and R. Andersen, "Cognitive control signals for neural prosthetics," *Science*, vol. 305, no. 5681, pp. 258–262, 2004.
- [76] G. Santhanam, S. I. Ryu, M. Y. Byron, A. Afshar, and K. V. Shenoy, "A high-performance brain–computer interface," *Nature*, vol. 442, no. 7099, pp. 195–198, 2006.
- [77] A. J. Casson, D. C. Yates, S. J. Smith, J. S. Duncan, and E. Rodriguez-Villegas, "Wearable electroencephalography," *IEEE Engineering in Medicine and Biology Magazine*, vol. 29, no. 3, pp. 44–56, 2010.
- [78] S. Au, M. Berniker, and H. Herr, "Powered ankle-foot prosthesis to assist level-ground and stair-descent gaits," *Neural Networks*, vol. 21, no. 4, pp. 654–666, 2008.
- [79] K. Suzuki, G. Mito, H. Kawamoto, Y. Hasegawa, and Y. Sankai, "Intention-based walking support for paraplegia patients with robot suit hal," *Journal of Advanced Robotics*, vol. 21, no. 1, pp. 1441–1469, 2007.
- [80] A. Tsukahara, R. Kawanishi, Y. Hasegawa, and Y. Sankai, "Sit-to-stand and stand-to-sit transfer support for complete paraplegic patients with robot suit hal," *Journal of Advanced Robotics*, vol. 24, no. 1, pp. 1615–1638, 2010.
- [81] Y. D. Li and E. T. Hsiao-Weckler, "Gait mode recognition and control for a portable-powered ankle-foot orthosis," in *IEEE International Conference on Rehabilitation Robotics (ICORR)*, 2013, pp. 1–8.
- [82] K. Yuan, S. Sun, Z. Wang, Q. Wang, and L. Wang, "A fuzzy logic based terrain identification approach to prosthesis control using multi-sensor fusion," in *IEEE International Conference on Robotics and Automation (ICRA)*, 2013, pp. 3376–3381.
- [83] F. Zhang, Z. Fang, M. Liu, and H. Huang, "Preliminary design of a terrain recognition system," in *Annual International Conference of the IEEE Engineering in Medicine and Biology Society*, 2011, pp. 5452–5455.
- [84] B. Kleiner and D. Cismeci, "Foresighted control of active foot prostheses," *Proceedings SENSOR*, pp. 669–672, 2011.
- [85] H. Huang, F. Zhang, L. J. Hargrove, Z. Dou, D. R. Rogers, and K. B. Englehart, "Continuous locomotion-mode identification for prosthetic legs based on neuromuscular-mechanical fusion," *IEEE Transactions on Biomedical Engineering*, vol. 58, no. 10, pp. 2867–2875, 2011.
- [86]

Bibliography

- [87] H. A. Quintero, R. J. Farris, and M. Goldfarb, "Control and implementation of a powered lower limb orthosis to aid walking in paraplegic individuals," in *IEEE International Conference on Rehabilitation Robotics*, 2011, pp. 1–6.
- [88] S. A. Murray, K. H. Ha, C. Hartigan, and M. Goldfarb, "An assistive control approach for a lower-limb exoskeleton to facilitate recovery of walking following stroke," *IEEE Transactions on Neural Systems and Rehabilitation Engineering*, vol. 23, no. 3, pp. 441–449, 2015.
- [89] S. Oh, E. Baek, S.-k. Song, S. Mohammed, D. Jeon, and K. Kong, "A generalized control framework of assistive controllers and its application to lower limb exoskeletons," *Robotics and Autonomous Systems*, vol. 73, pp. 68–77, 2015.
- [90] H. Rifai, S. Mohammed, B. Daachi, and Y. Amirat, "Adaptive control of a human-driven knee joint orthosis," in *IEEE International Conference on Robotics and Automation (ICRA)*, 2012, pp. 2486–2491.
- [91] S. Mefoued, S. Mohammed, and Y. Amirat, "Toward movement restoration of knee joint using robust control of powered orthosis," *IEEE Transactions on Control Systems Technology*, vol. 21, no. 6, pp. 2156–2168, 2013.
- [92] W.-H. Chen, "Disturbance observer based control for nonlinear systems," *IEEE/ASME Transactions on Mechatronics*, vol. 9, no. 4, pp. 706–710, 2004.
- [93] J. M. Donelan, R. Kram, and A. D. Kuo, "Mechanical work for step-to-step transitions is a major determinant of the metabolic cost of human walking," *Journal of Experimental Biology*, vol. 205, no. 23, pp. 3717–3727, 2002.
- [94] T. M. Griffin, T. J. Roberts, and R. Kram, "Metabolic cost of generating muscular force in human walking: insights from load-carrying and speed experiments," *Journal of Applied Physiology*, vol. 95, no. 1, pp. 172–183, 2003.
- [95] K. N. Gregorczyk, J. P. Obusek, L. Hasselquist, J. M. S. Bense, K. Carolyn, D. Gutekunst, and P. Frykman, "The effects of a lower body exoskeleton load carriage assistive device on oxygen consumption and kinematics during walking with loads," Tech. Rep., 2006.
- [96] R. Riener, L. Lunenburger, S. Jezernik, M. Anderschitz, G. Colombo, and V. Dietz, "Patient-cooperative strategies for robot-aided treadmill training: first experimental results," *IEEE Transactions on Neural Systems and Rehabilitation Engineering*, vol. 13, no. 3, pp. 380–394, 2005.
- [97] K. N. Gregorczyk, L. Hasselquist, J. M. Schiffman, C. K. Bense, J. P. Obusek, and D. J. Gutekunst, "Effects of a lower-body exoskeleton device on metabolic cost and gait biomechanics during load carriage," *Ergonomics*, vol. 53, no. 10, pp. 1263–1275, 2010.
- [98] G. S. Sawicki and D. P. Ferris, "Powered ankle exoskeletons reveal the metabolic cost of plantar flexor mechanical work during walking with longer steps at constant step frequency," *Journal of Experimental Biology*, vol. 212, no. 1, pp. 21–31, 2009.

-
- [99] S. J. Kang, J. C. Ryu, I. H. Moon, K. H. Kim, and M. S. Mun, "Walker gait analysis of powered gait orthosis for paraplegic," in *World Congress on Medical Physics and Biomedical Engineering*, 2007, pp. 2889–2891.
- [100] B. Husemann, F. Müller, C. Krewer, S. Heller, and E. Koenig, "Effects of locomotion training with assistance of a robot-driven gait orthosis in hemiparetic patients after stroke a randomized controlled pilot study," *Stroke*, vol. 38, no. 2, pp. 349–354, 2007.
- [101] H. Akahira, Y. Yamaguchi, K. Nakazawa, Y. Ohta, and N. Kawashima, "Effect of dynamic knee motion on paralyzed lower limb muscle activity during orthotic gait: A test for the effectiveness of the motor-assisted knee motion device," *Journal of Novel Physiotherapies*, 2012.
- [102] K. Kong and M. Tomizuka, "Control of exoskeletons inspired by fictitious gain in human model," *IEEE/ASME Transactions on Mechatronics*, vol. 14, no. 6, pp. 689–698, 2009.
- [103] K. Kong and D. Jeon, "Design and control of an exoskeleton for the elderly and patients," *IEEE/ASME Transactions on Mechatronics*, vol. 11, no. 4, pp. 428–432, 2006.
- [104] P. Leva., "Adjustments to zatsiorsky-seluyanov's segment inertia parameters," *Journal of Biomechanics*, vol. 29, no. 9, pp. 1223–1230, 1996.
- [105] H. Rifai, S. Mohammed, W. Hassani, and Y. Amirat, "Nested saturation based control of an actuated knee joint orthosis," *Mechatronics*, vol. 23, no. 8, pp. 1141–1149, 2013.
- [106] M. Ferrarin and A. Pedotti, "The relationship between electrical stimulus and joint torque: a dynamic model," *IEEE Transactions on Rehabilitation Engineering*, vol. 8, no. 3, pp. 342–352, 2000.
- [107] P. E. Gill and W. Murray, "Algorithms for the solution of the nonlinear least-squares problem," *SIAM Journal on Numerical Analysis*, vol. 15, no. 5, pp. 977–992, 1978.
- [108] K. X. Xing, J. Huang, and Y. J. Wang, "Tracking control of pneumatic artificial muscle actuators based on sliding mode and nonlinear disturbance observer," *IET Control Theory & Applications*, vol. 4, no. 10, pp. 2058–2070, 2010.
- [109] J. Wu, J. Huang, Y. J. Wnag, and K. X. Xing, "Nonlinear disturbance observer-based dynamic surface control for trajectory tracking of pneumatic muscle system," *IEEE Transactions on Control Systems Technology*, vol. 22, no. 2, pp. 440–455, 2014.
- [110] K.-B. Park. and T. Tsuji, "Terminal sliding mode control of second-order nonlinear uncertain systems," *International Journal of Robust and Nonlinear Control*, vol. 9, no. 11, pp. 769–780, 1999.
- [111] S. Oh, H. Woo, and K. Kong, "Frequency-shaped impedance control for safe human-robot interaction in reference tracking application," *IEEE/ASME Transactions on Mechatronics*, vol. 19, no. 6, pp. 1907–1916, 2014.

Bibliography

- [112] A. Ajoudani, N. G. Tsagarakis, and A. Bicchi, "Tele-impedance: Teleoperation with impedance regulation using a body-machine interface," *The International Journal of Robotics Research*, vol. 31, no. 13, pp. 1642–1656, 2012.
- [113] G. Aguirre-Ollinger, J. E. Colgate, M. A. Peshkin, and A. Goswami, "Design of an active one-degree-of-freedom lower-limb exoskeleton with inertia compensation," *The International Journal of Robotics Research*, vol. 30, no. 4, pp. 486–499, 2011.
- [114] S. Oh, E. Baek, S.-k. Song, S. Mohammed, D. Jeon, and K. Kong, "A generalized control framework of assistive controllers and its application to lower limb exoskeletons," *Robotics and Autonomous Systems*, vol. 73, pp. 68–77, 2015.
- [115] W. Huo, S. Mohammed, Y. Amirat, and K. Kong, "Active impedance control of a lower limb exoskeleton to assist sit-to-stand movement," in *IEEE International Conference on Robotics and Automation*, 2016, pp. 3530–3536.
- [116] G. Aguirre-Ollinger, J. E. Colgate, M. A. Peshkin, and A. Goswami, "Inertia compensation control of a one-degree-of-freedom exoskeleton for lower-limb assistance: initial experiments," *IEEE Transactions on Neural Systems and Rehabilitation Engineering*, vol. 20, no. 1, pp. 68–77, 2012.
- [117] S. P. Buerger and N. Hogan, "Complementary stability and loop shaping for improved human-robot interaction," *IEEE Transactions on Robotics*, vol. 23, no. 2, pp. 232–244, 2007.
- [118] W. S. Newman, "Stability and performance limits of interaction controllers," *Journal of Dynamic Systems, Measurement, and Control*, vol. 114, no. 4, pp. 563–570, 1992.
- [119] P. O. Riley, D. E. Krebs, R. Popat *et al.*, "Biomechanical analysis of failed sit-to-stand," *IEEE Transactions on Rehabilitation Engineering*, vol. 5, no. 4, pp. 353–359, 1997.
- [120] S. Mefoued, S. Mohammed, Y. Amirat, and G. Fried, "Sit-to-stand movement assistance using an actuated knee joint orthosis," in *IEEE RAS & EMBS International Conference on Biomedical Robotics and Biomechatronics (BioRob)*, 2012, pp. 1753–1758.
- [121] A. D. Kuo, "A simple model of bipedal walking predicts the preferred speed-step length relationship," *Journal of Biomechanical Engineering*, vol. 123, no. 3, pp. 264–269, 2001.
- [122] J. J. Craig, *Introduction to robotics: mechanics and control*. Pearson Prentice Hall Upper Saddle River, 2005.
- [123] W. Hassani, S. Mohammed, and Y. Amirat, "Real-time emg driven lower limb actuated orthosis for assistance as needed movement strategy." in *Robotics: Science and Systems (RSS)*, 2013.
- [124] D. A. Winter, *Biomechanics and motor control of human movement*. John Wiley & Sons, 2009.

- [125] H. K. Khalil and J. Grizzle, *Nonlinear systems*. Prentice Hall New Jersey, 1996.
- [126] A. Mohammadi, M. Tavakoli, H. Marquez, and F. Hashemzadeh, “Nonlinear disturbance observer design for robotic manipulators,” *Control Engineering Practice*, vol. 21, no. 3, pp. 253–267, 2013.
- [127] S. Buatois, D. Miljkovic, P. Manckoundia, R. Gueguen, P. Miget, G. Vançon, P. Perrin, and A. Benetos, “Five times sit to stand test is a predictor of recurrent falls in healthy community-living subjects aged 65 and older,” *Journal of the American Geriatrics Society*, vol. 56, no. 8, pp. 1575–1577, 2008.
- [128] M. Sartori, D. G. Lloyd, M. Reggiani, and E. Pagello, “A stiff tendon neuromusculoskeletal model of the knee,” in *IEEE Workshop on Advanced Robotics and its Social Impacts*, 2009, pp. 132–138.
- [129] J. Favre, B. Jolles, R. Aissaoui, and K. Aminian, “Ambulatory measurement of 3D knee joint angle,” *Journal of Biomechanics*, vol. 41, no. 5, pp. 1029–1035, 2008.
- [130] J. Ghan, R. Steger, and H. Kazerooni, “Control and system identification for the berkeley lower extremity exoskeleton (BLEEX),” *Advanced Robotics*, vol. 20, no. 9, pp. 989–1014, 2006.
- [131] V. Zatsiorsky and V. Seluyanov, “The mass and inertia characteristics of the main segments of the human body,” *Biomechanics VIII-B*, vol. 56, no. 2, pp. 1152–1159, 1983.
- [132] H. Woo and K. Kong, “Controller design for mechanical impedance reduction,” *IEEE/ASME Transactions on Mechatronics*, vol. 20, no. 2, pp. 845–854, 2015.
- [133] V. Bonnet, C. Mazza, P. Fraise, and A. Cappozzo, “Real-time estimate of body kinematics during a planar squat task using a single inertial measurement unit,” *IEEE Transactions on Biomedical Engineering*, vol. 60, no. 7, pp. 1920–1926, 2013.
- [134] V. Bonnet, P. Fraise, A. Crosnier, M. Gautier, A. González, and G. Venture, “Optimal exciting dance for identifying inertial parameters of an anthropomorphic structure,” *IEEE Transactions on Robotics*, vol. 32, no. 4, pp. 823–836, 2016.
- [135] I. Skog, P. Handel, J.-O. Nilsson, and J. Rantakokko, “Zero-velocity detection—an algorithm evaluation,” *IEEE Transactions on Biomedical Engineering*, vol. 57, no. 11, pp. 2657–2666, 2010.
- [136] E. Foxlin, “Pedestrian tracking with shoe-mounted inertial sensors,” *IEEE Computer Graphics and Applications*, vol. 25, no. 6, pp. 38–46, 2005.
- [137] G. Wu, S. Siegler, P. Allard *et al.*, “ISB recommendation on definitions of joint coordinate system of various joints for the reporting of human joint motion—part i: ankle, hip, and spine,” *Journal of Biomechanics*, vol. 35, no. 4, pp. 543–548, 2002.

Bibliography

- [138] P.-G. Jung, S. Oh, G. Lim, and K. Kong, "A mobile motion capture system based on inertial sensors and smart shoes," *Journal of Dynamic Systems, Measurement, and Control*, vol. 136, no. 1, p. 011002, 2014.
- [139] J. Bae and M. Tomizuka, "A tele-monitoring system for gait rehabilitation with an inertial measurement unit and a shoe-type ground reaction force sensor," *Mechatronics*, vol. 23, no. 6, pp. 646–651, 2013.
- [140] S. Haykin, *Kalman filtering and neural networks*. New York: Wiley, 2004.
- [141] K. Yuan, Q. Wang, and L. Wang, "Fuzzy-logic-based terrain identification with multisensor fusion for transtibial amputees," *IEEE/ASME Transactions on Mechatronics*, vol. 20, no. 2, pp. 618–630, 2015.
- [142] D. Anderson, R. H. Luke, J. M. Keller, M. Skubic, M. J. Rantz, and M. A. Aud, "Modeling human activity from voxel person using fuzzy logic," *IEEE Transactions on Fuzzy Systems*, vol. 17, no. 1, pp. 39–49, 2009.
- [143] K. Kong and M. Tomizuka, "A gait monitoring system based on air pressure sensors embedded in a shoe," *IEEE/ASME Transactions on Mechatronics*, vol. 14, no. 3, pp. 358–370, 2009.
- [144] L. A. Zadeh, "Outline of a new approach to the analysis of complex systems and decision processes," *IEEE Transactions on Systems, Man and Cybernetics*, no. 1, pp. 28–44, 1973.

List of Figures

1.1	The EICOSI exoskeleton	3
1.2	A subject wearing the EICOSI exoskeleton in the sitting position.	4
1.3	Lower limb exoskeleton E-ROWA	5
1.4	The scope of the thesis	6
2.1	Examples of the existing assistive lower limb exoskeletons with respect to actuation modes	19
2.2	Hierarchical control structure of exoskeletons/orthoses [7]	21
3.1	A subject wearing the 1-DOF active EICOSI in the sitting position.	34
3.2	Nonlinear disturbance observer based SMC/TSMC control diagram for the knee-joint human exoskeleton system.	37
3.3	A mannequin wearing the EICOSI exoskeleton in the sitting position.	41
3.4	Comparison experiments of tracking precision - Joint angles and tracking errors	43
3.5	Comparison experiments of tracking precision - Control torques	44
3.6	Comparison of convergence time - Joint angles and tracking errors	46
3.7	Comparison of robustness with respect to disturbances - Joint angles and tracking errors	47
3.8	The control torques of the basic SMC, NDO-based SMC and NDO-based TSMC.	48
4.1	Schematic view of a subject wearing an exoskeleton and achieving the STS motion in the sagittal plane.	54
4.2	The original impedance of the human exoskeleton system	56

List of Figures

4.3	Whole human-in-loop control structure with the exoskeleton's power assistance	56
4.4	Structure of the nonlinear active impedance control (AIC)	56
4.5	Effectiveness of the active impedance control structure	62
4.6	Human torques with different desired impedance models.	62
4.7	Robustness analysis of the AIC	64
4.8	Evaluation of the robust limitations.	65
4.9	One example of the function of λ_h and λ_k .	68
4.10	Cross-validation results of one subject's identified parameters	74
4.11	EMG sensor placements for the muscles: <i>vastus medialis</i> and <i>biceps femoris</i>	75
4.12	The joint angles, the calculated human joint torque and the processed EMG signals of one subject during the correlation test.	76
4.13	The correlation between the amplitudes of the human joint torque and the RMS of the corresponding EMG signals of one subject	76
4.14	One group of processed EMG signals during flexion/extension movements in four states	79
4.15	The RMS of the processed EMG signals in four states	80
4.16	The reduction ratios of the RMS of the EMG signals during inertia, damping and stiffness compensation compared to the baseline state	82
4.17	The STS transfer task for experimental evaluation with the assistance of the E-ROWA exoskeleton.	84
4.18	The reference trajectory of the whole system.	85
4.19	Human torques with different values of λ	86
4.20	Evaluation of the robust limitations	87
4.21	Evaluation of the effectiveness of the AIC using EMG activities	87
4.22	Effectiveness of the AIC with two different standing up speeds	88
5.1	Lower limb exoskeleton E-ROWA	95
5.2	The main features of different gait modes (level walking (LW), stair ascent (SA) and stair descent (SD)) in one RPTP	98

5.3	Membership functions of the fuzzy logic method	104
5.4	Defined gait phases of three gait modes (level walking (LW), stair ascent (SA) and stair descent (SD)) as well as the associated assistive strategies.	106
5.5	Human model during walking	107
5.6	The fuzzy logic based detection approach of the gait phases.	109
5.7	The whole three-layer control structure	111
5.8	Detection of the zero-velocity instant	112
5.9	Locomotion activities	113
5.10	Extracted features during the locomotion activity (1)	115
5.11	Detection of the gait modes during the locomotion activity (1)	115
5.12	Extracted features during the locomotion activity (2)	116
5.13	Detection of the gait modes during the locomotion activity (2)	116
5.14	Gait phase features of the three gait modes	118
5.15	Generated assistive torques during level walking and stairs ascent/descent . . .	119
5.16	One group of the processed EMG signals during stair descent and ascent in three cases	121
5.17	Comparison of the peak values of the processed EMG signals	121

List of Tables

1.1	The motion angular range of each DoF of the E-ROWA	6
3.1	Subjects' information	42
3.2	Identified system parameters	42
3.3	The mean absolute tracking errors (unit: rad)	49
4.1	Subjects' Information	73
4.2	System's identified parameters	73
4.3	Magnitudes of the model uncertainties	74
4.4	Comparison of the RMS of the EMG signals measured in the four states	81
4.5	Average reduction ratios of the RMS of EMG signals during inertia, damping and stiffness compensation	81
4.6	Identified system's parameters	85
5.1	Fuzzy Rules (Rule-I)	104
5.2	Gait mode and phase based assistive strategy	106
5.3	Fuzzy rules for gait phase detection (Rule-II)	108
5.4	Subjects' Information	113
5.5	Success rate of gait mode detection	117
5.6	Parameters of three assistive control strategies	118

List of Publications

Journals:

- [1] **Weiguang Huo**, Samer Mohammed, and Yacine Amirat, "Impedance Reduction Control of a Knee Joint Human Exoskeleton System", *IEEE Transactions on Robotics*, 2016. (Submitted)
- [2] **Weiguang Huo**, Samer Mohammed, Yacine Amirat, and Kyoungchul Kong, "Fast Gait Mode Detection and Assistive Torque Control of an Exoskeletal Robotic Orthosis for Walking Assistance (EROWA)", *IEEE Transactions on Robotics*, 2016. (Submitted)
- [3] **Weiguang Huo**, Samer Mohammed, Juan C. Moreno, and Yacine Amirat, "Lower Limb Wearable Robots for Assistance and Rehabilitation: A State of the Art", *IEEE Systems Journal*, vol. 10, no. 3, pp. 1068-1081, 2016.
- [4] Samer Mohammed, **Weiguang Huo**, Jian Huang, Hala Rifai, and Yacine Amirat, "Nonlinear Disturbance Observer Based Sliding Mode Control of a Human-driven Knee Joint Orthosis", *Robotics and Autonomous Systems*, vol. 75(A), pp. 41-49, 2016.
- [5] Samer Mohammed, Allou Same, Latifa Oukhellou, Kyoungchul Kong, **Weiguang Huo**, and Yacine Amirat, "Recognition of Gait Cycle Phases Using Wearable Sensors", *Robotics and Autonomous Systems*, vol. 75(A), pp. 50-59, 2016.
- [6] Jian Huang, **Weiguang Huo**, Wenxia Xu, Samer Mohammed, and Yacine Amirat, "Control of Upper-Limb Power-Assist Exoskeleton Using a Human-Robot Interface Based on Motion Intention Recognition", *IEEE Transactions on automation science and engineering*, vol. 12, no. 4, pp. 1257-1270, 2015. ¹

Peer-review Conferences:

- [7] **Weiguang Huo**, Samer Mohammed, Yacine Amirat, and Kyoungchul Kong, "Active Impedance Control of a Lower Limb Exoskeleton to Assist Sit-to-Stand Movement", *IEEE International Conference on Robotics and Automation (ICRA)*, 2016, pp. 3530-3526.

¹Jian Huang and Weiguang Huo contributed equally to this work

List of Tables

- [8] **Weiguang Huo**, Samer Mohammed, and Yacine Amirat, "Walking Assistance through Impedance Control of a Lower-limb Exoskeleton", *International Conference on NeuroRehabilitation (ICNR)*, 2017, pp. 711-715.
- [9] Victor Arnez-Paniagua, **Weiguang Huo**, Ivan Colorado-Cervantes, Samer Mohammed, and Yacine Amirat, "A Hybrid Approach towards Assisting Ankle Joint of Paretic Patients", *20th International Functional Electrical Stimulation Society Annual Conference (IFESS)*, 2016.
- [10] **Weiguang Huo**, Samer Mohammed, and Yacine Amirat, "Observer-based Active Impedance Control of a Knee-Joint Assistive Orthosis", *IEEE International Conference on Rehabilitation Robotics (ICORR)*, 2015, pp. 313-318.

Book Chapters:

- [11] Samer Mohammed, **Weiguang Huo**, Hala Rifai, Walid Hassani, and Yacine Amirat, "Robust Control of an Actuated Orthosis for Lower Limb Movement Restoration", *Intelligent Assistive Robots*, Springer International Publishing, pp. 385-400, 2015.